arXiv:2405.05054v2 [physics.ins-det] 20 Aug 2024

Beam-induced backgrounds measured in the ATLAS detector during local gas injection into the LHC beam vacuum

The ATLAS Collaboration

Inelastic beam-gas collisions at the Large Hadron Collider (LHC), within a few hundred metres of the ATLAS experiment, are known to give the dominant contribution to beam backgrounds. These are monitored by ATLAS with a dedicated Beam Conditions Monitor (BCM) and with the rate of fake jets in the calorimeters. These two methods are complementary since the BCM probes backgrounds just around the beam pipe while fake jets are observed at radii of up to several metres. In order to quantify the correlation between the residual gas density in the LHC beam vacuum and the experimental backgrounds recorded by ATLAS, several dedicated tests were performed during LHC Run 2. Local pressure bumps, with a gas density several orders of magnitude higher than during normal operation, were introduced at different locations. The changes of beam-related backgrounds, seen in ATLAS, are correlated with the local pressure variation. In addition the rates of beam-gas events are estimated from the pressure measurements and pressure bump profiles obtained from calculations. Using these rates, the efficiency of the ATLAS beam background monitors to detect beam-gas events is derived as a function of distance from the interaction point. These efficiencies and characteristic distributions of fake jets from the beam backgrounds are found to be in good agreement with results of beam-gas simulations performed with the FLUKA Monte Carlo programme.

Contents

1 Introduction

The Large Hadron Collider (LHC)[1] is an accelerator of 27 km circumference where proton bunches of a clockwise beam-1 and a counter-clockwise beam-2 are colliding at four interaction regions (IR). During

LHC Run 2, between 2015 and 2018, the proton energy was 6.5 TeV. Interesting physics events have to be extracted from $\sim 10^9$ Hz of minimum-bias collisions overlaid with some beam induced background (BIB). The intensity of BIB is small compared to the minimum-bias background but some BIB events can mimic high transverse momentum (p_T) objects that are characteristic for exotic new physics [2–4].

At the LHC BIB arises from proton collisions with residual gas in the beam pipe (beam-gas interactions) or from beam halo protons[1] impacting on limiting apertures, e.g. collimators [6–8]. The rate of beam-gas events (R_{BG}) depends on the beam intensity and the density and molecular composition of the residual gas in the beam pipe. Beam halo losses have a more complicated dependence on the setting of the various collimators and on the beam quality.

The two principal BIB observables monitored in the ATLAS experiment [9] are hits in the dedicated Beam Conditions Monitor (BCM) [10] and fake jets. Energetic particles emitted at very small angles from the collision of a high-energy proton with a stationary nucleus can initiate particle showers in the accelerator elements. These showers are mostly confined to small radii just around the beam pipe where they can hit the BCM detector modules and produce a trigger signature, indicative of BIB. Fake jets arise predominantly from high-energy muons produced in kaon and pion decays. When traversing the ATLAS calorimeters they have a small probability to deposit a substantial fraction of their energy through radiative processes. If the energy deposit of such an event is large enough it can be reconstructed as a (fake) jet.

Simulations [11], which agree well with measurements of total BIB rates, indicate that most of the background seen by the BCM originates from beam-gas collisions at less than 60 m from the interaction point (IP). Fake jets, on the other hand, are due to beam losses far upstream – beyond ~50 m from the IP. So far there has been no direct experimental verification of these simulation predictions, which was the main motivation for the study described in this paper.

BIB monitoring and detailed analysis of BIB events collected by the ATLAS detector during LHC Run 1 [12, 13] and Run 2, in particular during dedicated loss-map tests [5], have shown that beam-halo losses are a minor contribution [14] and most of the BIB observed by ATLAS originates from inelastic beam-gas collisions.

In order to quantify the sensitivity of ATLAS to beam-gas events at various well-defined locations, a series of dedicated pressure bump tests was performed during LHC Run 2. In these tests individual non-evaporable getter (NEG) cartridges [15] were heated such that some of the gas they had absorbed was re-injected into the LHC beam vacuum. By this method pressure bumps, with a typical extent of ~1 m FWHM along the beam direction, were created at four different $|z|$-locations[2] between 19 m and 151 m. In these bumps the pressure was up to four orders of magnitude higher than during normal beam operation. Given that the BIB observed in ATLAS, during physics data taking, is dominated by beam-gas collisions distributed over a typical length of the order of 100 m, these local pressure bumps resulted in a detectable increase of the BIB. Since the efficiency of ATLAS to record a beam-gas event depends on the location of that event, the additional BIB rates from some pressure bumps exceeded the normal level by orders of magnitude, while for some others an excess was barely resolvable.

These pressure bump tests provide detailed data for benchmarking the BIB simulations, and the results also are useful input for designing LHC beam vacuum upgrades such that the beam-gas background in the experiments is minimised.

---

[1] Beam halo is composed by a small fraction of particles surrounding the dense beam core [5].

[2] In the right-handed ATLAS coordinate system the origin is at the nominal IP and the azimuthal angle, ϕ, is measured relative to the x-axis, which points towards the centre of the LHC ring. The polar angle, θ, is defined with respect to the z-axis, which points along the beam-2 direction. The pseudorapidity is given by $\eta = -\ln\tan(\theta/2)$.
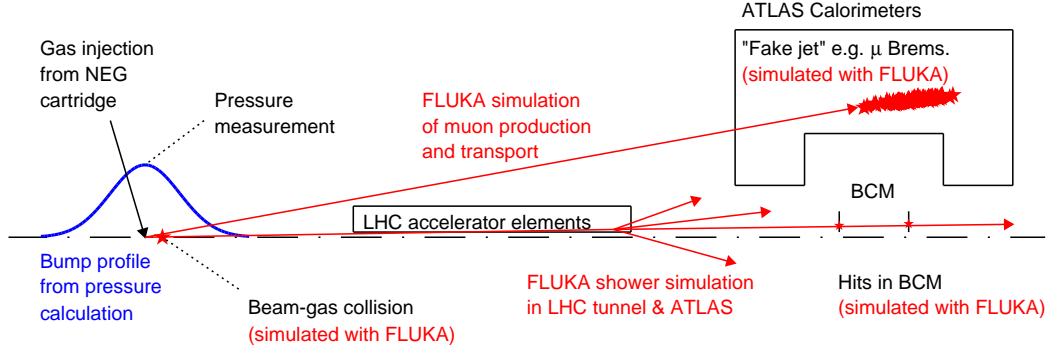
Figure 1: Schematic illustration of the pressure bump test. The red arrows and stars indicate particle collisions and trajectories. The blue text and profile indicate the estimates of the pressure bump profiles, which are discussed in Section 3.5. The red text refers to quantities and processes simulated with FLUKA, as described in Section 4. Black text is used for detector and accelerator components, real events, actions and measured observables.

1.1 Short overview of the test procedure

Figure 1 shows a schematic summary of the measurement, analysis and simulation procedures. The creation of the pressure bump and the associated pressure measurement are described in Sections 3.3 and 3.4, respectively.

Two definitions of the relation between the BIB seen by ATLAS and the pressure increase at the bump location can be considered.

1. The ratio, $\omega(z_i)$, between the additional background rate ΔB, observed by a given ATLAS detector, and the additional pressure, $\Delta P(z_i)$, measured by a vacuum gauge at the bump location z_i, i.e.

$$\omega(z_i) = \frac{\Delta B}{\Delta P(z_i)}. \tag{1}$$

2. The ratio, $\varepsilon(z)$, between the additional background rate observed by a given ATLAS detector and the rate of additional beam gas events, ΔR_{BG}, due to the introduced pressure bump. Here ΔR_{BG} is the change of the integral over the gas density in the bump area, i.e.

$$\varepsilon(z) = \frac{\Delta B}{\Delta R_{BG}} = \frac{\Delta B}{f \frac{\Delta P(z_i)}{P_{calc}(z_i)} \int \rho_{calc}(z) dz}, \tag{2}$$

where $\rho_{calc}(z)$ denotes the pressure profile that is obtained from calculations described in Section 3.5 and $P_{calc}(z_i)$ is the corresponding calculated pressure at the vacuum gauge location. The ratio of the measured $\Delta P(z_i)$ and the calculated value is used to renormalise the profile such that it matches the measured pressure at the gauge location. The factor f is related to the interaction cross section of the protons and the beam intensity, as described in Section 3.3.

The determination of $\omega(z_i)$ is described in Section 5. Since $\omega(z_i)$ is entirely based on measured data, it is not subject to any of the assumptions and calculations that have to be made in order to derive $\varepsilon(z)$. Thus it is a useful quantity to verify the consistency of the results for the same bump location in different LHC fills.

Also the $|z|$-dependence of the ratio of BCM and fake-jet BIB rates can be assessed from the measured data by using the respective $\omega(z_i)$-values. The downside of the $\omega(z_i)$-parameter is that it does not accurately describe the sensitivity of ATLAS to beam-gas background because a single pressure measurement does not provide enough information to determine the number of beam-gas collisions. Furthermore, the relation between $P(z_i)$ and the integrated density profile along the beam trajectory, $\int \rho(z)dz$, depends on the local vacuum equipment configuration, e.g. the distance between the point of gas injection and the vacuum gauge. Since these configurations are different at all bump locations, $\omega(z_i)$ provides only an approximate measure of the relative sensitivity between the four pressure bump locations.

The $\varepsilon(z)$ represents the real efficiency, i.e. the ratio between observed and produced events, which does not depend on the local vacuum equipment configuration or the beam conditions. Its determination needs, however, information about the gas density, $\rho(z)$, traversed by the beam in order to determine the rate of beam-gas interactions. Because the density profile cannot be measured by the LHC instrumentation, $\varepsilon(z)$ cannot be derived from data alone and is subject to the uncertainties of the dedicated pressure calculations, described in Section 3.5.

The $\omega(z_i)$ and $\varepsilon(z)$ are derived in Sections 5 and 6, respectively and their uncertainties are discussed in Section 7. BIB simulations with the FLUKA code [16, 17] are described in Section 4. These simulations compute the efficiency per event and can therefore be directly compared with $\varepsilon(z)$, which is done in Section 8.1. The azimuthal and pseudorapidity distributions of the simulated fake jets are compared with the measurements for different pressure bump locations in Section 8.2.

Section 9 gives a brief report of an unexpected increase of BIB levels after the last pressure bump test and Section 10 provides the conclusions.

2 Beam background measurements in ATLAS

2.1 The ATLAS experiment

ATLAS [9] is one of the two general purpose experiments, designed to fully exploit the proton–proton physics at the highest luminosities achievable at the LHC.

The inner detector (ID) provides the tracking and momentum measurement of charged particles up to $|\eta| = 2.5$. From the smallest to the largest radii it comprises a pixel detector, a silicon micro-strip tracker and a transition radiation detector. All of these are subdivided into barrel and endcap parts, embedded in a solenoid, which creates a magnetic field of 2 T along the z-axis.

The BCM is housed inside the ID and consists of four small diamond sensors on both sides of the IP at $|z| = 184$ cm. Following the ATLAS convention of labelling the sides of the experiment as A and C, the BCM-A and the BCM-C modules are on the incoming beam-1 and beam-2 sides, respectively. The sensors, with an active area of 8×8 mm^2, are arranged as a cross at an average radius of 55 mm from the centre of the beam line. In order to increase the track length within the sensitive volume, and thereby the signal of a BIB-particle, the modules are tilted by 45 degrees with respect to the z-axis [10].

The ID is surrounded by an electromagnetic calorimeter using lead as the absorber and liquid argon (LAr) as the active medium. The barrel part has a half-length of ~3 m and extends radially from $r = 1.5$ m to 2.0 m. At central rapidities the hadron energy is measured by a steel/scintillator tile calorimeter, extending from $r = 2.3$ to 4.3 m and having a half-length of ~6 m. In the endcaps both calorimeters are based

on LAr technology and provide coverage up to $|\eta| = 3.2$. These calorimeters are complemented by a forward calorimeter (FCAL), which reaches up to $|\eta| = 4.9$. All calorimeters provide nanosecond timing resolution.

The calorimeters are surrounded by a muon spectrometer based on three large air-core superconducting toroidal magnets with eight coils each: one barrel toroid and two endcap toroids positioned inside the barrel at both ends of the central solenoid.

The very forward region, behind the FCAL, is filled with massive shielding in order to reduce the radiation levels in the muon spectrometer. This shielding also serves as a plug of the tunnel entry such that the BIB – except the high-energy muon component – entering the ATLAS cavern is efficiently suppressed.

Potentially interesting events are selected with a two-stage trigger[18], where the first stage (Level-1) is hardware-based and fires on simple physics objects. The Level-1 selection is followed by a software high-level trigger, which further reduces the rate before the selected events are stored for offline analysis. An extensive software suite[19] is used in the reconstruction of data, in detector operations and in the trigger and data acquisition systems of the experiment.

2.2 ATLAS beam background triggers

The measurement of BIB utilises bunches that do not collide with bunches of the opposite beam at the ATLAS IP. In the Level-1 trigger these unpaired bunches form their own bunch group. This grouping isolates the background trigger items from those used for physics and allows trigger prescales to be applied independently. This is particularly important for the low-p_T single-jet trigger, which is used for fake-jet monitoring. In colliding bunches low-p_T jets appear at overwhelming rates and the only possibility to collect a sizeable sample of fake-jet events is to trigger independently on the unpaired bunches without the need reduce the rate by a prescale.

ATLAS data-taking is subdivided into luminosity blocks (LBs) with a typical duration of ~60 s. This time is short enough to consider variations of beam conditions to be negligible.[3] Although individual events have a time-stamp with nanosecond accuracy the LBs provide convenient time-bins for trend monitoring. This also ensures that Level-1 trigger rates (which are always averaged over a LB), offline data and information received from the LHC can be analysed within a common time binning.

The signature of BIB in the BCM, shown schematically in Figure 2, is formed by one early hit in any of the four sensors on one side and an in-time hit in any sensor on the other side of the IP. An early hit is defined to be in a 5.46 ns wide time-window, centred ~6 ns before the nominal collision time. An in-time hit has the same window width, but centred ~6 ns after the nominal collision time, i.e. aligned in time with the collision products from the IP. Due to its location the BCM is particularly sensitive to BIB showers developing at small radii, just outside the beam pipe.

Fake jets are almost exclusively due to radiative energy losses of high-energy muons traversing the detector, in particular bremsstrahlung, resulting in electromagnetic showers with a relatively small extent and negligible hadronic activity. They are selected in the range $|\eta| < 3.2$ by a single jet trigger[20], which fires on a transverse energy deposition above $E_T > 12$ GeV, calibrated at the electromagnetic scale. Since, however, the fake jet is not associated to any object with p_T defined at the IP, the E_T should be considered an

---

[3] This assumption is not true for fast losses due to sudden beam instabilities, but these are not a subject of the present study.
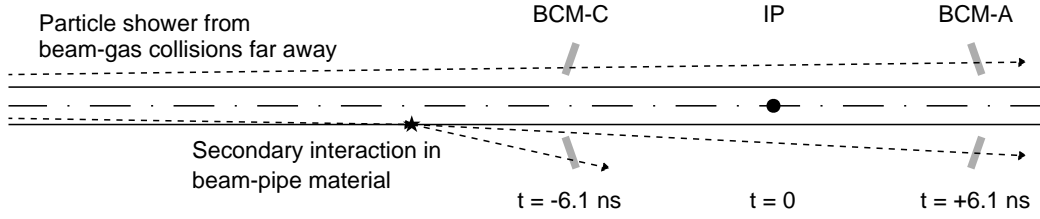
Figure 2: Illustration of the BCM background trigger signature for beam-2. The vertical dimensions are not to scale. In particular, the size of the BCM sensors is exaggerated and their tilt is indicated only schematically. The dot-dashed line is the beam line and the two solid lines illustrate the wall of the beam pipe. The dashed lines represent the trajectories of particles produced in proton collisions with residual gas or accelerator elements. The trigger can be fired either by a single particle traversing a module on both sides of the IP or by two different particles as illustrated on the upper and lower parts of the figure, respectively. The only requirement is that there are early and in-time hits in any of the four modules on opposite sides of the IP.

apparent E_T, which is assigned by the reconstruction algorithm on the basis of the position and magnitude of the energy deposition in the calorimeter.

The jet trigger is fully efficient up to $|\eta| = 2.8$ and has reduced sensitivity up to $|\eta| = 3.2$. At various stages of the trigger chain the recorded events are subject to dead time, which is evaluated for each LB. A dead-time correction is applied by scaling the recorded event rate correspondingly. The trigger efficiency starts to rise gradually above the E_T-threshold of 12 GeV, and full efficiency is reached only around 20 GeV. For most of the results in this paper the trigger efficiency can be considered an intrinsic property of the jet-observable that is used to detect a BIB event by the fake-jet monitoring. Thus, whatever the efficiency to detect the fake jet is, it is the same in the pressure bump test and during normal physics operation. In order to maximise the number of fake-jet events for the analysis, all jets that have a reconstructed transverse energy of 12 GeV and for which the corresponding Level-1 jet trigger has fired are retained. However, the reduced efficiency below 20 GeV becomes significant when comparing measured and simulated fake-jet rates. For these comparisons only jets at the efficiency plateau, i.e. with $E_T > 20$ GeV, are considered.

2.3 Fake-jet reconstruction and cleaning

Even in unpaired bunches the jet sample has a non-negligible contribution from collisions of protons in the unpaired bunch with ghost charge in the other beam, i.e. recaptured protons that have left their original radio-frequency bucket [13]. These ghost collisions take place at the IP but the luminosity of these encounters is typically ~3 orders of magnitude below that of two colliding nominal bunches. This contribution can be removed with high efficiency by applying a vertex veto, i.e. requiring that the event where the jet is observed has no reconstructed primary vertex [21].

The jets are reconstructed with the anti-k_t jet algorithm [22, 23] from clusters at the electromagnetic scale [24], using a radius parameter $R = 0.4$. No further calibrations are applied since these would not be appropriate for the fake jets that do not originate from the IP, are not subject to event pile-up, and have a negligible hadronic contribution. Standard jet quality criteria [25], are applied in order to remove instrumental backgrounds, e.g. effects of calorimeter noise.
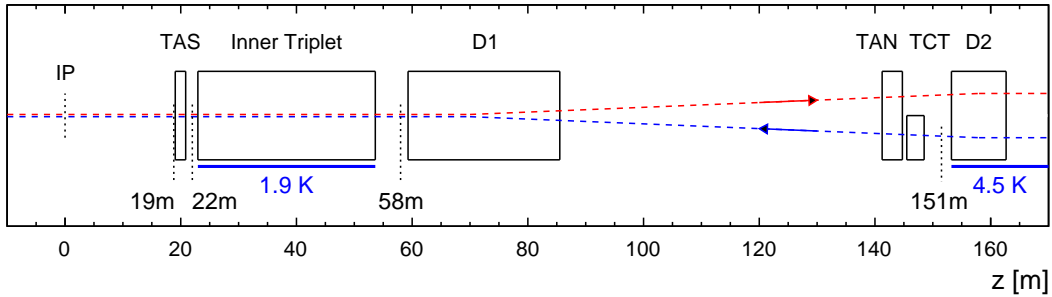
Figure 3: Schematic illustration of the LSS up to the D2 dipole, i.e. the part relevant for this study. The pressure bump locations at 19 m, 22 m, 58 m and 151 m are indicated, as well as the temperatures of the cryogenic elements in the area. The vertical dimensions are not to scale.

In the barrel calorimeters, the axis of a BIB-induced shower is parallel to the beam direction, instead of pointing to the IP. Previous studies [11] have shown that FLUKA simulations, implementing only a rudimentary clustering of the total deposited energy, reproduce the fake jet rates reconstructed from the data. This indicates that, even though the energy deposition is elongated in the wrong direction with respect to the IP, the cluster in the data is not split by the reconstruction.

2.4 BCM efficiency and purity

The threshold for the BCM to record a hit corresponds to an energy deposition of around 250 keV, above which the efficiency is assumed to be close to 100%. After a hit, however, an individual module has a dead time with a typical duration of the order of 10 ns, depending on the deposited energy. Thus a hit before the trigger window can mask another that would have contributed to the trigger signature. This potential efficiency drop has to be taken into account when comparing data with simulations.

Since the BCM background trigger involves an early hit, its sensitivity to ghost collisions is strongly suppressed. Less than 4% of the triggered events would be rejected by a vertex veto. Thus the number of events collected was maximised and issues of dead-time corrections were mitigated by basing the analysis on the raw Level-1 trigger rates, recorded from the unpaired bunches.

3 The pressure bump tests

3.1 The IR1 region around ATLAS

Earlier BIB simulation studies, e.g. those presented in Refs. [6, 8, 11], predict that BIB can be observed from beam-gas interactions in the entire long straight section (LSS) and part of the LHC arc, up to a distance of about 500 m from the IP.

The main accelerator components in the part of the LSS that is relevant for the pressure bump tests are illustrated in Figure 3. Between the IP and $z = 18.5$ m, the radius of the beam pipe varies between 28 mm and 120 mm. The cryogenic inner triplet of quadrupole magnets extends from $|z| = 23$ m up to $|z| = 55$ m and inside of it a perforated beam screen (BS), kept at a temperature of ~20 K, reduces the synchrotron radiation load on the beam-pipe wall. Residual gas in this cryogenic section can pass through

8

the perforations and condense on the cold bore, kept at 1.9 K. The triplet is protected by the secondaries absorber (TAS) from the collision debris created at the IP. The TAS devices, one on either side of the experiment, starting at $|z| = 19$ m, are 1.8 m long copper blocks with an aperture of 17 mm radius for the passing beams. Vacuum stations with ion pumps and NEG cartridges, placed on either side of the TAS, provide efficient local pumping.

From $|z| = 55$ m to $|z| = 152.5$ m the beam pipe is at room temperature. One of the few warm magnets of the LHC, the D1 separation dipole, is located in this region. Extending from 59 m to 83 m, its role is to separate the beams from the common pipe at the IP into the two separate pipes in the LHC arc. Other beam-line elements that are potentially significant for this study are the set of tertiary collimators (TCT) and the neutral absorber (TAN). The TCTs are located in the region $|z| = 145$ m-148 m, and with apertures of 18.4 mm in the horizontal and 11.6 mm in the vertical plane[4] they are likely to intercept some of the secondaries produced in the most distant pressure bump at 151 m. The role of the TAN is to intercept neutral particles produced at the IP and that are not deflected by the D1 dipole, before they would impinge on the D2 dipole, which is operated at 4.5 K.

The room-temperature sections of the LHC beam pipe are coated with a TiZrV NEG layer [26], which provides distributed pumping. Especially in the region |z|<18 m this NEG coating and a pair of low-capacity annular ion pumps, located at $z \approx \pm 3.7$ m, ensure a good vacuum around the IP.

In the cold arc of the LHC, starting at $|z| \approx 270$ m, a good vacuum is ensured by the cryogenic surfaces of the magnets, which constitute very efficient pumps. No gauges or other active vacuum equipment exists in the cold regions, so the pressure bump study is limited to four points in the LSS, $|z| = 19$ m, 22 m, 58 m and 151 m, which are indicated in Figure 3.

3.2 Beam conditions

During Run 2 of the LHC the colliding protons were grouped in bunches with a typical population of $n_b = 10^{11}$. A bunch train was composed of a varying number of bunches, spaced by 25 ns. Larger gaps, of up to 800 ns, were left between the trains to account for the rise-times of injection kickers. One wide gap of 3.1 μs is needed in the bunch pattern in order to allow for a clean beam abort.

Typically twelve unpaired bunches per beam are included in an LHC fill pattern. These are usually grouped in short trains immediately after the abort gap in order to maximise their separation from the preceding colliding pairs. In this position the afterglow, i.e. long-lived debris from the collisions [13], is minimised.

Five pressure bump tests were performed in LHC fills 4905, 5005, 5331 (all in 2016), 6239 (in 2017) and 7212 (in 2018). The principal beam parameters of these five fills are summarised in Table 1. In order to reduce the risk of a beam dump due to the increased local loss rate, all tests were done during the intensity ramp-up following regular technical stops of the accelerator. Thus all five fills were characterised by a smaller than nominal number of bunches and, therefore, lower total beam intensity than regular physics fills.

The beams had typical per-bunch luminosities of $\sim 5 \times 10^{30}$ cm^{-2}s^{-1} for physics production, except for fills 5331 and 7212, during which the beams were separated about half way through the fill in order to provide low collision rates for dedicated forward physics data-taking. The beam-gas backgrounds are insensitive to this beam separation.

---

[4] Corresponding to 2016 collimator settings.

Table 1: Beam conditions of the five fills during which pressure bump tests were performed. β^* is the value of the β-function at the IP and is related to the transverse size of the luminous region [27]. The β^* and crossing angle values refer to the ATLAS IP.

	LHC fill				
	4905	5005	5331	6239	7212
Number of bunches per beam	241	602	169	1358	603
Number of unpaired bunches	12	12	12	12	13
Maximum bunch train length	72	72	48	8	48
β^* [cm]	40	40	40	30	30
Crossing half-angle [μrad]	185	185	140	150	155
Single beam intensity [10^{13} protons]	3.2	7.1	1.8	12	6

3.3 LHC beam vacuum description and gas injection procedure

The ultra-high vacuum conditions inside the LHC beam pipe are achieved by distributed pumping, provided by the NEG coating in the room-temperature sections and cryopumping in the cold sections.

A central parameter for this study is the sticking factor (α) of hydrogen molecules on the NEG coated surface in the room-temperature sections. This factor represents the probability for a gas molecule, hitting the surface, to stick on it. Thus it corresponds to the pumping efficiency of the NEG coating. It is shown in Section 3.5 that the amount of gas in the introduced pressure bump depends strongly on this parameter. In validation tests [28], prior to installation, α was measured to be larger than 10^{-3} with $\alpha = 5 \times 10^{-3}$ being a commonly expected value for the installed beam pipe.

Table 2 lists the inelastic proton cross sections for the typical molecules found in the beam vacuum. The gases relevant for this study are hydrogen and neon. Although the latter is not a common gas in ultra-high vacuum systems it could have influenced these tests significantly, as is discussed in Section 6.4.

In cryogenic parts of the LHC no NEG coating is needed since the cold bore of a magnet operated at 1.9 K represents a 100% efficient pump for all gas species except helium [29]. Since, however, the perforations cover only about 3% of the BS surface, the pumping efficiency, or sticking factor, of the cryogenic sections is estimated at 3×10^{-2}. Some magnets in the LSS, in particular the D2 dipole, are kept at an elevated temperature of 4.5 K at which the sticking factor, especially for hydrogen, is significantly reduced. In order to ensure a good vacuum in these warmer magnets, dedicated cryoabsorber strips of woven carbon fibre are incorporated into the BS.

In the presence of an intense proton beam, gas is desorbed from the beam-pipe and BS walls by synchrotron radiation, particles hitting the surface and radio-frequency heating induced by the passing bunches. The rate of gas release depends on the surface condition and is reduced by the NEG coating and beam scrubbing in the warm and cryogenic sections, respectively. The latter procedure consists of keeping increasingly intense low-energy beams in the LHC in order to release the gas molecules from the surface prior to actual physics operation. The degree of conditioning cannot be directly measured and the actual state of the surface introduces a significant uncertainty into the pressure around the ring, especially in cold sectors where no vacuum gauges are located. Since, however, the pressure bumps are introduced by controlled gas injection and the steady-state background is subtracted, as is explained in Section 5, the uncertainty of the overall pressure distribution is only of minor importance for this study.

Table 2: Densities (ρ) at STP (0° C and 1.013 bar) and inelastic scattering lengths (λ) of LHC beam protons for the common residual gas molecules. The densities and scattering lengths are extracted from the FLUKA code. The cross sections derived from λ and ρ are given for reference only. The uncertainty on the density is negligible and that on the scattering length a few percent (Section 7.1.1). The last column gives the relative response of the vacuum gauge for each gas species with respect to N_2 [30]. The uncertainties on these sensitivities are estimated at about 10%, but are included in the gauge accuracies, which are discussed in Section 7.1.1.

Gas	Density (ρ) [g/m^3] at STP	Inelastic scattering length (λ) [m] at STP at 6.5 TeV	Inelastic cross section [mb] at 6.5 TeV	Gauge response [N_2 equivalent]
H_2	89.9	4900	76	0.42
Ne	900	980	380	0.22
CH_4	716	890	420	1.4
CO	1250	630	590	1.05
CO_2	1970	410	920	1.4

The typical densities of the residual gases are about 12 orders of magnitude below those at standard temperature and pressure (STP), which means that the mean free path of a beam proton is of the order of 10^{12} km. This implies that the average lifetime of an individual 6.5 TeV proton, before it undergoes a beam-gas interaction, is about 1000 h.

If the gas densities are known, R_{BG} can be derived by using the data of Table 2. The mean free path $\lambda(z)$ is given by

$$\frac{1}{\lambda(z)} = \sum_j \frac{N_A \rho_j(z) \sigma_j}{A_j},$$

(3)

where N_A is the Avogadro number and σ_j and A_j are the interaction cross section and atomic mass of residual gas species j, respectively. When the proton beam traverses the gas, it sees a z-dependent density $\rho_j(z)$. In the ultra-high vacuum λ is very large and the total interaction probability for a single proton traversing a gas density distribution between z_1 and z_2 is obtained from a linear approximation

$$P_{BG} = \int_{z_1}^{z_2} \frac{dz}{\lambda(z)} = \sum_j \frac{N_A \sigma_j}{A_j} \int_{z_1}^{z_2} \rho_j(z) dz.$$

(4)

When P_{BG} is multiplied by the number of protons per bunch (n_b) – by convention expressed in units of 10^{11} protons – and the revolution frequency ν of the LHC beam, R_{BG} is obtained in units of Hz/$10^{11}\, p$ for the z-range considered. Thus the factor f in Eq. (2), for a single gas, is given by

$$f = n_b \nu \frac{N_A \sigma}{A},$$

(5)

i.e. it comprises only constants and measured quantities.

The R_{BG} arising from the pressure distribution during normal operation was studied thoroughly with simulations for LHC Run 1 [11] and good agreement between simulated and measured BIB rates was obtained. Although the bunch spacing was reduced from 50 ns to 25 ns and the beam energy was increased for Run 2, the BIB levels recorded by the BCM in the pressure bump fills, prior to the gas injection, were very similar to those seen in Run 1. This suggests that the R_{BG} distribution as a function of z, presented in Ref. [11], provides a good estimate for the pedestal R_{BG} in the pressure-bump fills. According to that

study the R_{BG} is about 0.01 Hz/(10^{11} $p \cdot$ m) for $|z| \lesssim 20$ m and varies between 0.05 Hz/(10^{11} $p \cdot$ m) and 0.5 Hz/(10^{11} $p \cdot$ m) for larger $|z|$. These R_{BG} values were used to define the target pressure for the bump tests, i.e. to determine how much additional gas was needed in order to induce about an order of magnitude increase in the BIB rate seen by the BCM. For the most distant bump location, at 151 m, only a factor of about five increase of the BIB rate was reached at a pressure of ~1 nbar, which was considered the safe limit.

Local vacuum stations, typically comprising ion pumps, NEG cartridges and vacuum gauges, are installed in the warm sections. The NEG cartridges, Capacitorr D-400 of SAES getters [31], are composed of sintered discs of non-evaporable getter material, contained in a protective stainless steel grid. They are equipped with a heater element for activation. In these tests the heaters were used to provoke an emission of gas from the cartridges at the locations indicated in Figure 3. The rate of gas release was controlled by the current used to heat the NEG and the pressure was monitored with the nearby gauges. Upon heating the NEG is assumed to release predominantly hydrogen, which is least strongly bound into the NEG material. Thus the gas composition of an introduced pressure bump differs significantly from the average in that region during normal operation. Given that the pressure in the bumps was up to four orders of magnitude above normal, the additional beam-gas interactions were initially assumed to all be p-H collisions, although this assumption had to be revised in the course of the analysis.

Since only BIB events from unpaired bunches were used, the observed background could be unambiguously associated with one of the two incoming beams. Therefore it was possible to heat two NEG cartridges simultaneously, one on either side of ATLAS. It took typically 5–10 minutes to reach the target level, where the pressure was stabilised for about 20 minutes in order to collect a sufficient number of events. Between consecutive pressure bumps on the same beam about 20 minutes were left for the BIB to fall close enough to the initial level.

3.4 Pressure measurement

The warm sections of the LHC beam pipe are equipped with vacuum gauges in order to monitor the pressure constantly. In the regions where the pressure bumps are introduced, two different gauge technologies are utilised:

VGPB: cold cathode gauges [30], Pfeiffer vacuum IKR 070, triaxial and

VGI: hot cathode gauges [32], custom CERN made.

The measurement ranges of both gauge types cover the full pressure variation during the bump tests.

During the tests two or three gauges provided data in the vicinity of each pump but the positioning of the gauges with respect to the beam line and the NEG cartridge is different at each pressure bump location. Some gauges exhibited erratic behaviour in one or more fills. Therefore only the data from the most appropriate devices, in terms of vicinity to the activated NEG cartridge and consistency of the data in all fills, were used. In most cases, selecting an alternative gauge would have had only a very small influence on the results. This is discussed as a systematic uncertainty in Section 7.1.1.

3.5 Estimation of pressure bump profiles

Because a vacuum gauge does not provide any information about the gas density profile along the beam line, pressure calculations have to be invoked to estimate the profiles, $\rho(z)$, which are needed to calculate R_{BG} from Eq. (4).

For the calculation of pressure profiles at the various bump locations, two conceptually different vacuum calculation/simulation programs were used:

1. VASCO [33] uses a simple one-dimensional model to produce a pressure profile along the beam line, based on the requirement that various sources (outgassing mechanisms), drains (local or distributed pumps) and the diffusion of gas between sources and drains, are in equilibrium.

2. MOLFLOW+ [34] is a detailed three-dimensional Monte Carlo simulation which transports individual gas molecules until they are removed by a pump or absorbed on a surface. In order to benefit fully from the power of MOLFLOW+, a detailed three-dimensional description of the vacuum system is needed.

Initially, only VASCO calculations, based on the best knowledge of the pumping efficiency in the room temperature and cryogenic parts of the beam pipe, were produced for all four pressure bump locations. These, however, resulted in unphysically low values of R_{BG} for the nearby pressure bumps at $|z| < 23$ m, as is seen in Section 6.3. Therefore more detailed MOLFLOW+ simulations were set up for the 19 m and 22 m pressure bumps, exploring various alternative pumping efficiencies of the NEG coating. No sufficiently detailed MOLFLOW+ geometry models are available for the 58 m and 151 m locations, so the original VASCO results are used for these distant pressure bumps. The uncertainties associated with these calculations are discussed in Section 7.1.

The NEG cartridges and vacuum gauges are not directly on the beam pipe, but recessed on the same or different chimneys. When gas is emitted from the NEG cartridge, the pressure at the gauge is typically different than at the chimney exit. Being one-dimensional, the VASCO calculations do not consider the various chimneys in detail, so they do not provide estimates for the pressures at the gauge locations. The MOLFLOW+ simulations, on the other hand, can provide an estimate of the gas density profiles along the beam line where the protons pass, but also at the location of the gauge where the pressure is measured.

Figure 4 shows the MOLFLOW+ results for pressure bumps at 19 m and 22 m, for different values of the NEG sticking factor α. The value of α is found to have a particularly large effect on the pressure profile of the 19 m bump. The reason is that between 19 m and 20.8 m the TAS, with its small aperture, reduces the gas flow while the beam pipe towards the IP is wide, and for low α the pressure bump extends almost to the IP. It is also seen that with increasing α the difference between the value at the gauge and the maximum at the beam line increases.

The situation is quite different at 22 m where the pressure bump is constrained between the TAS on the IP side and the $T = 1.9$ K region of the inner triplet, starting at $|z| \approx 23.5$ m. The cold bore of the quadrupole magnet is considered a 100% efficient pump for all gas species. So any gas molecule traversing the pumping holes, which cover about 3% of the BS, is considered to be absorbed. Since this cold part has no NEG coating, the effect of α is restricted to the region between the inner triplet and the TAS and, for the small amount of gas passing through it, the beam pipe on the IP side of the TAS. This restriction from both sides is very evident when comparing Figures 4(b) and 4(a): for $\alpha = 0.005$ the pressure drops by two orders of magnitude when the gas is injected at 22 m and has to traverse the TAS. If the injection point is at 19 m the profile towards the IP is much wider.
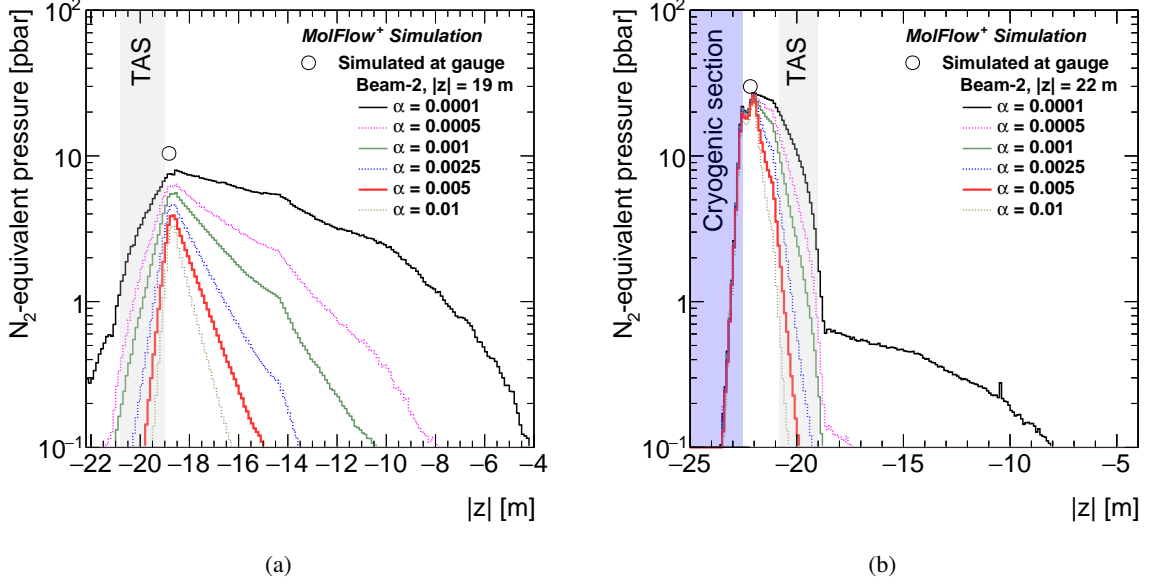
Figure 4: Pressure profiles at (a) 19 m and (b) 22 m as simulated with MOLFLOW+ for different assumptions of α. The profile for the expected value, $\alpha = 5 \times 10^{-3}$, is indicated by the thicker line. The MOLFLOW+ simulations also provide an estimate of the pressure at the relevant vacuum gauge, which can be used to scale the simulation results to the pressure actually measured in any particular fill, as is detailed in Section 6.2. The blue shaded area in (b) indicates the cryogenic region of the inner triplet.

4 Beam background simulations with FLUKA

Most LHC beam background simulations [8] are performed with the FLUKA Monte Carlo simulation code. Recently these have been extended [11] to include hit simulation and trigger emulation in the ATLAS sub-detectors that are relevant for studies of BIB. Thus the FLUKA simulations can be used to predict the efficiency of ATLAS to detect a beam-gas event as a function of its z-position.

The FLUKA simulations are performed as outlined in Ref. [11]. Beam-gas events are modelled as inelastic p-H scattering and the z-coordinates are sampled from the simulated pressure profiles, which are described in Section 3.5. For the nearby pressure bumps, i.e. $|z| < 23$ m, the position of the beam-gas interaction in the xy-plane is determined from the offset due to the vertical crossing angle and smeared according to the divergence caused by the β-squeeze and transverse emittance of the beams. In all simulations $185 \, \mu$rad and 40 cm are assumed for the crossing half-angle and β^*, respectively. These do not match the values given in Table 1 for all fills but the results depend only very weakly on the exact values of these parameters. In the case of the two distant pressure bumps, the transverse position of the event is placed on the ideal beam orbit and the shower is transported with FLUKA to a virtual interface plane at $z = 22.6$ m where particles are picked up by the ATLAS simulation, as described in Ref. [11]. In these computing-intensive LHC simulations, where particle showers are tracked in the accelerator structure and LHC tunnel over more than 100 metres, the primary p-H collisions have a uniform z-distribution of ± 5 m around the centre of each pressure bump. For the ATLAS simulations the events are selected according to the calculated pressure bump profiles along z. This allowed different pressure profiles to be studied, using the same set of events from the LHC simulations.

Fake-jet events are rare, and the number of events available from the LHC simulations determines the

14

statistical uncertainty: 9.5 million and 22.5 million events were selected for the 58 m and 151 m locations, respectively. As practically all fake jets are generated by radiative energy losses of muons, only these were picked up at the interface plane for further transport through ATLAS.

Obtaining a sufficient number of BIB events in the BCM background simulations is not an issue for any of the pressure bump locations. Thus only a small fraction of the events produced in the LHC simulations was used: 2×10^4 for the pressure bumps at 58 m and 2×10^5 for the 151 m location. For the nearby bumps, where the efficiency is very high, 8000 events, sampled from the pressure profiles, sufficed to obtain a negligible statistical error. All particles were transported until their energy fell below 100 keV, which is lower than the hit threshold of the BCM modules. In order to account for the dead-time of a BCM module, only the first hit within the ± 12.5 ns window, centred around the bunch passage at the IP, was considered for any individual module.

5 Background versus measured pressure

5.1 Determination of pedestal and bump pressure

During normal operation the BIB is dominated [14] by beam-gas interactions, distributed along the LSS and adjacent arc [11]. The gas injection causes localised pressure bumps into this distributed source. The observed background (B) is therefore parameterised as a function of the change of local pressures ($\Delta P(z_i)$) reported by vacuum gauges at locations z_i:

$$B = C + \sum_i \omega(z_i) \Delta P(z_i),$$

(6)

where z_i, with $i = 1 - 4$, refers to the four pressure bump locations and the pressure differences are measured with respect to the value prior to the gas injection. The parameter $\omega(z_i)$ relates $\Delta P(z_i)$ and the change of detected background while C describes the pedestal BIB level, arising from beam-halo losses at the TCT collimators and from beam-gas interactions in the absence of the pressure bump. Another minor contribution to C, for fake jets, comes from energy depositions by cosmic rays.

The accuracy with which $\Delta P(z_i)$, as measured by a vacuum gauge, reflects the pressure at the beam line depends on the local configuration of the vacuum equipment. In addition, the local pressure measurements provide no information on how far the injected gas spreads in the beam pipe, i.e. what is the gas density profile traversed by the beam. The dependence between $\Delta P(z_i)$ and the gas density, integrated along the beam trajectory, is reflected in the value of $\omega(z_i)$, which therefore differs from the absolute BIB detection efficiency that is discussed in Section 6. Since BIB is generated only by the incoming beam, Eq. (6) is evaluated separately for positive and negative z.

Figure 5 shows, as an example, the BCM background rates and pressures at 58 m and 151 m for beam-1 in fill 6239. The pedestal background, C, is determined, both for BCM and fake-jet rates, by averaging over the grey-shaded area indicated in Figure 5. The pressures reported by the selected gauges are averaged over the same period in order to determine the corresponding pedestal pressures. Figure 5 reveals that after the gas injection is terminated the pressure does not promptly return to its initial value, i.e. some pressure, additional to the pedestal, remains when further bumps are introduced at other locations. This residual, however, is at the percent level or below and therefore has no significant impact on the value of $\Delta P(z_i)$.
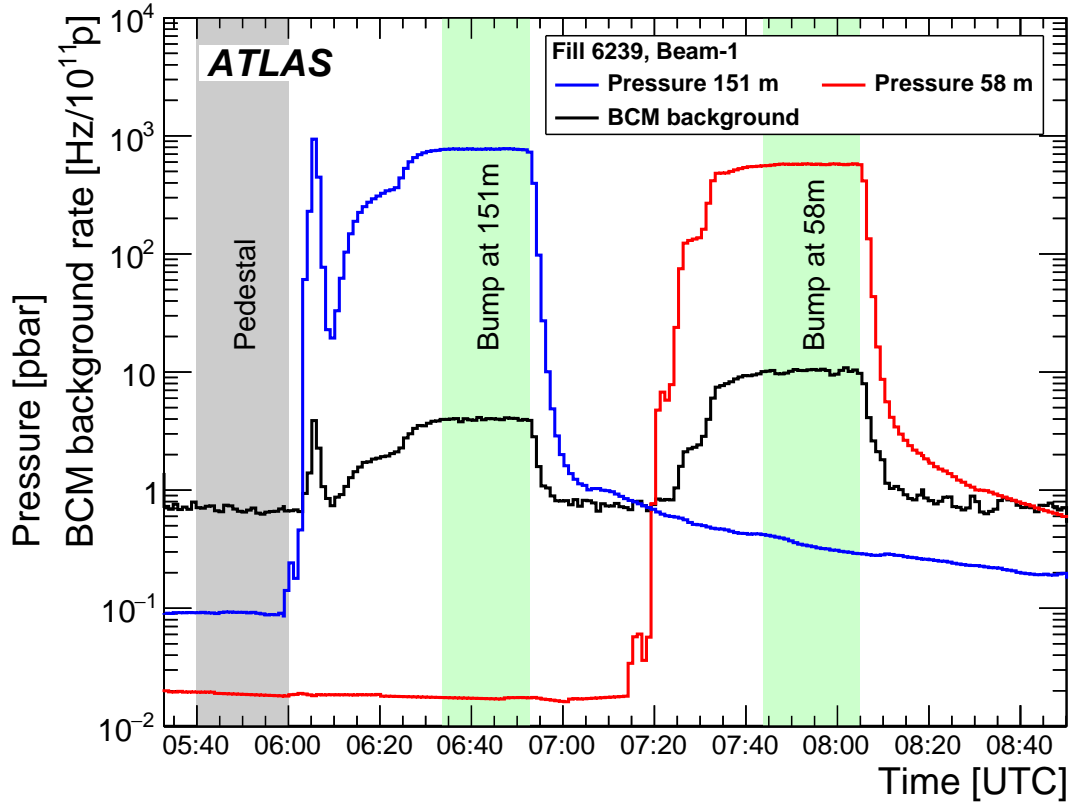
Figure 5: BCM background observed on beam-1 in fill 6239 and pressures measured by the vacuum gauges at $z = 58\,\mathrm{m}$ and $z = 151\,\mathrm{m}$. The grey-shaded area before the first bump indicates the time periods over which the pedestal pressure and background are averaged. The green shaded areas correspond to the averaging over the stable pressure periods of each of the two bumps.

The background rates and pressures due to the gas injection are taken from the green-shaded time intervals, which correspond to the stable pressure periods at the top of each bump. For each fill and pressure bump these shaded areas are determined by eye, requiring that the quality of the pressure and background measurements is as good and stable as possible throughout each period. In particular, periods obviously affected by instrumental noise or beam instabilities, not related to the test itself, are excluded.

5.2 Calculation of the $\omega(z_i)$ parameters

The rate of BIB, especially the beam-gas component, depends on the bunch intensity and residual pressure around the accelerator ring. The latter varies with the total beam intensity. This variation, however, is a function of the z-location, and the information available is insufficient to take all local pressure changes into account when propagating C. Therefore only the intensity decrease of the unpaired bunches is considered when propagating C to later times.

The pedestal C is subtracted from the background rate B, measured at maximum bump pressure, i.e. the periods indicated by the green shades in Figure 5. The $\Delta P(z_i)$ is determined as the difference between the

pressure in the green- and grey-shaded periods.

Since only one pressure bump at a time is introduced per beam, $\omega(z_i)$ can be solved from Eq. (6):

$$\omega(z_i) = \frac{B - C}{\Delta P(z_i)} = \frac{\Delta B}{\Delta P(z_i)}, \tag{7}$$

which is the same as Eq. (1).

Both, $B - C$ and $\Delta P(z_i)$ are evaluated separately for each LB in the green shaded area.

The final $\omega(z_i)$ for each z-location is obtained by averaging over all LBs in the green-shaded area of the corresponding pressure bump. The uncertainties on the mean values are estimated from the LB to LB variation. Upon insertion of the constant C and the obtained $\omega(z_i)$-values, Eq. (6) represents a global parameterisation of the BIB as a function of local pressure changes with time.

5.3 Parameterisation results

Figure 6 compares some representative BIB predictions, using the pressure parameterisation defined in Eq. (6), with the observed background. The data-points outside of the shaded areas, shown in the plots, are not included when determining the parameters $\omega(z_i)$. Thus any background anomalies that are not explained by the pressures at the considered gauges appear as differences instead of biasing the $\omega(z_i)$-values. Equation (6) agrees with the data also at the right edge of each plot. This confirms that the variation of C is negligible over the short duration of the tests, even though a correction with the overall decrease of dynamic pressure has not been applied.

Ideally $\omega(z_i)$ should be determined from a stable period around the maximum bump pressure. For several bumps, especially those at 19 m and 22 m, the pressure, however, could not be stabilised at a plateau value. In these cases a range with as stable as possible a pressure was selected, while taking care to maintain a reasonable number of events. In any case, the effect of a pressure variation should largely cancel since $\omega(z_i)$ is the ratio between the observed background and measured pressure and is evaluated for each LB separately. Thus $\omega(z_i)$ is constant, as long as the background change is proportional to the change of the pressure. Should, however, this proportionality be violated by a different time dependence of the two quantities, then this will be reflected in the uncertainty of $\omega(z_i)$ such that it includes in addition to statistical fluctuations also an unresolved systematic component. Such a non-linearity might appear, especially, at the start and end of the gas injection when the pressure bump profile is not yet, or not any more, stabilised.

In fill 7212 the tests started with a pressure bump at 19 m. Figure 6(a) shows that initially the pressure fit follows the rise of the background very closely. The pressure could not be perfectly stabilised at the target level but was gradually decreasing with time, as was the background rate. When the heating of the NEG cartridge was terminated, at about 20:00 UTC, the pressure dropped back to the initial value within about 20 minutes but the background remained at a higher level. Thus the 22 m pressure bump started with a factor of about two offset with respect to the initial pedestal background. The level, however, still was only about 10% of that at the top of the bump. An interesting feature of the leading edge of the 22 m pressure bump is that the background rises more rapidly than the pressure and overshoots the parametrisation in the first few minutes after the maximum pressure is reached. A possible reason for this is discussed in Section 6.4. No stable pressure could be established for the 22 m bump; both pressure and background dropped by about a factor of three over the shaded region which was considered for the averaging. When
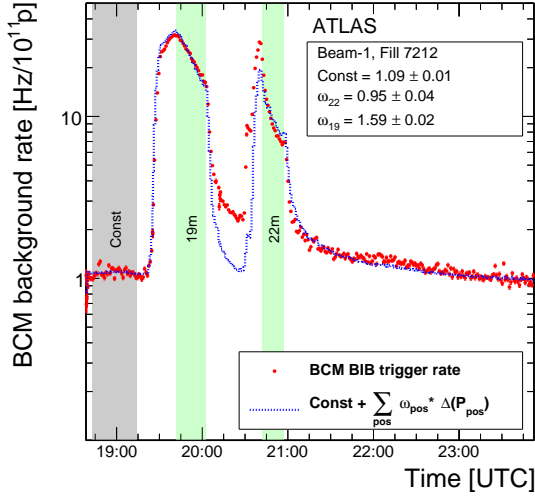
(a)
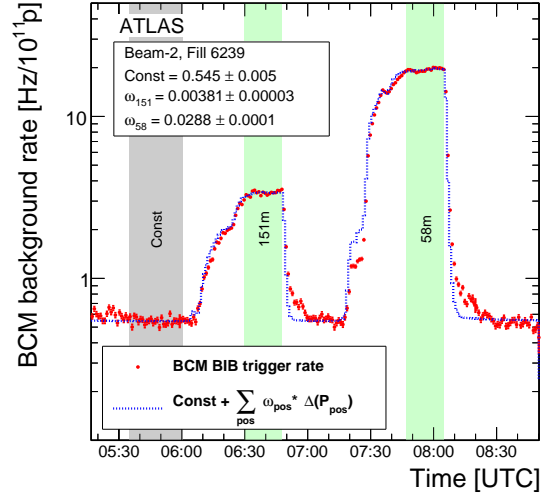
(b)
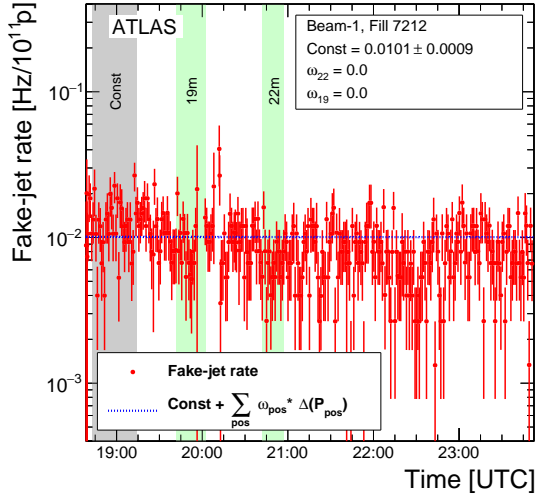
(c)
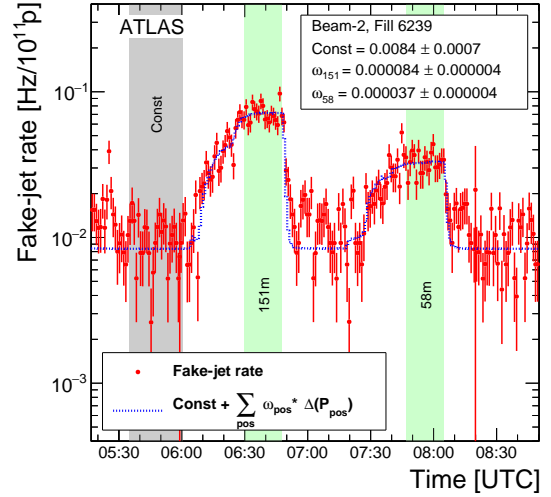
(d)

Figure 6: Comparison of BIB predictions using Eq. (6), with the observed (a) BCM and (c) fake-jet backgrounds from beam-1 pressure bumps at 19 m and 22 m in fill 7212. Figures (b) and (d) show the corresponding results at 58 m and 151 m for BCM and fake jets, respectively, for beam-2 in fill 6239. Only the data in the shaded regions are used to determine the parameters C and $\omega(z_i)$, which are needed in Eq. (6) to produce the dotted blue histogram. The time-dependence arises from the time variation of the local pressures $P(z_i)$.

the gas injection was terminated it took about 2 hours for the background and pressure to return to their initial levels.

Figure 6(c) shows that no additional fake jets can be resolved from the pedestal for the 19 m and 22 m pressure bumps. This is the case also for all other fills where gas was injected at these nearby locations. On the right side of Figure 6(c) the parameterisation overestimates the data. This is due to a separation of the beams at about 20:30 UTC, which causes a drop of the jet background from ghost collisions. Despite the

18

Table 3: Values of the pedestal background (C) and $\omega(z_i)$ averaged over all fills where the corresponding pressure bump was introduced. The uncertainties include the statistical variation within any given fill but are dominated by the fill-to-fill variation. As explained in the text, they might also include a component due to a non-linearity between measured pressure and observed background.

	Unit	BCM background rate		Fake-jet background rate	
		Beam-1	Beam-2	Beam-1	Beam-2
C	Hz/$10^{11}\,p$	0.80 ± 0.09	0.60 ± 0.07	0.012 ± 0.002	0.012 ± 0.002
$\omega(151\,\text{m})$	Hz/($10^{11}\,p \cdot$pbar)	$(4.2 \pm 0.2)\times10^{-3}$	$(3.4 \pm 0.5)\times10^{-3}$	$(8.8 \pm 0.5)\times10^{-5}$	$(8.1 \pm 0.8)\times10^{-5}$
$\omega(58\,\text{m})$	Hz/($10^{11}\,p \cdot$pbar)	$(1.8 \pm 0.3)\times10^{-2}$	$(2.9 \pm 0.2)\times10^{-2}$	$(1.9 \pm 0.3)\times10^{-5}$	$(4.0 \pm 0.4)\times10^{-5}$
$\omega(22\,\text{m})$	Hz/($10^{11}\,p \cdot$pbar)	0.82 ± 0.03	0.610 ± 0.006	—	—
$\omega(19\,\text{m})$	Hz/($10^{11}\,p \cdot$pbar)	1.53 ± 0.05	0.80 ± 0.04	—	—

applied vertex veto some contribution of these remains in the pedestal that is derived from the grey-shaded period, which corresponds to a time when the beams were still colliding head-on.

Contrary to the nearby bumps, pressures were stable for the 58 m and 151 m bumps in fill 6239, shown in Figures 6(b) and 6(d) for BCM and fake-jet rates, respectively. The pressure parameterisations follow very closely the BCM backgrounds, except for a minor overshoot on the rising edge of the 58 m bump and a slightly faster return to the initial level. Excess jet rates are clearly resolved for these distant pressure bumps, even though the pedestal level is rather noisy.

A common feature of several pressure bumps is that when the outgassing is stopped, the background decays slower than the measured pressure. This effect is particularly clear at 19 m and less pronounced or totally absent at the three other locations. A possible explanation is that some gas that has diffused far into the beam pipe is pumped out slower, i.e. when the outgassing from the NEG is stopped the low pressure is quickly re-established in the vicinity of the NEG cartridge where the gauges and additional ion pumps are located. Further away along the beam pipe a small fraction of the injected gas seems to reside for longer, maintaining a background excess. This is discussed in more detail in Section 6.

The $\omega(z_i)$ values obtained from Eq. (7) and averaged over all relevant fills are listed in Table 3. They have units of Hz/$10^{11}\,p$ per pbar because they express the change of the observed background rate with respect to the measured N_2-equivalent pressure change. Since the $\omega(z_i)$-values are based on the pressure measurement and not on the actual amount of additional gas traversed by the beam, they are not exactly comparable for locations with different vacuum gauge configurations. Nevertheless, they still give some indications of the relative importance of background sources as a function of z. The general trend is that the efficiency of the BCM to detect beam-gas events decreases as the distance between the pressure bump and the IP increases. This is expected from the fact that the BCM probes the BIB at very small radii; even from beam-gas collisions only a few metres from the IP some secondaries can reach the radial range of the BCM sensors. This is consistent with simulations [11], where the efficiency is found to increase between $z \approx 5$ m and $z \approx 10$ m and then stay roughly constant up to $z \approx 25$ m. Beyond this the attenuation in accelerator components, notably the TAS, and the lateral spread of the shower start to reduce the probability of a BCM module to be hit.

One striking observation that can be made from Table 3 is that for the BCM background, $\omega(19\,\text{m})$ and $\omega(22\,\text{m})$ are significantly higher for beam-1 than for beam-2 although the beam line, the instrumentation and the BCM detector are symmetric on both sides. This finding, which here is based purely on data, has implications for the discussion in Section 6.

Table 4: Ratio (BCM/Jet) of the average values given in Table 3. The simulated ratios are derived from Tables 8 and 9 in Section 6, i.e. their uncertainties include only the statistical errors given there. No simulations exist for the value of C.

Position	Beam-1	Beam-2	Simulation
C	64±11	49±8	N.a.
58 m	950±230	740±80	790 ± 45
151 m	48±3	41±7	52 ± 2

Contrary to the BCM, the probability to observe fake jets increases with distance from the IP. This is explained by the fact that fake jets are produced by energetic muons that reach the calorimeter radii only if they are produced sufficiently far away. In particular, if they originate from beyond the D1 magnet they are deflected by its field, which increases their spread in the horizontal plane.

The rates reported in Table 3 provide a purely experimental determination of the relative sensitivity of ATLAS to detect BIB through BCM trigger and fake-jet rates: since for any given position the backgrounds originate from the same pressure distribution, all unknown factors, especially the pressure profile, cancel from the ratios of the BCM and fake-jet rates. These ratios, presented in Table 4, reveal several interesting features:

- The ratio of the constant terms is slightly higher for beam-1. Table 3 shows that this difference is entirely due to an asymmetric BCM background. The BCM sensitivity is highest for nearby beam-gas events, which do not produce fake jets. Thus a beam-1/beam-2 ratio larger than one suggests that there are more nearby beam gas events on the incoming beam-1 side, i.e. for an unknown reason the vacuum in the vicinity of ATLAS seems worse on that side.

- For both distant pressure bump locations the BCM/Jet ratios are consistent between the two beams, as would be expected from the symmetry of the beam line and the ATLAS detector.

- The BCM/fake-jet ratio is almost 20 times larger for beam-gas events at 58 m than at 151 m.

- The agreement with simulations is nearly perfect. Since the simulations are done with the same methods as in Ref. [11], these measurements provide a valuable benchmark for that earlier work.

- The most interesting observation arises from a comparison with Ref. [14], where the ATLAS beam backgrounds resulting from proton losses on the TCTs, at $|z| \approx 145$–148 m from the IP, are reported. In those data, at $\beta^* = 40$ cm, the BCM/fake-jet ratio was found to be 5.4 ± 0.3 for beam-1 and 6.1 ± 0.3 for beam-2. The corresponding ratios in Table 4 for the 151 m pressure bump are higher by a factor of about seven. The explanation of this substantial difference is deferred to the end of Section 8.1.

6 Absolute beam-gas detection efficiency

6.1 Definition

The values of $\omega(z_i)$, derived from Eq. (7), are based entirely on data and show that the observed background rates are strongly correlated with the magnitude of the locally introduced pressure bumps. Although they

provide an experimental determination of the BCM/fake-jet background ratio as a function of the pressure bump location, they do not allow for determining the real efficiency to detect beam-gas events by the BCM ($\varepsilon_{\text{BCM}}(z)$) or as fake jets ($\varepsilon_{\text{JET}}(z)$) from different z-locations. Furthermore, since the $\omega(z_i)$ are specific to the local configuration of vacuum gauges and NEG cartridges used to inject the gas, they are not even suited to accurately determine the relative efficiency between different z-locations.

The generally good agreement of the time-dependence between the observed background and the measured pressure, seen in Figure 6, confirms that the introduced pressure bumps dominate the background rates. Other contributions are negligible, especially for the BCM.

The ultimate goal of these pressure bump tests was to determine the absolute efficiency of ATLAS to detect beam-gas events as a function of their z-location. This, however, requires that R_{BG} is known for each bump. Once R_{BG} is determined, $\varepsilon_{\text{BCM}}(z)$ and $\varepsilon_{\text{JET}}(z)$ are obtained from Eq. (2), i.e. as the ratio between the observed background rate increase and the additional R_{BG} due to the introduction of the pressure bump.

6.2 Absolute scale of the pressure profiles

The pressure profile calculations, described in Section 3.5, are performed for a single outgassing rate of the NEG cartridge. In order to adjust the calculations to the conditions of a particular fill the pressure measurement provided by the vacuum gauges is invoked: the calculated density profiles ($\rho_{\text{calculated}}(z)$) are rescaled, as illustrated in Figure 7(a), such that the calculated P at the gauge position matches the measured P, averaged over the period considered for the analysis. Formally the rescaling can be described as

$$\rho_{\text{rescaled}}(z) = \frac{P_{\text{measured}}(\text{gauge})}{P_{\text{calculated}}(\text{gauge})}\rho_{\text{calculated}}(z).\tag{8}$$

The right side of Eq. (8) is equivalent to the pressure ratio and density integral in the denominator of Eq. (2). The rescaling brings two advantages:

1. it accounts for the measured pressure data, and

2. it renders the single pressure profile calculation universal, i.e. the same profile, at a given location, is equally applicable to all fills.

It is important to emphasise that this rescaling procedure is in no sense a correction introduced to compensate for deficiencies of the calculation. It is purely a factor applied to adjust the assumptions made in the calculations to the observed conditions of a particular fill.

The gauges report the nitrogen equivalent pressure ($P_{\text{N}_{\text{eq}}}$). In order to compare this with the calculated density of residual gas molecules n_i, the latter is converted into $P_{\text{N}_{\text{eq}}}$ at room temperature using the formula

$$P_{\text{N}_{\text{eq}}} = k_B T \sum_i r_i n_i,\tag{9}$$

where k_B is the Boltzmann constant and r_i the gas-dependent gauge response taken from Table 2. The sum runs over all gas species. The ratio of measured and calculated $P_{\text{N}_{\text{eq}}}$ is used in Eq. (8) to perform the rescaling of the calculated gas density. The MoLFLow+ simulations provide the pressure at the gauge location and consider only the injected hydrogen, ignoring the other gases, which contribute only to the pedestal pressure. In this case only one single gas contributes to the pressure change, and the rescaling
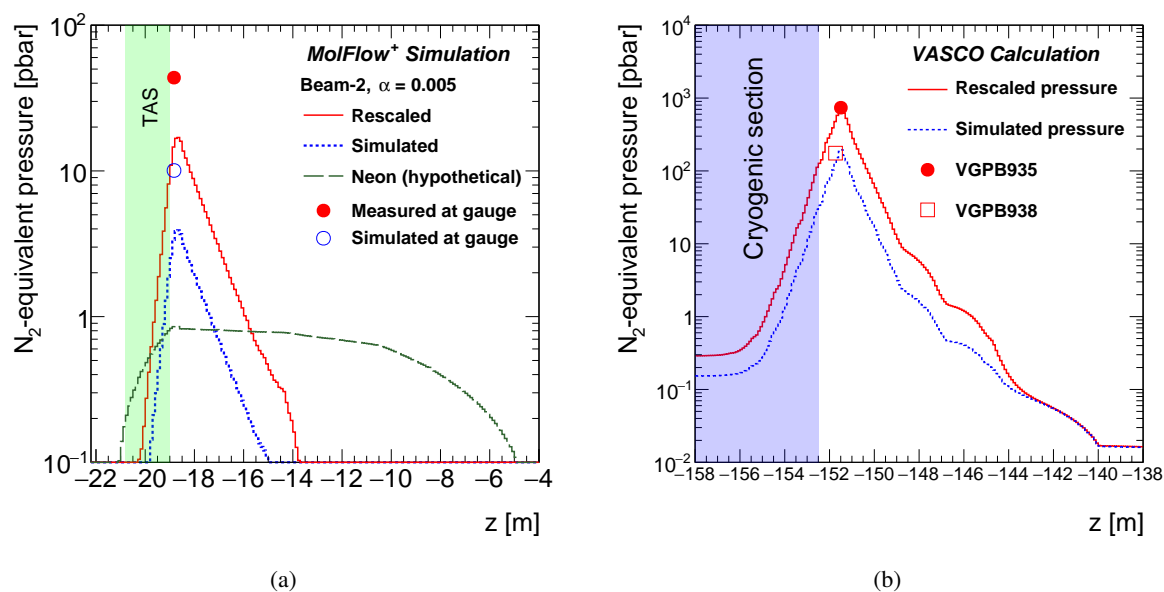
Figure 7: Illustration of the profile rescaling to the measured pressures in the case of beam-2. (a) MoLFLOW+-simulated pressure profiles at 19 m assuming $\alpha = 5 \times 10^{-3}$ before and after rescaling the calculations to the pressure reported by the vacuum gauge in fill 7212. The neon profile, shown in the figure, is normalised to a total of 6×10^{12} atoms, as is discussed in Section 6.4. (b) VASCO-calculated pressure profiles at 151 m before and after rescaling the value at the profile maximum to the value reported by the VGPB935 gauge in fill 6239.

procedure is straightforward. The procedure is slightly more complicated at 58 m and 151 m where VASCO is used to calculate the pressure profiles. VASCO takes into account also the other gases, which contribute to the pressure in the absence of the gas injection, so the breakdown of $P_{N_{eq}}$ into individual gas densities is ambiguous. The injected gas, however, dominates the pressure in the bump by orders of magnitude. Since it is assumed to be hydrogen, only the partial pressure of hydrogen is changed in the rescaling procedure. Contrary to MoLFLOW+, VASCO calculations do not consider the gauge explicitly. Thus the beam-line pressure at the z-location of the gauge is compared with the measured value, i.e. $P_{\text{calculated}}(\text{gauge})$ is replaced by $P_{\text{calculated}}(z_{\text{gauge}})$ in Eq. (8). The pressure profiles for the bump at $z = 151$ m are shown in Figure 7(b). At this location two vacuum gauges, separated by only 25 cm, provide pressure measurements. A significant difference between the values from the two gauges is seen. The gauge VGPB935 is located next to the NEG cartridge used to emit the gas and is therefore considered to provide the more relevant measurement. The mismatch, seen in Figure 7(b), between the rescaled profile and the pressure reported by the VGPB938 gauge is discussed in Section 7.1.3.

The calculated pressure profiles are rescaled such that they correspond to the conditions of a particular fill. Then the integral over the rescaled profiles is used in Eq. (4) to determine the increase of R_{BG} due to the introduction of the bump. The results, as a function of α, are shown in Figure 8 for all nearby, i.e. 19 m and 22 m, bumps. For each fill and pressure bump, the R_{BG} that equals the observed BCM background rate increase is indicated on the curves by an asterisk. For all fills these points agree rather well on a unique α value for any given bump location. An R_{BG} lower than the indicated value is unphysical, as it would imply that more beam-gas events are detected than produced. The α values for which MoLFLOW+ gives the same R_{BG} as VASCO are indicated by the open circles. With the exception of the 22 m pressure bump in beam-2, they all fall into the unphysical region.
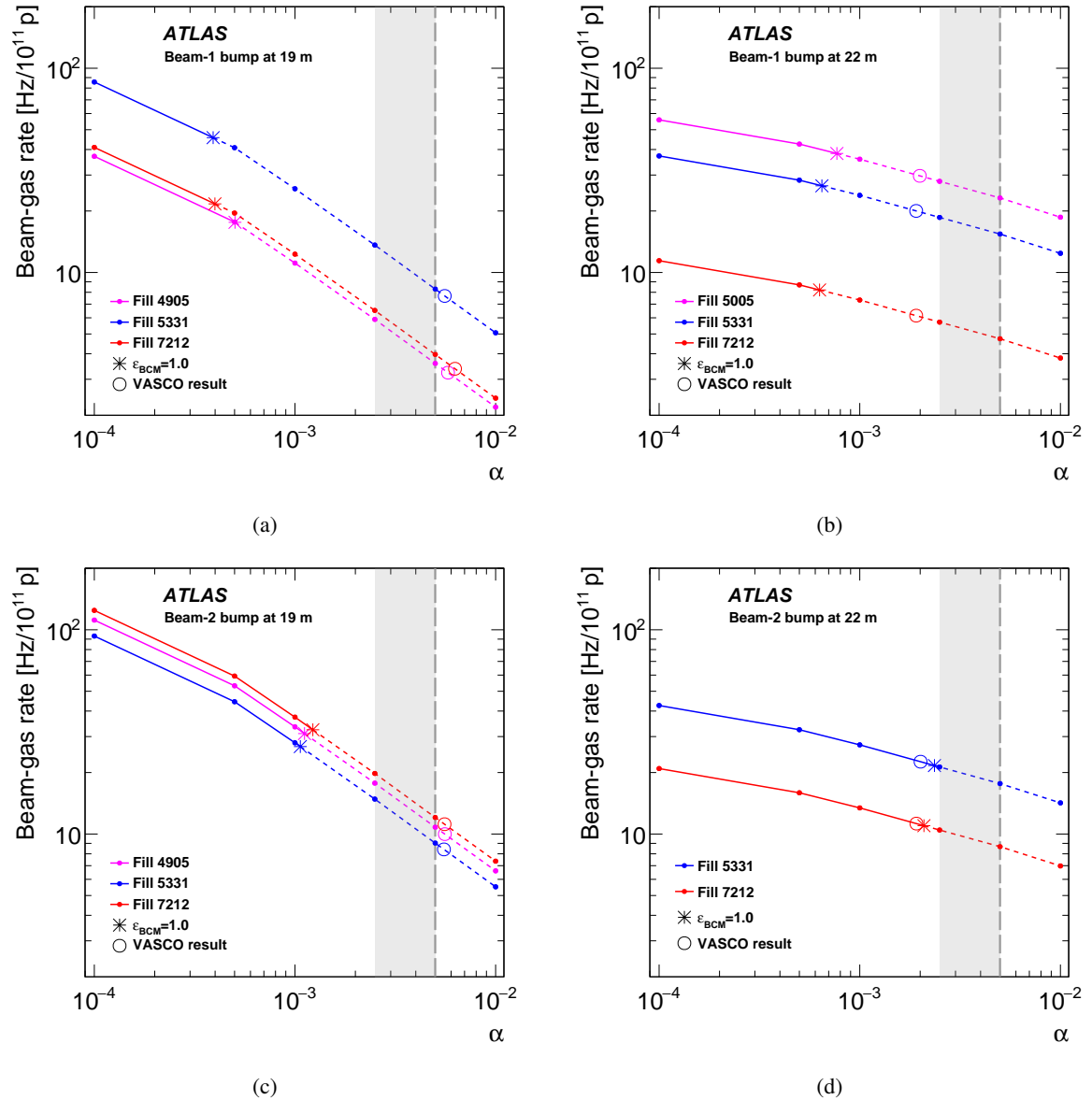
Figure 8: Beam gas rates in the 19 m and 22 m bumps, calculated from the pressure profiles obtained with MoLFLow+ when assuming different values of α. The dashed vertical line indicates the standard assumption for α and the adjacent shade shows the reasonable range of downward variation. The asterisks indicate the point where R_{BG} equals the observed BCM background rate increase in the given fill, i.e. $\varepsilon_{BCM}(z) = 1.0$. The dashed part of the lines represents the unphysical region $\varepsilon_{BCM}(z) > 1.0$. The open circles show, for each individual fill, the α values for which MoLFLow+ gives the same R_{BG} as VASCO.

6.3 Determination of BIB detection efficiencies

Tables 5 and 6 give, for each individual fill, the BIB detection efficiencies that are obtained as the ratio between observed additional background events and the estimated R_{BG} at the pressure bump location. It is expected that α is around 5×10^{-3} for gases, including H_2, which are pumped by the NEG coating of the beam-pipe wall. Therefore the MoLFLow+ profiles corresponding to $\alpha = 5 \times 10^{-3}$ are used for the

Table 5: Ratio between the BCM background rate and the estimated R_{BG} due to the pressure bump. A '—' means that no bump was introduced in that position in the given fill. The uncertainties are based on the LB-to-LB variation, i.e. are mostly statistical but reflect also a possible non-linearity between the pressure and background measurements. The values for the 19 m and 22 m bumps correspond to $\alpha = 5\times10^{-3}$. As discussed in the text, as efficiencies they are unphysical, but they serve here only to indicate the consistency of data obtained in different fills.

LHC Fill	Position, beam-1			
	19 m	22 m	58 m	151 m
4905	4.9 ± 0.4	—	$(2.84 \pm 0.03)\times10^{-2}$	—
5005	—	1.65 ± 0.02	$(2.99 \pm 0.02)\times10^{-2}$	—
5331	5.5 ± 0.2	1.7 ± 0.2	$(2.63 \pm 0.03)\times10^{-2}$	$(6.34 \pm 0.08)\times10^{-3}$
6239	—	—	$(3.13 \pm 0.03)\times10^{-2}$	$(7.29 \pm 0.04)\times10^{-3}$
7212	5.5 ± 0.3	1.7 ± 0.2	—	—

LHC Fill	Position, beam-2			
	19 m	22 m	58 m	151 m
4905	2.9 ± 0.3	—	$(3.29 \pm 0.03)\times10^{-2}$	—
5005	—	—	$(4.07 \pm 0.03)\times10^{-2}$	—
5331	3.0 ± 0.4	1.23 ± 0.07	$(4.7 \pm 0.1)\times10^{-2}$	$(4.88 \pm 0.06)\times10^{-3}$
6239	—	—	$(5.46 \pm 0.03)\times10^{-2}$	$(6.47 \pm 0.07)\times10^{-3}$
7212	2.69 ± 0.08	1.27 ± 0.01	—	—

Table 6: Ratio between the fake-jet background rate and the estimated R_{BG} due to the pressure bump. A '—' means that no bump was introduced in that position in the given fill. The uncertainties are based on the LB-to-LB variation, i.e. are mostly statistical but reflect also a possible non-linearity between the pressure and background measurements. No ratios are given for the 19 m and 22 m bumps, where no excess of fake jets could be resolved from the pedestal background.

LHC Fill	Position, beam-1		Position, beam-2	
	58 m	151 m	58 m	151 m
4905	$(2.6 \pm 0.6)\times10^{-5}$	—	$(5.3 \pm 0.8)\times10^{-5}$	—
5005	$(2.7 \pm 0.4)\times10^{-5}$	—	$(6.3 \pm 0.5)\times10^{-5}$	—
5331	$(1.5 \pm 0.8)\times10^{-5}$	$(1.4 \pm 0.1)\times10^{-4}$	$(6.7 \pm 0.7)\times10^{-5}$	$(1.20 \pm 0.08)\times10^{-4}$
6239	$(2.6 \pm 0.5)\times10^{-5}$	$(1.49 \pm 0.07)\times10^{-4}$	$(7.0 \pm 0.5)\times10^{-5}$	$(1.46 \pm 0.06)\times10^{-4}$

nearby pressure bumps. The pedestals of R_{BG} and the background event rate, in the absence of a pressure bump, are determined from the grey-shaded areas in Figure 6 (and equivalent figures for other fills) and are subtracted before forming the ratio. Despite varying beam conditions, the efficiencies in different fills are consistent to better than 30%. The only exception is the $\varepsilon_{BCM}(58\,m)$ for beam-2, which is about 60% higher in fill 6239 than in 4905.

The $\varepsilon_{BCM}(19\,m)$ and $\varepsilon_{BCM}(22\,m)$ values given in Table 5 exceed unity by a significant amount. This is obviously unphysical and therefore suggests that the density of gas traversed by the beam is severely underestimated. Figure 8 indicates that α should be much smaller than assumed in order to increase R_{BG}
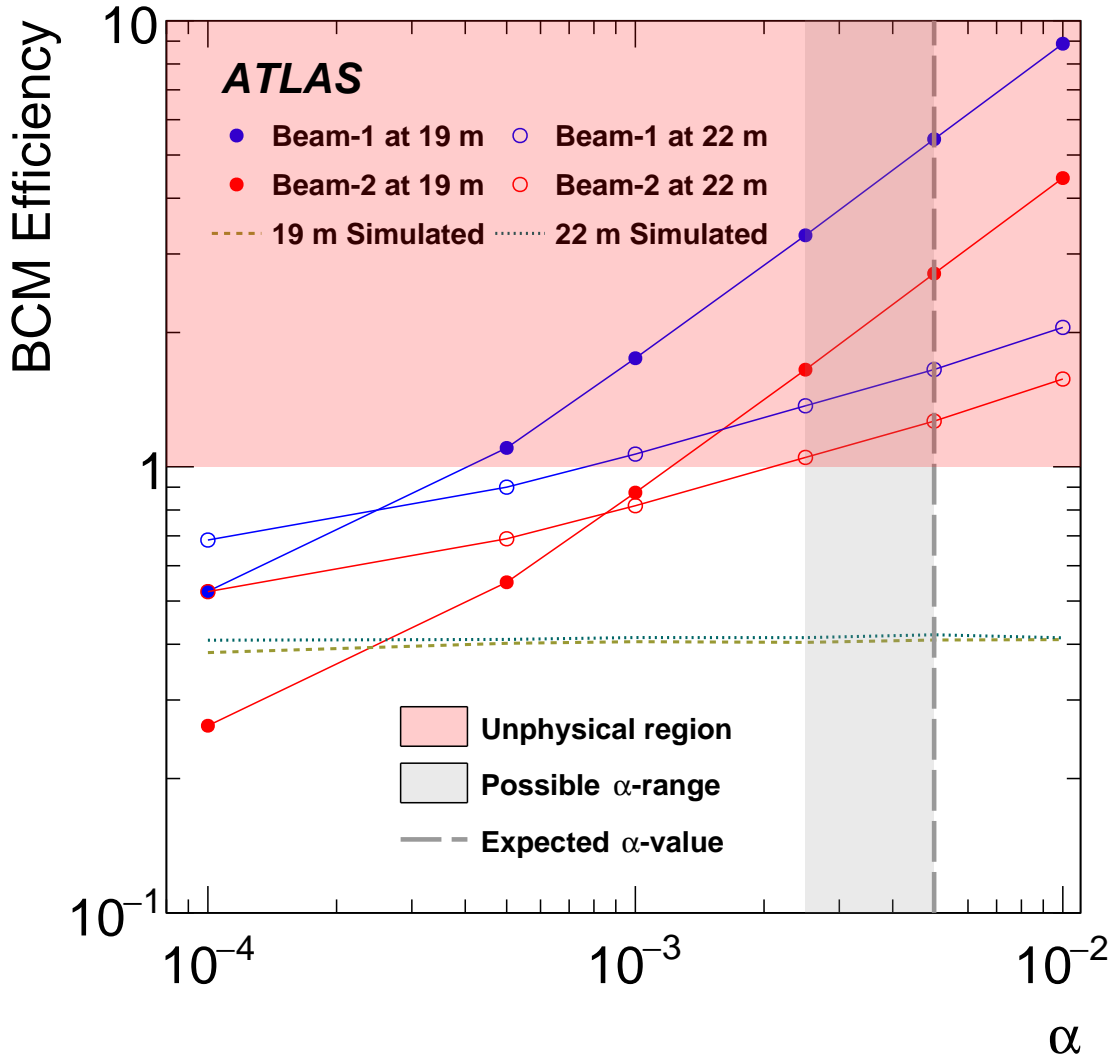
Figure 9: Beam-gas induced background detection efficiency of the BCM as a function of α assumed in the MoLFLow+ simulations. The dashed vertical line indicates the standard assumption for α, and the adjacent grey shade shows the reasonable range of downward variation. The values are averaged over all fills in which a pressure bump at the indicated location was introduced, i.e. those shown in Figure 8. In all cases the error bars due to the fill-to-fill variation are smaller than the symbols. The red-shaded area indicates the unphysical region where the number of detected background events would exceed the number of produced beam-gas collisions. The simulated $\varepsilon_{\text{BCM}}(z)$ should not depend on α, but a weak dependence arises because the z-locations of the events are sampled from the pressure profiles shown in Figure 4. Especially at 19 m the average of this distribution moves away from the IP when α increases.

to the same level as the observed background. This is even better illustrated by Figure 9 where $\varepsilon_{\text{BCM}}(z)$, averaged over all relevant fills, is plotted as a function of α.

Several interesting observations can be made from Figure 9:

- for both locations, $\varepsilon_{\text{BCM}}(z)$ for beam-1 is systematically higher than for beam-2,

- the dependence of $\varepsilon_{BCM}(z)$ on α is much stronger for the 19 m than for the 22 m pressure bumps,

- the FLUKA simulations predict almost equal $\varepsilon_{BCM}(z)$ for beam-gas events at the 19 m and 22 m locations.

The last observation is particularly interesting: while the absolute rates obtained from the simulations have substantial uncertainties, many of these cancel from the ratio $\varepsilon_{BCM}(19\,m)/\varepsilon_{BCM}(22\,m)$, notably those associated with the BCM hit and trigger simulation, beam-gas event generation and accuracy of the beam-line geometry description at $z < 19\,m$. Therefore this ratio is considered to be a much more reliable prediction than the absolute value of $\varepsilon_{BCM}(z)$, obtained from the simulations. This means that $\varepsilon_{BCM}(19\,m) = \varepsilon_{BCM}(22\,m)$ can be considered a rather strong constraint, although it arises from the FLUKA simulations.

Figure 9 is based on the MOLFLOW+ simulations, assuming that only hydrogen is released from the NEG cartridge. The points of intersection of the curves suggest that α must be slightly below 10^{-3} for beam-2 and about three times lower for beam-1 in order to obtain $\varepsilon_{BCM}(19\,m) = \varepsilon_{BCM}(22\,m)$ for a given beam.

Table 3 reveals that the ratio between BCM background and measured pressure is highest for the 19 m bump on the beam-1 side, lowest for the 22 m bump on the beam-2 side and intermediate for the two other nearby locations. This is qualitatively consistent with the order of the curves in Figure 9 at $\alpha = 5 \times 10^{-3}$, i.e. the purely data-driven results also indicate a significant difference for the two sides of ATLAS.

An independent verification of the calculated pressure profiles is obtained by monitoring the pressure increase at 19 m when gas is injected at 22 m and vice versa. Since MOLFLOW+ provides the pressure at the gauges, this ratio can also be derived from the pressure simulations. A comparison of these measured and simulated ratios reveals that the best agreement is obtained for $\alpha < 10^{-3}$. This value, as well as the fact that it is found to be lower for beam-1 than beam-2, is in good agreement with Figure 9.

Such low values of α, and a large difference on the two sides of the IP, do not seem plausible [28]. One possible explanation for the apparently low and non-uniform α is that in addition to hydrogen, another gas, not considered in the MOLFLOW+ simulations, was emitted from the NEG cartridge.

6.4 Possible neon contribution

During each annual technical stop, the experimental beam pipe within $|z| < 22\,m$ is filled with ultra-pure neon to atmospheric pressure [35] in order to protect the pipe walls from accidental collapse during maintenance of the ATLAS experiment. Although noble gases are not pumped by NEGs, it is possible that some neon atoms reside on the large surface of very porous material of the NEG cartridge [36]. Upon heating, this neon would be released alongside the hydrogen.

Such a two-gas hypothesis could provide a plausible qualitative explanation for the apparently low α: α could well be close to the expected value of 5×10^{-3} for H_2, but since it is zero for neon, a sizeable amount of emitted neon could result in an apparent[5] α around, or even below, 10^{-3}.

There are two reasons why even a small amount of neon can have a significant impact on $\varepsilon_{BCM}(z)$:

---

[5] Apparent α refers to Figure 9, i.e. it is the α that produces the observed $\varepsilon_{BCM}(z)$.

1. Table 2 shows that the inelastic cross section for p-Ne scattering is five times larger than for p-H_2 but for the same density of molecules the vacuum gauge will report two times higher pressure for hydrogen than for neon. Thus, for the same measured pressure, R_{BG} in pure neon is about ten times higher than in pure H_2. In addition, the FLUKA simulations indicate that, due to the higher particle multiplicity, the efficiency of the BCM to detect p-Ne events is about 15% higher than for p-H collisions.

2. Since neon is not removed by the NEG coating of the beam pipe, i.e. $\alpha = 0$, its distribution can be expected to be much wider in z than for hydrogen. This is the case, especially, for the 19 m location, where the neon flow towards the IP is restricted only by the ion pump at $|z| = 3.7$ m. As a consequence the ratio between the total amount of gas traversed by the beam and the pressure measured at the gauge is likely to be much larger than for hydrogen.

Hydrogen is quickly absorbed by the NEG coating of the beam pipe, but if neon is emitted from the NEG at $z = -19$ m it will form a wide bump between $z \approx -8$ m and $z \approx -19$ m, as indicated in Figure 7(a). In order to be removed, this neon has to diffuse to the ion pumps, so it will reside in the beam pipe for a longer time than hydrogen. The neon profile shown in Figure 7(a) is obtained from MOLFLOW+, but since the rate of neon emission is not known, the (possibly time-dependent) mixing ratio of hydrogen and neon cannot be derived by combining the pressure data with the simulations. Thus only an approximate range of R_{BG} can be determined for the mixture, as is discussed in Section 7.1.2.

In the $|z|$-region where the neon is contained, according to the MOLFLOW+ simulations, $\varepsilon_{BCM}(z)$ is roughly constant [11]. Thus Eq. (4) can be used to estimate that $\sim 6 \times 10^{12}$ neon atoms are sufficient to lower $\varepsilon_{BCM}(19\,\text{m})$ below unity even if α is 5×10^{-3} for hydrogen. In order to verify if neon could be a viable explanation for the observations, dedicated laboratory tests were carried out by the CERN vacuum group [37]. In these tests a NEG cartridge was exposed to pure neon at atmospheric pressure for three days before re-establishing the vacuum. Then the heating on the NEG cartridge was turned on and released gas composition was monitored with a residual gas analyser and the pressure by a hot cathode vacuum gauge. The tests indicated that about $\sim 5 \times 10^{13}$ neon atoms were released from the cartridge over a 55 minute period of heating. This result has large uncertainties but it exceeds by almost an order of magnitude the amount needed to explain the present results. A detailed time dependence of the neon emission, however, is not determined in these tests. It is not clear if the neon is emitted gradually such that the total amount would scale with the heating time or predominantly soon after the heating of the NEG cartridge starts. The early rise and overshoot of the background in Figure 6(a), with respect to Eq. (6), suggests that a significant fraction of the neon is released promptly when the heating of the NEG starts: $\omega(22\,\text{m})$ is derived from Eq. (7) after this overshoot. If hydrogen dominates during that time, $\omega(22\,\text{m})$ will underestimate the BIB from the earlier gas composition if that is richer in neon.

No such overshoot is seen for the 19 m bump in Figure 6(a). A possible explanation is provided by the longer residence time, discussed above: compared to the 22 m bump, the total amount of neon varies less over time for the 19 m bump, i.e. neon contributes also during the time-interval used to determine $\omega(19\,\text{m})$. This argument is also consistent with the discrepancy between the background rate and the pressure parameterisation seen in Figure 6(a) after the 19 m bump: when the NEG heating is terminated, neon probably still resides far from the ion pumps, e.g. around $|z| \approx 10 - 15$ m, and causes an excess of beam-gas events.

Another observation that supports the hypothesis of neon emission is that a small pressure increase is observed on the other side of the TAS if the gas is injected at either 19 m or 22 m. The MOLFLOW+ profiles shown in Figure 7(a) indicate that when the NEG at $z = -19$ m is heated, practically none of the emitted

hydrogen can traverse the NEG-coated TAS if $\alpha = 5 \times 10^{-3}$ is assumed. However, the neon pressure on the opposite side, at $z = -22$ m, is non-zero and sufficient to cause the pressure gradient through the TAS to appear equivalent to $\alpha \lesssim 10^{-3}$. Without the annular pump at 3.7 m, the neon from an injection at $|z| = 19$ m would spread to the other side of the IP, cause some increase of BIB in the opposite beam, and thereby provide firm evidence for the two-gas hypothesis. Unfortunately the pump prevents this, as evidenced by the drop of the MoLFLow+-simulated neon pressure for $|z| \lesssim 10$ m in Figure 7(a).

Although these arguments are consistent with the neon emission hypothesis, and the laboratory measurements indicate the right order of magnitude of released neon atoms, they cannot be taken as a firm proof for the neon hypothesis but merely as an indication that it is a likely explanation for the unphysically high $\varepsilon_{\mathrm{BCM}}(19\,\mathrm{m})$ and $\varepsilon_{\mathrm{BCM}}(22\,\mathrm{m})$ values in Table 5. A firm verification would require further tests with a detailed analysis of the residual gas composition.

One feature, however, remains unexplained: the injection of neon takes place on the incoming beam-1 side, close to the 22 m NEG cartridge. Although this creates an asymmetry between the sides, it is unclear why more neon seems to be released from the NEG cartridge on the beam-1 side, although the entire ATLAS beam pipe is filled with neon at atmospheric pressure for several months during the annual technical stop.

7 Discussion of the level of systematic uncertainties

7.1 Uncertainties affecting the measured values

7.1.1 Common effects

The statistical errors, reported, e.g., in Tables 5 and 6, are in general negligible compared to systematic uncertainties, which comprise several contributions. Given the nature of the problem and, especially, the incomplete knowledge of the injected gas composition, only a qualitative discussion of the magnitude of the systematic uncertainties is provided.

In some cases, when the observed BIB is not well correlated with the pressure change, the ω-factor obtained from Eq. (7) depends on the averaging range. Such deviations appear, especially, at the rising and falling edges of the pressure bumps. For instance, if the averaging range for the 22 m pressure bump in Figure 6(a) would be moved earlier a higher value would be obtained. The effect of small variations of the averaging ranges was investigated and, as long as the rising and falling edges were excluded, the effect on the results was found to be negligible. A possible bias caused by erroneously excluding periods that appear suspicious would be revealed when averaging over several fills. The uncertainties reported in Table 3 are dominated by the fill-to-fill variation, and they are all of the order of 10% or less. Thus, any significant selection bias in the analysed fills can be excluded. As the same averaging periods are used in Section 6 to determine the absolute efficiencies, these fill-to-fill uncertainties apply also to $\varepsilon_{\mathrm{BCM}}(z)$ and $\varepsilon_{\mathrm{JET}}(z)$ and are included in their statistical errors.

A systematic uncertainty that affects both the ω factors and absolute efficiencies is the choice and accuracy of the vacuum gauge used for the pressure measurement. For the 19 m and 22 m bumps the gauges that provided the most consistent output in all relevant fills and for both beams were selected. Using an alternative gauge has an average effect of 25% at the 22 m location and no effect at all at 19 m. This is consistent with the expected gauge uncertainty of <10% for VGI gauges, used at 19 m and <30% for VGPB

gauges, used at 22 m. A gauge uncertainty of <30% is assumed also for the VGPB gauges used at the 58 m and 151 m locations.

A minor contribution to the uncertainty of the absolute efficiencies arises from the cross sections listed in Table 2. These affect R_{BG} through Eq. (4) and thereby the measured values of $\varepsilon_{BCM}(z)$ and $\varepsilon_{JET}(z)$. CH_4, CO and CO_2 contribute only to the pedestal beam-gas rate, which cancels from the final result. The uncertainty associated with the possibly present neon is entirely dominated by the lack of knowledge of the amount of that gas, as discussed in Section 7.1.2. Thus only the cross-section uncertainty of p-H_2 is relevant. For this the values in Table 2 can be compared with the proton–proton cross section from Ref. [38], which is about 38 mb at 6.5 TeV laboratory momentum. This is consistent with Table 2, and the fit in Ref. [38] suggests that the uncertainty is less than 5%, which is negligible compared to other contributions.

7.1.2 Nearby pressure bumps at 19 m and 22 m

It is evident from Section 6.4 that the possible emission of another gas, notably neon, in addition to hydrogen, constitutes a major uncertainty impacting the measured values of $\varepsilon_{BCM}(19\,m)$ and $\varepsilon_{BCM}(22\,m)$. Within this two-gas hypothesis not enough information is available to establish anything other than an estimated range. Figure 9 indicates that this range is rather limited: clearly R_{BG} cannot exceed the rate of detected additional events, i.e. the requirement $\varepsilon_{BCM}(z) \leq 1$ defines the upper limit. Other possible sources of spurious BCM background triggers, e.g. noise, ghost collisions or afterglow, are not affected by the introduction of the pressure bump and therefore are removed by the pedestal subtraction and by rejecting data in periods that are obviously affected by noise bursts or beam instabilities. The good consistency between individual fills, seen in Table 5, indicates that this cleaning is efficient and no significant anomalies remain in the data.

A lower bound for $\varepsilon_{BCM}(z)$ is more complicated to establish since in the two-gas hypothesis it arises from the maximum amount of neon that could contribute to the background. Figure 7(a) indicates that neon emitted at 19 m would create a wide pressure distribution extending from $|z| \approx 8\,m$ to the TAS, which coincides with the region where $\varepsilon_{BCM}(z)$ is roughly constant. The volume of the beam pipe in this z-range is ~70 litres. Thus every 10^{12} neon atoms would increase R_{BG} by about 7 Hz/10^{11} p. This can be compared with the curves in Figure 8: the highest R_{BG} required for $\varepsilon_{BCM}(19\,m) = 1$ is ~50 Hz/10^{11} p as indicated by an asterisk in Figure 8(a) for fill 5331. The laboratory tests indicate that up to 5×10^{13} neon atoms could be emitted by the NEG cartridge upon heating. Taking this as the maximum amount that could contribute would increase R_{BG} by about 350 Hz/10^{11} p. This adds to the ~10 Hz/10^{11} p of p-H events indicated in Figure 8(a) if α is assumed to be in the expected range $\sim 2.5 - 5 \times 10^{-3}$. Reaching $\varepsilon_{BCM}(19\,m) = 1$ requires $R_{BG} = 50$ Hz/10^{11} p, which means that 360 Hz/10^{11} p corresponds to $\varepsilon_{BCM}(19\,m) \gtrsim 0.15$. In all other cases 350 Hz of additional rate would have a larger effect. Since the FLUKA prediction of $\varepsilon_{BCM}(19\,m) = \varepsilon_{BCM}(22\,m)$ is considered reliable and as there is no reason to believe that $\varepsilon_{BCM}(z)$ would be different for the two beams, the highest lower limit of $\varepsilon_{BCM}(z)$ applies to all cases. This implies that for the other pressure bumps the role of the neon must be smaller, which is consistent with Figure 9.

7.1.3 Distant pressure bumps at 58 m and 151 m

For both the 58 m and the 151 m pressure bumps, $\varepsilon_{BCM}(z)$ is far below unity, i.e. this hard limit does not provide any constraint. On the other hand, these positions are not affected by the annual neon injection, so the assumption that hydrogen is emitted predominantly is justified.

Only Vasco results are available for the distant pressure bump locations. The accuracy of these can be estimated by comparing Vasco calculations with the more detailed MolFlow+ simulation results for the nearby bumps. Figure 8 shows that R_{BG} values obtained from Vasco are rather consistent with MolFlow+ predictions when $\alpha \approx 5 \times 10^{-3}$ is assumed for the latter; for the 19 m pressure bumps Vasco gives an only 8% higher R_{BG} while for the 22 m position it is 23% lower. This good agreement seen for the nearby bumps provides confidence in the pressure profiles produced by Vasco for the distant bumps.

Since the maximum pressure of the Vasco-calculated profile is scaled to the local gauge reading, an uncertainty arises from how well the measured pressure represents the maximum at the beam line. At both distant locations two nearby vacuum gauges are available. One is close to the NEG cartridge used for the gas injection while the other is about 25 cm away on the other side of a sector valve. Both gauges are on chimneys, recessed from the beam line. In the absence of the pressure bump they report very consistent values. When the gas is injected the pressure measurements differ significantly. At both locations the gauge next to the NEG is used and can be assumed to provide an upper estimate for the pressure at the beam line. At 58 m the neighbouring gauge remains reasonably consistent with the steep edge of the pressure profile but for the 151 m bump, shown in Figure 7(b), the pressures reported by the two adjacent gauges differ by more than an order of magnitude. This effect is systematically seen for all fills and both beams at the 151 m location.

In the extreme case of using VGPB938 as the absolute pressure reference at 151 m, R_{BG} would increase by an order of magnitude. The VGPB935 gauge, however, is assumed to provide a better estimate of the pressure at the beam line, although it could slightly overestimate R_{BG}: the MolFlow+ results shown in Figure 4 suggest that the gauge on the same chimney as the NEG cartridge overestimates the beam-line pressure by 30–150%, depending on α. The equipment configuration at the nearby locations, however, is very different from that at 151 m. In particular all chimneys have a NEG coating, which is not the case at 151 m. Thus the relevant difference should be that seen for the smallest α-values, i.e. ~50% at most.

It is evident from Figure 7(b) that such a 50% correction is not nearly sufficient to establish agreement with the VGPB938 pressure measurement. The origin of this discrepancy is most likely in the local configuration of the vacuum equipment: the two gauges are located on different chimneys and the one housing VGPB938 has a much smaller diameter than the beam pipe and therefore lower conductance. Thus the pressure drop along the chimney is larger than along the beam line. This is also consistent with the difference appearing only when the gas is injected. This explanation implies that the pressure measured by VGPB938 is not relevant, i.e. no additional uncertainty is derived from it.

An alternative explanation for the discrepancy between the two gauges is that it is due to an overestimate of the profile width: if the slope is underestimated on the side of the cold magnet, the pressure at VGPB938 is overestimated. As the pressure scale in the plot is logarithmic, a steeper slope, passing through the two measurements, would reduce R_{BG} by only ~30%.

Both uncertainties, discussed above, are asymmetric and tend in the direction of R_{BG} being overestimated. Although the discrepancy between the two neighbouring gauges is significantly smaller at the 58 m location, it seems prudent to assign the same uncertainties there as at 151 m.

Table 7 summarises the measurement-related uncertainties discussed above and in Section 7.1.2. For the nearby pressure bumps the unknown neon contribution dominates all other effects. For the distant bumps it is not obvious how the uncertainties should be combined. The gauge accuracy can be assumed to represent a Gaussian uncertainty distribution, centred at the measured value. The asymmetric uncertainties, however, indicate the possible bias by which the amount of gas might be overestimated. All these uncertainty components are independent. Due to their different natures it appears justified to add the upper and lower

Table 7: Summary of uncertainties affecting the determined values of $\varepsilon_{\mathrm{BCM}}(z)$ and $\varepsilon_{\mathrm{JET}}(z)$. The first two contributions apply also to the $\omega(z_i)$ values discussed on Section 5. The fill-to-fill variation is included in the statistical errors of Tables 3, 8 and 9. The gauge accuracy is best at 19 m where a VGI-type gauge is used. For the effective α no central value is determined; instead the uncertainty is expressed as a range of $\varepsilon_{\mathrm{BCM}}(z)$ with the lower limit corresponding to the largest realistic contribution of neon. For the nearby bumps the last two uncertainties, which are related to the bump shape, are considered to be part of the effective α uncertainty.

$|z|$-position	19 m	22 m	58 m & 151 m
Proton-H_2 cross section	5%	5%	5%
Fill-to-fill	10%	10%	10%
Gauge uncertainty	10%	30%	30%
Effective α	$0.15 - 1.0$	$0.15 - 1.0$	n.a.
Gauge to profile maximum	—	—	$0 - 50\%$
Bump shape	—	—	$0 - 30\%$

limits separately in quadrature. This yields a combined uncertainty range from -30% to 70%, which means that the analysis is slightly biased towards underestimating the BIB detection efficiency.

7.2 Uncertainties of the FLUKA simulations

Systematic uncertainties affecting the FLUKA simulations arise from the accuracy of modelling the beam-gas interactions, the geometry description, the shower transport and the signal reconstruction in the detectors. All of these are difficult to estimate and disentangle since they depend very much on the particular situation.

The formation of the BCM background trigger signature is based on a simple coincidence of two energy depositions in thin diamond sensors. The main uncertainty is in the threshold ionisation to record a hit. Previous simulation studies [11] indicate that within a reasonable range of thresholds the rate varies only by a few percent, which is negligible compared with the overall uncertainties of the shower simulations.

The jet reconstruction is approximated in the FLUKA simulations by an evaluation of local energy deposition [11]. It was shown that the energy sum depends only weakly on the volume over which the integration of deposited energy is performed. It is, however, not possible to determine the overall accuracy of this method, since it is merged with all other simulation uncertainties, which are discussed below.

Extensive comparisons [39] have indicated that the simulations agree with radiation background measurements within 20–30% when the primary source is pp collisions at the IP. It is not evident to what extent this applies to BIB simulations, where the showers extend over a much larger distance and have quite different characteristics.

The BCM records BIB very close to the beam pipe, where the particle fluences originate mainly from interactions in the beam-pipe material and other accelerator elements. Thus it can be assumed that the dominant uncertainty arises from the accuracy with which the beam line is described in the simulation models. Secondary particle yields and angular distributions of the primary beam-gas interaction are another significant source of uncertainty for the BCM rates. For the nearby pressure bumps the uncertainties evaluated for pp collisions at the IP should give an indication of the error margin. Based on this a 30% uncertainty is assigned to the simulated $\varepsilon_{\mathrm{BCM}}(19\,\mathrm{m})$ and $\varepsilon_{\mathrm{BCM}}(22\,\mathrm{m})$ values.

A minor asymmetric uncertainty, affecting the nearby bumps, arises from the difference of the p-H and p-Ne interactions. The latter produce about 15% more BCM background triggers. The simulations, assuming only p-H collisions, might underestimate the BCM background rate by up to 15%, depending on the amount of neon.

For the two distant pressure bumps the geometry traversed before reaching the BCM is more complicated, and this must be reflected as a larger uncertainty. The simulated fake jet rates depend on the yield of high-energy muons in the very forward direction, which is a minor part of the entire event topology. The muon transport, however, is almost insensitive to small differences in material descriptions.

Previous BIB studies [11, 14] show agreement between data and simulation within a factor of two for the BCM and fake-jet rates. In those earlier studies, as in the present one, the dominant uncertainties were in the estimated loss rate of primary beam protons, which provides the absolute scale for the simulations. In Ref. [11] the loss rate was determined from Vasco pressure simulations for the entire LSS, in Ref. [14] from the loss rate on the primary collimators of the LHC and in the present work from the gas density in the locally introduced bumps. These normalisations are totally independent while the Fluka simulations are very similar in all three cases. The fact that all three studies find agreement within a factor of about two indicates that the uncertainties of the Fluka simulations, themselves, should be lower. Although this provides no rigorous argument to quantify the uncertainty associated with the Fluka simulations alone, it suggests that a factor of 1.5 is reasonable.

8 Comparison with simulations

8.1 BIB detection efficiencies

The comparison of the simulated efficiencies with the averages of the values given in Tables 5 and 6 is the primary objective of this study. The localised pressure bumps provide much more detailed benchmarking of the simulations than could be obtained in Ref. [11]. These comparisons are shown in Tables 8 and 9 for BCM and fake-jet backgrounds, respectively. In order to avoid the E_T-range where the jet trigger is not yet fully efficient, the jet rates are compared for $E_T >20$ GeV. Therefore the values given in Table 9 are considerably lower than the averages over the individual fills shown in Table 6.

The simulations predict that the BCM detects about 40% of p-H collisions taking place at 19 m and 22 m. As discussed before, a significant neon contribution would increase the simulated efficiency by up to 15%. This increase, however, is anti-correlated with the effect neon has on the measurement, in which it pushes the efficiency towards the lower limit of the range given in Table 8. Assuming $\alpha = 5 \times 10^{-3}$ for H_2, the amount of neon needed to bring the measurement and simulation into consistency can be estimated: for the beam-1 pressure bump at 19 m about 1.2×10^{13} neon atoms, which is ~25% of the amount extracted in the laboratory tests, in the beam vacuum would result in a measured $\varepsilon_{BCM}(19\,\text{m}) \approx 0.5$. With that neon density about 90% of the beam-gas interactions would be p-Ne collisions, i.e. the simulated $\varepsilon_{BCM}(19\,\text{m})$ would rise by almost 15% with respect to Table 8, reaching the same ~0.5 as the measurement. For the other pressure bumps the amount of neon needed to lower the measured $\varepsilon_{BCM}(z)$ to ~0.5 would be less – around 5×10^{12} atoms. Even with this amount, p-Ne collisions would dominate over p-H. It is, actually, very difficult to conceive that the measurement and simulations could be consistent if hydrogen is the only gas contributing, while the two-gas model presented in Section 6.4 could establish consistency.

Table 8: BCM efficiency to detect a beam-gas event in the various pressure bump locations. The results from all fills are averaged and compared with the simulations, in which the two beams are assumed identical. As explained in the text, exact values of $\varepsilon_{\mathrm{BCM}}(19\,\mathrm{m})$ and $\varepsilon_{\mathrm{BCM}}(22\,\mathrm{m})$ cannot be determined due to the possible but not quantifiable contribution of neon. The lower limit of the given range corresponds to the maximum reasonable neon contribution, as discussed in Section 7.1.2. The fill-to-fill variation, derived from the per-fill data given in Table 5, is included in the errors. The systematic effects discussed in Section 7.1.3 are not included for the distant bumps. The simulations assume p-H collisions and for the 19 m and 22 m locations a gas density profile corresponding to $\alpha = 5 \times 10^{-3}$ is assumed. The uncertainties on the simulations are statistical only.

	Measured		Simulated
	Beam-1	Beam-2	Beams 1 or 2
$\varepsilon_{\mathrm{BCM}}(19\,\mathrm{m})$	$0.15 - 1.0$	$0.15 - 1.0$	0.424 ± 0.006
$\varepsilon_{\mathrm{BCM}}(22\,\mathrm{m})$	$0.15 - 1.0$	$0.15 - 1.0$	0.432 ± 0.006
$\varepsilon_{\mathrm{BCM}}(58\,\mathrm{m})$	0.029 ± 0.001	0.043 ± 0.005	0.0284 ± 0.0014
$\varepsilon_{\mathrm{BCM}}(151\,\mathrm{m})$	0.0071 ± 0.0003	0.0056 ± 0.0008	0.0075 ± 0.0002

Table 9: Efficiency to detect fake jets with $E_{\mathrm{T}} > 20\,\mathrm{GeV}$ from beam-gas events in the various pressure bump locations. The results from all fills are averaged and compared with simulation in which the two beams are assumed identical. The upper table shows results for the full $|\eta|$-range considered in this study. The lower table compares the data and simulations for $\eta| < 1.5$, which roughly corresponds to the barrel calorimeters. This reduced range is consistent with earlier work where similar comparisons are made [11, 14]. The fill-to-fill variation, derived from the per-fill data given in Table 6, is included in the errors. The systematic effects discussed in Section 7.1.3 are not included. The uncertainties on the simulations are statistical only.

	Measured ($|\eta| < 3.2$)		Simulated ($|\eta| < 3.2$)
	Beam-1	Beam-2	Beams 1 or 2
$\varepsilon_{\mathrm{JET}}(58\,\mathrm{m})$	$(1.3 \pm 0.2) \times 10^{-5}$	$(3.1 \pm 0.2) \times 10^{-5}$	$(1.5 \pm 0.1) \times 10^{-5}$
$\varepsilon_{\mathrm{JET}}(151\,\mathrm{m})$	$(8.7 \pm 0.5) \times 10^{-5}$	$(8.3 \pm 0.4) \times 10^{-5}$	$(6.9 \pm 0.1) \times 10^{-5}$

	Measured ($|\eta| < 1.5$)		Simulated ($|\eta| < 1.5$)
	Beam-1	Beam-2	Beams 1 or 2
$\varepsilon_{\mathrm{JET}}(58\,\mathrm{m})$	$(2.5 \pm 0.2) \times 10^{-6}$	$(8.7 \pm 0.1) \times 10^{-6}$	$(5.4 \pm 0.6) \times 10^{-6}$
$\varepsilon_{\mathrm{JET}}(151\,\mathrm{m})$	$(3.3 \pm 0.4) \times 10^{-5}$	$(3.3 \pm 0.3) \times 10^{-5}$	$(2.25 \pm 0.08) \times 10^{-5}$

For the 151 m bump the simulations agree almost perfectly with the data for the BCM backgrounds, and underestimate the fake jets by about 20%. For the beam-1 bumps at 58 m the simulations agree rather well with the BCM backgrounds and the fake-jet measurements, especially if the latter are considered over the entire $|\eta|$-range. For both, BCM and fake-jet backgrounds, the difference between data and simulation exceeds significantly the statistical uncertainties for the 58 m bump in beam-2. This is consistent with Table 3, which is based on pure data and reveals a substantial difference between beam-1 and beam-2 for the 58 m bump: the BCM background per unit measured pressure is 50% higher for beam-2 than beam-1. For fake jets the difference seems even larger – about a factor of two. Since the pedestal background and pressure are subtracted prior to forming these ratios, an additional source, not related to the pressure bump, can be excluded. This could imply that either the gauge efficiency on the beam-2 side was lower or the
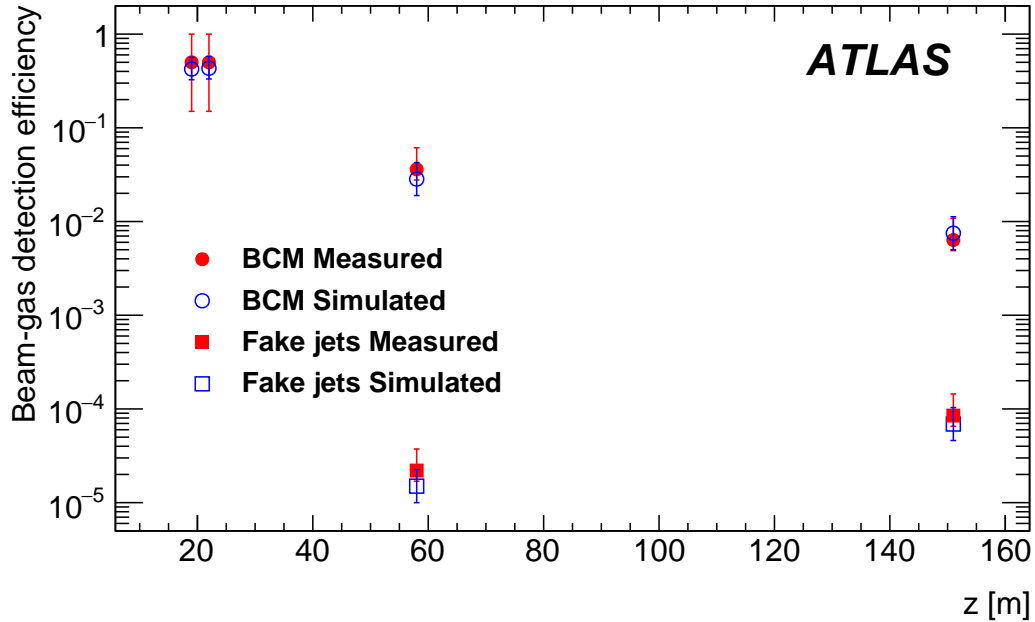
Figure 10: Detection efficiency of beam-gas events as a function of z. The measurements correspond to the averages of both beams in Tables 8 and 9. The error bars are dominated by the estimated systematic uncertainties, as discussed in Section 7. The average of the measured value for the two nearby points is set to 0.5, which corresponds to assuming a significant neon contribution, as discussed in the text. The error bars display the range indicated in Table 8. The error bars on the measurements at the two distant points are dominated by the 50% uncertainty on how well the pressure measured by a gauge reflects the amount of gas in the bump region.

bump width at 58 m was wider than predicted by the VASCO calculations.[6]

Figure 10 shows $\varepsilon_{BCM}(z)$ and $\varepsilon_{JET}(z)$ as a function of z. The error bars in the plot include the estimated systematic uncertainties, as discussed in Section 7. For the two nearby points it is assumed that neon plays a significant role in lowering $\varepsilon_{BCM}(z)$ to ~ 0.5, as discussed above. This summary plot illustrates the opposite trends of the two BIB observables as a function of z: the $\varepsilon_{BCM}(z)$ decreases with distance from the IP while $\varepsilon_{JET}(z)$ increases. It is worth emphasising that the data shown in Figure 10 span over four orders of magnitude. Even though the uncertainty estimates are large, they play no significant role in the principal outcome of this study, which is a demonstration of the strong z-dependence of the beam-gas detection efficiency with opposite trends for the BCM and fake-jet backgrounds.

A comparison in the reduced $|\eta|$-range is presented in Table 9 in order to maintain consistency with earlier work [11, 14]. This ensures that the trigger is fully efficient over the η-range considered. Another reason for the restriction is that the simulations assume that all fake jets are produced by high-energy muons. While this assumption is certainly justified for the barrel calorimeters, the possibility of hadronic showers, initiated in the beam-pipe walls and reconstructed as jets in the endcaps, cannot be excluded [11]. A comparison of the results for the two $|\eta|$-ranges in Table 9, however, reveals that considering only central rapidities leads to a slightly larger reduction of the simulated than the observed fake-jet rates. This confirms that radiative

---

[6] A comparison of the ratios between the two neighbouring gauges at 58 m reveals that the preferred gauge was giving up to 40% lower readings on the beam-2 side, especially in fills 5331 and 6239. This could explain the higher ε-values seen in Tables 8 and 9 as well as the larger fill-to-fill variation seen in Table 5.

energy losses of high-energy muons are, by far, the dominant origin of the fake-jet background even in the endcap calorimeters, but it also suggests that either the efficiency drop of the jet trigger is significant in the endcap region or the simulations underestimate the radial spread of high-energy muons.

When the BIB detection efficiencies reported in Tables 8 and 9 are compared with those for BIB resulting from beam-halo losses on the TCT [14], it is seen that they are significantly higher, especially for the BCM. This indicates that the higher BCM/Jet ratio reported in Table 4, compared to Ref. [14], is due to more secondaries from beam-gas events staying inside the beam-pipe aperture and reaching the BCM. If protons interact in the TCT jaws, a larger fraction of the produced particles is absorbed locally or in the accelerator structures between the collision point and the IP. Because fake jets are the type of BIB that can affect some physics searches, this large difference is potentially relevant: it indicates that not only the z-position where the proton is lost matters, but also the material or accelerator element on which it is lost. Thus a monitoring of BIB with the BCM alone might severely underestimate the fake-jet rates if beam halo losses on the TCT become more important with evolving LHC beam optics and collimator settings.

8.2 Jet distributions

Based on earlier simulations [12], the ϕ-distribution of the muon background originating from $|z| < 60$ m is expected to exhibit maxima in both the horizontal and vertical planes, while muons from farther away are predominantly in the plane of the LHC ring. This azimuthal distribution should be reflected in the fake-jet rates. Fake-jet data collected in the absence of a pressure bump, however, show pronounced maxima only at $\phi = 0$ and $\phi = \pi$ and only very minor humps at $\phi = \pm\pi/2$ [11].

With the clear excess of fake jets observed from both, the 58 m and the 151 m locations in the pressure bump data, it is possible to verify whether the azimuthal jet distribution depends on the $|z|$-location of the beam-gas event. In particular, it is possible to investigate how the azimuthal BIB distribution is affected by the D1 dipole, which is situated between these two bump locations.

In data the additional fake jets due to the pressure bumps are merged with the distribution from elsewhere around the ring. Especially for the 58 m location this pedestal is large dilutes the ϕ-distribution. As it is impossible to determine the $|z|$-origin of an individual fake jet seen in data, the pedestal can only be subtracted on average. For this the jet counts per azimuthal bin, collected in periods (see, e.g. Figure 6) with a normal pressure distribution ($N_{\text{Base}}(\Delta\phi)$), are subtracted from those during the gas injection ($N_{\text{Bump}}(\Delta\phi)$), after weighting with the ratio of wall-clock times ($t_{\text{Bump}}/t_{\text{Base}}$) over which the two data sets are collected:

$$N_z(\Delta\phi) = N_{\text{Bump}}(\Delta\phi) - \frac{t_{\text{Bump}}}{t_{\text{Base}}} N_{\text{Base}}(\Delta\phi). \tag{10}$$

The resulting $N_z(\Delta\phi)$ is the estimated additional number of counts due to the pressure bump at z. Table 6 shows that the fake-jet rate per unit measured pressure varies significantly from fill to fill and between the two beams, especially for the 58 m location. Including this variation would inflate the uncertainties and render a comparison of the ϕ-distributions less conclusive. In order to limit the comparison to the shape only, the different fills are made comparable by normalising all distributions to unity before averaging $N_z(\Delta\phi)$ over the fills. Due to this normalisation the E_{T}-cut becomes irrelevant so, unlike in Table 9, all jets with $E_{\text{T}} > 12$ GeV have been retained in order to maximise the sizes of the samples.[7] Even with the relaxed E_{T}-cut, the data suffer from a low count rate; after subtracting the estimated pedestal, only slightly more

---

[7] Raising the cut threshold to 20 GeV has no effect on the shapes of the distribution.
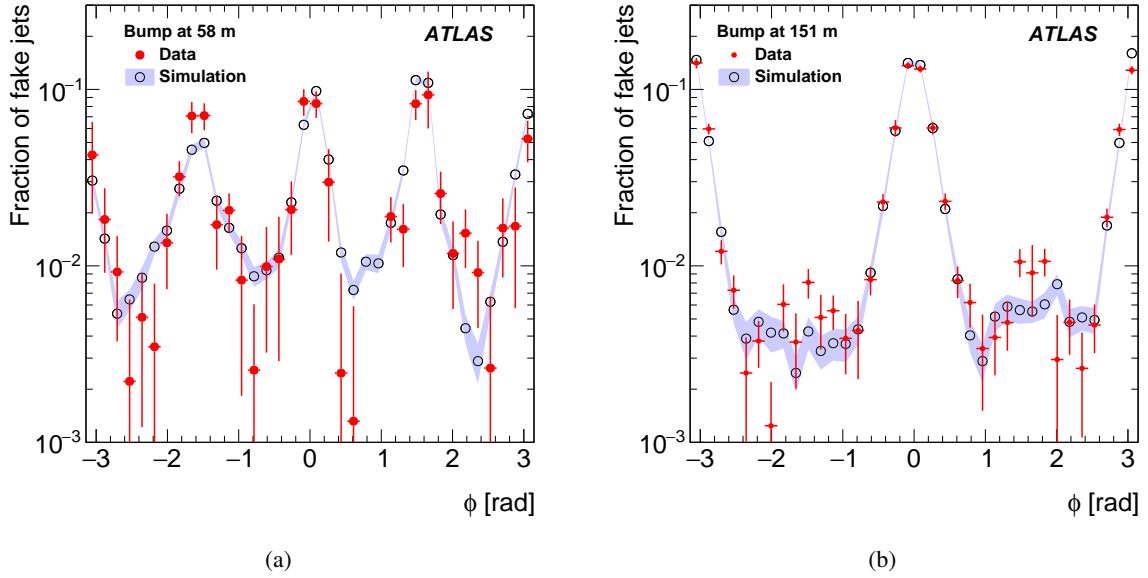
Figure 11: Comparison of azimuthal distributions of fake jets seen in data and predicted by simulations for the (a) 58 m and (b) 151 m pressure bumps. All distributions are normalised to unity, thus only the shapes are compared, not the absolute rates. The data of both beams are added.

than 1100 fake jets remain for the 58 m pressure bump. These are distributed among the 36 ϕ-bins in the plot, and most entries fall into the peaks. Thus the minima have just a few counts per bin. For the 151 m pressure bump the count rate is higher: about 5000 fake jets remain after pedestal subtraction.

The count rate in the FLUKA simulations has no pedestal but is limited by the number of beam-gas events available from the LHC simulations. The number of counts is of similar magnitude to that in the data: slightly more than 3000 jets from both the 58 m and the 151 m locations. For the 151 m position the events are selected according to the pressure bump profile. At 58 m, where the probability to obtain a jet is lower, all beam-gas events with a flat distribution in the range 53–63 m had to be used in order to reach this number of fake jets. The probability for a high-energy muon to generate a fake jet when traversing the ATLAS calorimeters is at the percent level. Thus the number of simulated events could be doubled by using twice each muon produced by the LHC simulations. This introduced a minor correlation, i.e. about 1% of the fake jets originated from the same muon and, thereby, fall into the same ϕ-bin.

The comparisons, shown in Figure 11, confirm that the data and simulations agree on the expected feature: the ϕ-distribution of fake jets from 58 m exhibits four peaks while those from 151 m are predominantly in the plane of the accelerator. The agreement on the shape of the azimuthal distributions is remarkably good for both locations. The only significant elements between 58 m and the IP, which are not ϕ-symmetric, are the quadrupoles of the inner triplet. Between 58 m and 151 m the D1 dipole introduces an additional breaking of ϕ-symmetry. Thus Figure 11 confirms the assumption that the four-peak structure arises from the bending of muon trajectories in the quadrupoles, while the more significant peaks in the accelerator plane are caused by the dipole fields.

Figure 12 shows the pseudorapidity distributions of the fake jets. The measured distributions are rather similar for both distant pressure bump locations. There are slightly more fake jets in the downstream half, i.e. positive z. The FLUKA simulations reproduce these shapes reasonably well, although there are some
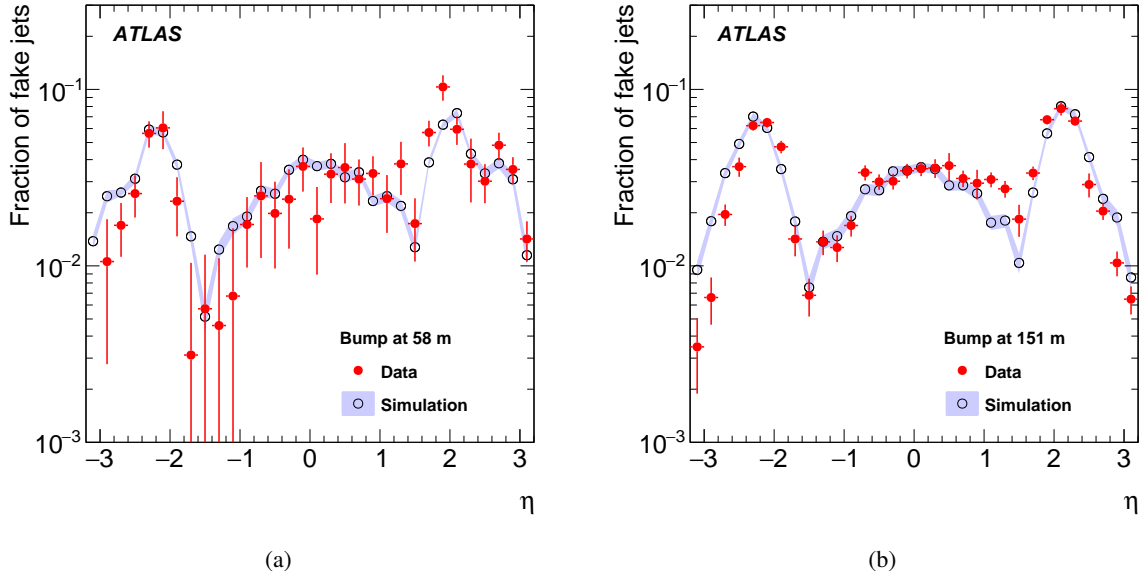
Figure 12: Comparison of pseudorapidity distribution of fake jets seen in data and predicted by simulations for the (a) 58 m and (b) 151 m pressure bumps. The data of both beams are added after inverting z for beam-1 unpaired bunches, i.e. the beam direction is always from negative to positive η. All distributions are normalised to unity, thus only the shapes are compared, not the absolute rates.

differences, especially at high $|\eta|$. These are, at least qualitatively, consistent with the drop of the jet trigger efficiency at $|\eta| > 2.8$, which is not accounted for in the simulations.

The distributions from both beams were inspected separately and found to agree within statistical uncertainties. Therefore the contributions of both beams are added together in Figures 11 and 12, in the latter case after inverting the beam-1 direction.

9 Backgrounds excess following a pressure test

In the normal physics fills, following the pressure test in fill 7212, unusually high beam-1 backgrounds were recorded by the BCM. In the first fill after the test, the background jumped to about 10 times the normal level and then gradually decreased over the course of the fill. In subsequent fills the same was observed, although the magnitude of the initial jump was reduced from fill to fill. It took several normal physics fills for the beam-1 start-of-collision background levels to recover to their pre-test levels. This is illustrated in Figure 13(a) where the start-of-collision backgrounds in five fills before the pressure test are compared with those in 13 fills following the test. Only fills starting with high luminosity are included in the plot, and the backgrounds are averaged over the first 30 minutes of data-taking, provided the average number of collisions per bunch crossing was higher than 45. This requirement was imposed in order to prevent start-of-fill emittance scans [40] from biasing the results, since the background jump is obviously luminosity-related. The background increase seems to affect only beam-1; no sign of a similar increase is seen for BIB from beam-2. As shown in Figure 13(b), at the same time the vacuum gauges at the 19 m and 22 m positions, where the pressure bumps had been introduced, showed no anomalies. The reason for this
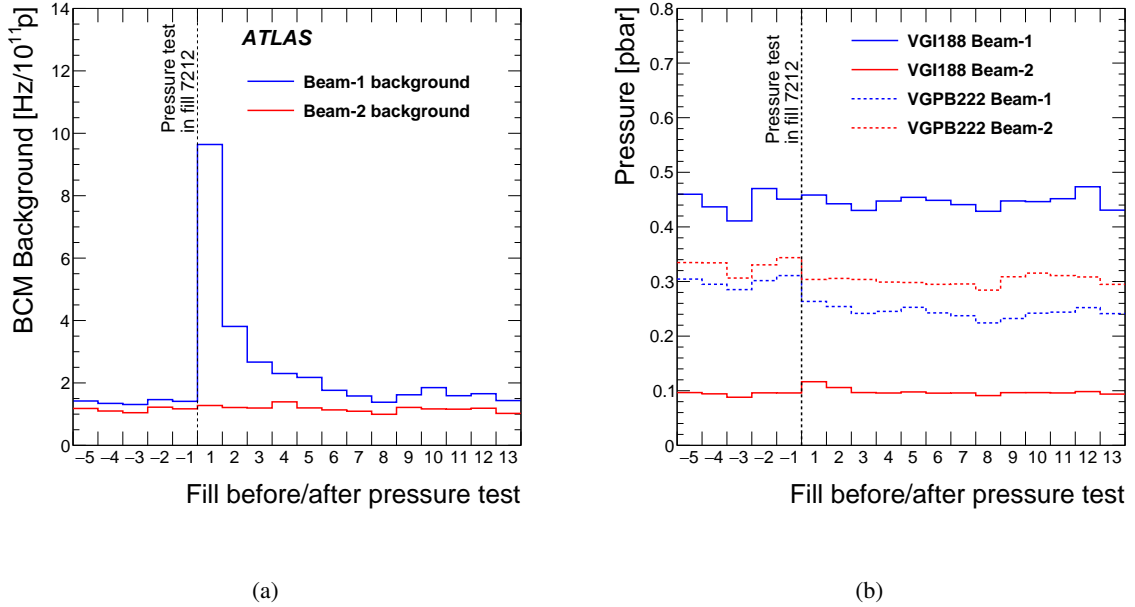
Figure 13: (a) BCM backgrounds and (b) residual pressures for the two beams observed in normal physics fills just before the pressure test and in several fills thereafter. Each bin represents the average over the first 30 minutes of data-taking at high luminosity. The dashed vertical line indicates the pressure test, which itself is excluded from the plot.

excess is not entirely clear. Possibly some of the injected gas had condensed on the BS and was gradually desorbed by the particle debris hitting the BS during high-luminosity operation.

Although the increase of the BCM background trigger rate for beam-1 was an order of magnitude, it had no impact on the operation or data quality of ATLAS. This can be taken as an indication of the margin that ATLAS at least has with respect to BIB from nearby beam-gas collisions, before data-taking efficiency or quality of physics data start to be affected.

10 Conclusions

Several dedicated pressure bump tests were undertaken in five different fills during LHC Run 2 in order to determine the sensitivity of the ATLAS beam-induced background (BIB) monitoring system to beam-gas events at different distances from the interaction point (IP). In these tests individual non-evaporative getter (NEG) cartridges in the vicinity of the ATLAS experimental area were heated in order to reverse the pumping process. In the bumps the gas density was up to four orders of magnitude higher than elsewhere.

A very good correlation between the pressure measured at the bump location and the BIB rates seen in ATLAS is observed, i.e. the BIB rate can be fitted with a linear combination of a constant term and the local pressure changes, weighted with z-dependent proportionality constants.

The ratio of BIB from the different bump locations, seen by the beam conditions monitor (BCM) and as fake-jet backgrounds in the calorimeters, is evaluated. It confirms previous simulation studies, which predict that beam-gas events very close to the detector do not produce fake jets, while the BCM has high sensitivity to BIB originating from that region. With increasing distance from the IP the sensitivity of

the BCM drops while fake jets become more likely. At $|z| = 58$ m the BCM/jet BIB ratio is ~800 and at $|z| = 151$ m it is only ~45. This latter value is much larger than the ratio of about six, which has been measured for BIB from proton halo impacting on the tertiary collimators, only a few metres closer to the IP. These large differences imply that BCM and fake-jet backgrounds are very weakly correlated and BIB monitoring by the BCM alone does not provide a reliable measure of the fake-jet rate.

In order to derive absolute background detection efficiencies for the different z-locations, the amount of gas traversed by the beam was evaluated from the calculated pressure profile of each bump. Although the calculations were adjusted to the measured pressure, they are subject to significant uncertainties, in particular the pumping efficiency of the NEG-coating in the room-temperature sections of the beam pipe. With a typical NEG efficiency of $\alpha = 5 \times 10^{-3}$ the results for the two nearby pressure bumps indicate that more beam-gas events are detected than are produced. A possible explanation is that upon heating the NEG cartridge releases some neon in addition to the expected hydrogen. The neon could be a residue from filling the beam pipe with an ultra-pure noble gas to atmospheric pressure during access to the experiment. Neon, which is not pumped by the NEG coating ($\alpha = 0$), would have a wider distribution and longer residence time in the beam pipe than hydrogen. It also has an about ten times higher cross section for proton scattering.

Even though systematic uncertainties are estimated to be of the order of a factor of two, they are rather minor compared to the differences of the observed efficiencies, which extend over several orders of magnitude, depending on the z-location. The $\varepsilon_{BCM}(z)$ values range from just below unity for pressure bumps at 19 m and 22 m to ~3% at 58 m and ~0.6% at 151 m. No fake-jet backgrounds are detected from the two nearby bump positions. For the 58 m and 151 m bumps the $\varepsilon_{JET}(z)$ values, for $E_T > 12$ GeV, are ~ 4×10^{-5} and ~ 1.4×10^{-4}, respectively.

For the nearby pressure bumps the FLUKA simulations agree with the data at $\varepsilon_{BCM}(z) \sim 0.5$, but only if neon plays a significant role. The simulation results for the two distant bumps are in good agreement with the measurements. The latter are based on pressure profile calculations that are consistent with $\alpha \approx 5 \times 10^{-3}$. In these regions no neon filling is applied, so the assumption of hydrogen dominance should be valid.

The shapes of the fake-jet distributions in the azimuthal plane and as a function of pseudorapidity have been compared with simulations, and good agreement is found. The data show, in particular, that the azimuthal distribution of jets from the 58 m position has four about equally high maxima at $n\frac{\pi}{2}$, while jets from 151 m are predominantly in the plane of the accelerator ring, i.e. their distribution peaks at $n\pi$.

All tests were performed parasitically during normal physics data taking. No adverse effects for the performance of ATLAS or the LHC were seen. Even the unexplained contamination of the beam vacuum, observed after the last test, had no impact on the operation of the accelerator or the experiment.

This study completes a set of dedicated measurements and simulations that comprise also Refs. [11, 14]. Together these cover the dominant sources of BIB in the ATLAS detector and show that the sources of these backgrounds are well understood and simulations can reproduce them within a factor of about two. These results, and the successful benchmarking of the simulation methods, provide important information for the study and optimisation of future accelerator configurations and BIB mitigation methods.

Acknowledgements

References

[1] L. Evans and P. Bryant, *LHC Machine*, JINST **3** (2008) S08001.

[2] ATLAS Collaboration, *Search for light long-lived neutral particles that decay to collimated pairs of leptons or light hadrons in pp collisions at $\sqrt{s} = 13$ TeV with the ATLAS detector*, JHEP **06** (2023) 153, arXiv: 2206.12181 [hep-ex].

[3] ATLAS Collaboration, *Search for neutral long-lived particles in pp collisions at $\sqrt{s} = 13$ TeV that decay into displaced hadronic jets in the ATLAS calorimeter*, JHEP **06** (2022) 005, arXiv: 2203.01009 [hep-ex].

[4] ATLAS Collaboration, *Search for events with a pair of displaced vertices from long-lived neutral particles decaying into hadronic jets in the ATLAS muon spectrometer in pp collisions at $\sqrt{s} = 13$ TeV*, Phys. Rev. D **106** (2022) 032005, arXiv: 2203.00587 [hep-ex].

[5] R. Bruce et al., *Simulations and measurements of beam loss patterns at the CERN Large Hadron Collider*, Phys. Rev. ST Accel. Beams **17** (2014) 081004, arXiv: 1409.3123 [physisc.acc-ph].

[6] A. I. Drozhdin, M. Huhtinen and N. V. Mokhov, *Accelerator related background in the CMS detector at LHC*, Nucl. Instr. and Meth., A **381** (1996) 531.

[7] A. I. Drozhdin, N. V. Mokhov and S. I. Striganov, *Beam Losses and Background Loads on Collider Detectors due to Beam-Gas Interactions in the LHC*, FERMILAB-CONF-09-172-APC, 2009, URL: http://lss.fnal.gov/archive/2009/conf/fermilab-conf-09-172-apc.pdf.

[8] R. Bruce et al., *Sources of machine-induced background in the ATLAS and CMS detectors at the CERN Large Hadron Collider*, Nucl. Instrum. Meth. A **729** (2013) 825.

[9] ATLAS Collaboration, *The ATLAS Experiment at the CERN Large Hadron Collider*, JINST **3** (2008) S08003.

[10] V. Cindro et al., *The ATLAS beam conditions monitor*, JINST **3** (2008) P02004.

[11] ATLAS Collaboration, *Comparison between simulated and observed LHC beam backgrounds in the ATLAS experiment at E_{beam} = 4 TeV*, JINST **13** (2018) P12006, arXiv: 1810.04450 [hep-ex].

[12] ATLAS Collaboration, *Characterisation and mitigation of beam-induced backgrounds observed in the ATLAS detector during the 2011 proton–proton run*, JINST **8** (2013) P07004, arXiv: 1303.0223 [hep-ex].

[13] ATLAS Collaboration, *Beam-induced and cosmic-ray backgrounds observed in the ATLAS detector during the LHC 2012 proton–proton running period*, JINST **11** (2016) P05013, arXiv: 1603.09202 [hep-ex].

[14] R. Bruce et al., *Collimation-induced experimental background studies at the CERN Large Hadron Collider*, Phys. Rev. Accel. Beams **22** (2019) 021004.

[15] P. Manini and E. Maccallini, *NEG pumps: Sorption mechanisms and applications*, 2020, arXiv: 2006.01537 [physics.ins-det].

[16] T. T. Böhlen et al., *The FLUKA Code: Developments and Challenges for High Energy and Medical Applications*, Nucl. Data Sheets **120** (2014) 211.

[17] A. Ferrari, P. R. Sala, A. Fasso and J. Ranft, *FLUKA: A multi-particle transport code*, CERN-2005-010 (2005), URL: https://cds.cern.ch/record/898301.

[18] ATLAS Collaboration, *Performance of the ATLAS trigger system in 2015*, Eur. Phys. J. C **77** (2017) 317, arXiv: 1611.09661 [hep-ex].

[19] ATLAS Collaboration, *The ATLAS Collaboration Software and Firmware*, ATL-SOFT-PUB-2021-001, 2021, URL: https://cds.cern.ch/record/2767187.

[20] ATLAS Collaboration, *The performance of the jet trigger for the ATLAS detector during 2011 data taking*, Eur. Phys. J. C **76** (2016) 526, arXiv: 1606.07759 [hep-ex].

[21] ATLAS Collaboration, *Vertex Reconstruction Performance of the ATLAS Detector at $\sqrt{s}$ = 13 TeV*, ATL-PHYS-PUB-2015-026, 2015, URL: https://cds.cern.ch/record/2037717.

[22] M. Cacciari, G. P. Salam and G. Soyez, *The anti-k_t jet clustering algorithm*, JHEP **04** (2008) 063, arXiv: 0802.1189 [hep-ph].

[23] M. Cacciari, G. P. Salam and G. Soyez, *FastJet user manual*, Eur. Phys. J. C **72** (2012) 1896, arXiv: 1111.6097 [hep-ph].

[24] ATLAS Collaboration, *Topological cell clustering in the ATLAS calorimeters and its performance in LHC Run 1*, Eur. Phys. J. C **77** (2017) 490, arXiv: 1603.02934 [hep-ex].

[25] ATLAS Collaboration, *Monitoring and data quality assessment of the ATLAS liquid argon calorimeter*, JINST **9** (2014) P07024, arXiv: 1405.3768 [hep-ex].

[26] C. Benvenuti, P. Chiggiato, F. Cicora and V. Ruzinov, *Decreasing surface outgassing by thin film getter coatings*, Vacuum **50** (1998) 57.

[27] H. Wiedemann, *Particle Accelerator Physics*, Graduate Texts in Physics, Springer, 2015, URL: https://www.springer.com/us/book/9783319183169?wt_mc=ThirdParty.SpringerLink.3.EPR653.About_eBook.

[28] G. Lanza, V. Baglin, G. Bregliozzi and P. Chiggiato,
'LHC Experimental Beam Pipe Upgrade during LS1', *Proc. 5th International Particle Accelerator Conference (IPAC'14), Dresden, Germany, June 15-20, 2014* (Dresden, Germany) 2366,
URL: http://jacow.org/ipac2014/papers/wepme044.pdf.

[29] V. Baglin, *Cryopumping and Vacuum Systems*, 2020, arXiv: 2006.01574 [ins-det].

[30] K. Jousten, 'Ultrahigh vacuum gauges', *CAS - CERN Accelerator School: Vacuum in Accelerators*,
2007 24 p, URL: https://cds.cern.ch/record/1046855.

[31] *"SAES Getters"*, https://accelconf.web.cern.ch/p01/EXHIBIT/SAES.pdf, URL:
https://www.saesgetters.com/wp-content/uploads/sites/5/2024/02/Capacitorr-
Pumps-Scheda-D400_2_206x292mm_2024-2.pdf.

[32] K. Jousten et al., *A review on hot cathode ionisation gauges with focus on a suitable design for measurement accuracy and stability*, Vacuum **179** (2020) 109545.

[33] A. Rossi,
VASCO (VAcuum Stability COde): multi-gas code to calculate gas density profile in a UHV system,
LHC-Project-Note 341, CERN, 2004, URL: https://cds.cern.ch/record/728512.

[34] R. Kersevan and M. Ady, *Recent developments of Monte-Carlo codes Molflow+ and Synrad+*,
(2019) TUPMP037. 4 p, URL: http://cds.cern.ch/record/2694236.

[35] V. Baglin et al., 'The LHC Experimental Beam Pipe Neon Venting, Pumping and Conditioning',
Proc. 2nd Int. Particle Accelerator Conf. (IPAC'11) (San Sebastian, Spain),
JACoW Publishing, 2011 1557,
URL: https://accelconf.web.cern.ch/IPAC2011/papers/tups017.pdf.

[36] G. Bregliozzi, 'Neon Venting of Activated NEG Beam Pipes in the CERN LHC Long Straight Sections without Losing Vacuum Performance', *Particle Accelerator Conference (PAC 09)*, 2010,
URL: https://accelconf.web.cern.ch/PAC2009/papers/mo6rfp006.pdf.

[37] A. Galloro, *Measurements of Neon desorption from a SAES Getter D400 Capacitorr NEG cartridge*,
tech. rep., 2021, URL: https://edms.cern.ch/document/2683915/2.

[38] R. L. Workman et al., *Review of Particle Physics*, PTEP **2022** (2022) 083C01.

[39] ATLAS Collaboration, *The ATLAS Experiment at the CERN Large Hadron Collider: A Description of the Detector Configuration for Run 3*, JINST **19** (2024) P05063,
arXiv: 2305.16623 [physics.ins-det].

[40] O. Karacheban and Y. C. Cekmecelioglu,
Emittance Scans for CMS Luminosity Calibration in run 2, PoS **EPS-HEP2019** (2020) 193.

[41] ATLAS Collaboration, *ATLAS Computing Acknowledgements*, ATL-SOFT-PUB-2023-001, 2023,
URL: https://cds.cern.ch/record/2869272.

The ATLAS Collaboration

G. Aad[104], E. Aakvaag[17], B. Abbott[123], S. Abdelhameed[119a], K. Abeling[56], N.J. Abicht[50], S.H. Abidi[30], M. Aboelela[45], A. Aboulhorma[36e], H. Abramowicz[154], H. Abreu[153], Y. Abulaiti[120], B.S. Acharya[70a,70b,l], A. Ackermann[64a], C. Adam Bourdarios[4], L. Adamczyk[87a], S.V. Addepalli[27], M.J. Addison[103], J. Adelman[118], A. Adiguzel[22c], M. Ady[37], T. Adye[137], A.A. Affolder[139], Y. Afik[40], M.N. Agaras[13], J. Agarwala[74a,74b], A. Aggarwal[102], C. Agheorghiesei[28c], F. Ahmadov[39,y], W.S. Ahmed[106], S. Ahuja[97], X. Ai[63e], G. Aielli[77a,77b], A. Aikot[166], M. Ait Tamlihat[36e], B. Aitbenchikh[36a], M. Akbiyik[102], T.P.A. Åkesson[100], A.V. Akimov[38], D. Akiyama[171], N.N. Akolkar[25], S. Aktas[22a], K. Al Khoury[42], G.L. Alberghi[24b], J. Albert[168], P. Albicocco[54], G.L. Albouy[61], S. Alderweireldt[53], Z.L. Alegria[124], M. Aleksa[37], I.N. Aleksandrov[39], C. Alexa[28b], T. Alexopoulos[10], F. Alfonsi[24b], M. Algren[57], M. Alhroob[170], B. Ali[135], H.M.J. Ali[93], S. Ali[32], S.W. Alibocus[94], M. Aliev[34c], G. Alimonti[72a], W. Alkakhi[56], C. Allaire[67], B.M.M. Allbrooke[149], J.F. Allen[53], C.A. Allendes Flores[140f], P.P. Allport[21], A. Aloisio[73a,73b], F. Alonso[92], C. Alpigiani[141], Z.M.K. Alsolami[93], M. Alvarez Estevez[101], A. Alvarez Fernandez[102], M. Alves Cardoso[57], M.G. Alviggi[73a,73b], M. Aly[103], Y. Amaral Coutinho[84b], A. Ambler[106], C. Amelung[37], M. Amerl[103], C.G. Ames[111], D. Amidei[108], K.J. Amirie[158], S.P. Amor Dos Santos[133a], K.R. Amos[166], S. An[85], V. Ananiev[128], C. Anastopoulos[142], T. Andeen[11], J.K. Anders[37], A.C. Anderson[60], S.Y. Andrean[48a,48b], A. Andreazza[72a,72b], S. Angelidakis[9], A. Angerami[42], A.V. Anisenkov[38], A. Annovi[75a], C. Antel[57], E. Antipov[148], M. Antonelli[54], F. Anulli[76a], M. Aoki[85], T. Aoki[156], M.A. Aparo[149], L. Aperio Bella[49], C. Appelt[19], A. Apyan[27], S.J. Arbiol Val[88], C. Arcangeletti[54], A.T.H. Arce[52], E. Arena[94], J-F. Arguin[110], S. Argyropoulos[55], J.-H. Arling[49], O. Arnaez[4], H. Arnold[148], G. Artoni[76a,76b], H. Asada[113], K. Asai[121], S. Asai[156], N.A. Asbah[37], K. Assamagan[30], R. Astalos[29a], K.S.V. Astrand[100], S. Atashi[162], R.J. Atkin[34a], M. Atkinson[165], H. Atmani[36f], P.A. Atmasiddha[131], K. Augsten[135], S. Auricchio[73a,73b], A.D. Auriol[21], V.A. Austrup[103], G. Avolio[37], K. Axiotis[57], G. Azuelos[110,ad], D. Babal[29b], H. Bachacou[138], K. Bachas[155,p], A. Bachiu[35], F. Backman[48a,48b], A. Badea[40], T.M. Baer[108], P. Bagnaia[76a,76b], M. Bahmani[19], D. Bahner[55], K. Bai[126], J.T. Baines[137], L. Baines[96], O.K. Baker[175], E. Bakos[16], D. Bakshi Gupta[8], L.E. Balabram Filho[84b], V. Balakrishnan[123], R. Balasubramanian[117], E.M. Baldin[38], P. Balek[87a], E. Ballabene[24b,24a], F. Balli[138], L.M. Baltes[64a], W.K. Balunas[33], J. Balz[102], I. Bamwidhi[119b], E. Banas[88], M. Bandieramonte[132], A. Bandyopadhyay[25], S. Bansal[25], L. Barak[154], M. Barakat[49], E.L. Barberio[107], D. Barberis[58b,58a], M. Barbero[104], M.Z. Barel[117], K.N. Barends[34a], T. Barillari[112], M-S. Barisits[37], T. Barklow[146], P. Baron[125], D.A. Baron Moreno[103], A. Baroncelli[63a], A.J. Barr[129], J.D. Barr[98], F. Barreiro[101], J. Barreiro Guimarães da Costa[14], U. Barron[154], M.G. Barros Teixeira[133a], S. Barsov[38], F. Bartels[64a], R. Bartoldus[146], A.E. Barton[93], P. Bartos[29a], A. Basan[102], M. Baselga[50], A. Bassalat[67,b], M.J. Basso[159a], S. Bataju[45], R. Bate[167], R.L. Bates[60], S. Batlamous[101], B. Batool[144], M. Battaglia[139], D. Battulga[19], M. Bauce[76a,76b], M. Bauer[80], P. Bauer[25], L.T. Bazzano Hurrell[31], J.B. Beacham[52], T. Beau[130], J.Y. Beaucamp[92], P.H. Beauchemin[161], P. Bechtle[25], H.P. Beck[20,o], K. Becker[170], A.J. Beddall[83], V.A. Bednyakov[39], C.P. Bee[148], L.J. Beemster[16], T.A. Beermann[37], M. Begalli[84d], M. Begel[30], A. Behera[148], J.K. Behr[49], J.F. Beirer[37], F. Beisiegel[25], M. Belfkir[119b], G. Bella[154], L. Bellagamba[24b], A. Bellerive[35], P. Bellos[21], K. Beloborodov[38], D. Benchekroun[36a], F. Bendebba[36a], Y. Benhammou[154],

K.C. Benkendorfer [62], L. Beresford [49], M. Beretta [54], E. Bergeaas Kuutmann [164], N. Berger [4], B. Bergmann [135], J. Beringer [18a], G. Bernardi [5], C. Bernius [146], F.U. Bernlochner [25], F. Bernon [37,104], A. Berrocal Guardia [13], T. Berry [97], P. Berta [136], A. Berthold [51], S. Bethke [112], A. Betti [76a,76b], A.J. Bevan [96], N.K. Bhalla [55], S. Bhatta [148], D.S. Bhattacharya [169], P. Bhattarai [146], K.D. Bhide [55], V.S. Bhopatkar [124], R.M. Bianchi [132], G. Bianco [24b,24a], O. Biebel [111], R. Bielski [126], M. Biglietti [78a], C.S. Billingsley [45], M. Bindi [56], A. Bingul [22b], C. Bini [76a,76b], A. Biondini [94], G.A. Bird [33], M. Birman [172], M. Biros [136], S. Biryukov [149], T. Bisanz [50], E. Bisceglie [44b,44a], J.P. Biswal [137], D. Biswas [144], I. Bloch [49], A. Blue [60], U. Blumenschein [96], J. Blumenthal [102], V.S. Bobrovnikov [38], M. Boehler [55], B. Boehm [169], D. Bogavac [37], A.G. Bogdanchikov [38], C. Bohm [48a], V. Boisvert [97], P. Bokan [37], T. Bold [87a], M. Bomben [5], M. Bona [96], M. Boonekamp [138], C.D. Booth [97], A.G. Borbély [60], I.S. Bordulev [38], H.M. Borecka-Bielska [110], G. Borissov [93], D. Bortoletto [129], D. Boscherini [24b], M. Bosman [13], J.D. Bossio Sola [37], K. Bouaouda [36a], N. Bouchhar [166], L. Boudet [4], J. Boudreau [132], E.V. Bouhova-Thacker [93], D. Boumediene [41], R. Bouquet [58b,58a], A. Boveia [122], J. Boyd [37], D. Boye [30], I.R. Boyko [39], L. Bozianu [57], J. Bracinik [21], N. Brahimi [4], G. Brandt [174], O. Brandt [33], F. Braren [49], B. Brau [105], J.E. Brau [126], R. Brener [172], L. Brenner [117], R. Brenner [164], S. Bressler [172], G. Brianti [79a,79b], D. Britton [60], D. Britzger [112], I. Brock [25], G. Brooijmans [42], E.M. Brooks [159b], E. Brost [30], L.M. Brown [168], L.E. Bruce [62], R. Bruce [37], T.L. Bruckler [129], P.A. Bruckman de Renstrom [88], B. Brüers [49], A. Bruni [24b], G. Bruni [24b], M. Bruschi [24b], N. Bruscino [76a,76b], T. Buanes [17], Q. Buat [141], D. Buchin [112], A.G. Buckley [60], O. Bulekov [38], B.A. Bullard [146], S. Burdin [94], C.D. Burgard [50], A.M. Burger [37], B. Burghgrave [8], O. Burlayenko [55], J. Burleson [165], J.T.P. Burr [33], J.C. Burzynski [145], E.L. Busch [42], V. Büscher [102], P.J. Bussey [60], J.M. Butler [26], C.M. Buttar [60], J.M. Butterworth [98], W. Buttinger [137], C.J. Buxo Vazquez [109], A.R. Buzykaev [38], S. Cabrera Urbán [166], L. Cadamuro [67], D. Caforio [59], H. Cai [132], Y. Cai [14,114c], Y. Cai [114a], V.M.M. Cairo [37], O. Cakir [3a], N. Calace [37], P. Calafiura [18a], G. Calderini [130], P. Calfayan [69], G. Callea [60], L.P. Caloba [84b], D. Calvet [41], S. Calvet [41], M. Calvetti [75a,75b], R. Camacho Toro [130], S. Camarda [37], D. Camarero Munoz [27], P. Camarri [77a,77b], M.T. Camerlingo [73a,73b], D. Cameron [37], C. Camincher [168], M. Campanelli [98], A. Camplani [43], V. Canale [73a,73b], A.C. Canbay [3a], E. Canonero [97], J. Cantero [166], Y. Cao [165], F. Capocasa [27], M. Capua [44b,44a], A. Carbone [72a,72b], R. Cardarelli [77a], J.C.J. Cardenas [8], G. Carducci [44b,44a], T. Carli [37], G. Carlino [73a], J.I. Carlotto [13], B.T. Carlson [132,q], E.M. Carlson [168,159a], J. Carmignani [94], L. Carminati [72a,72b], A. Carnelli [138], M. Carnesale [76a,76b], S. Caron [116], E. Carquin [140f], S. Carrá [72a], G. Carratta [24b,24a], A.M. Carroll [126], T.M. Carter [53], M.P. Casado [13,i], M. Caspar [49], F.L. Castillo [4], L. Castillo Garcia [13], V. Castillo Gimenez [166], N.F. Castro [133a,133e], A. Catinaccio [37], J.R. Catmore [128], T. Cavaliere [4], V. Cavaliere [30], N. Cavalli [24b,24a], L.J. Caviedes Betancourt [23b], Y.C. Cekmecelioglu [49], E. Celebi [83], S. Cella [37], F. Celli [129], M.S. Centonze [71a,71b], V. Cepaitis [57], K. Cerny [125], A.S. Cerqueira [84a], A. Cerri [149], L. Cerrito [77a,77b], F. Cerutti [18a], B. Cervato [144], A. Cervelli [24b], G. Cesarini [54], S.A. Cetin [83], D. Chakraborty [118], J. Chan [18a], W.Y. Chan [156], J.D. Chapman [33], E. Chapon [138], B. Chargeishvili [152b], D.G. Charlton [21], M. Chatterjee [20], C. Chauhan [136], Y. Che [114a], S. Chekanov [6], S.V. Chekulaev [159a], G.A. Chelkov [39,a], A. Chen [108], B. Chen [154], B. Chen [168], H. Chen [114a], H. Chen [30], J. Chen [63c], J. Chen [145], M. Chen [129], S. Chen [156], S.J. Chen [114a], X. Chen [63c,138], X. Chen [15,ac], Y. Chen [63a], C.L. Cheng [173], H.C. Cheng [65a], S. Cheong [146], A. Cheplakov [39], E. Cheremushkina [49], E. Cherepanova [117], R. Cherkaoui El Moursli [36e], E. Cheu [7], K. Cheung [66], L. Chevalier [138], V. Chiarella [54], G. Chiarelli [75a], N. Chiedde [104], G. Chiodini [71a], A.S. Chisholm [21], A. Chitan [28b], M. Chitishvili [166], M.V. Chizhov [39],

K. Choi [11], Y. Chou [141], E.Y.S. Chow [116], K.L. Chu [172], M.C. Chu [65a], X. Chu [14,114c],
Z. Chubinidze [54], J. Chudoba [134], J.J. Chwastowski [88], D. Cieri [112], K.M. Ciesla [87a],
V. Cindro [95], A. Ciocio [18a], F. Cirotto [73a,73b], Z.H. Citron [172], M. Citterio [72a], D.A. Ciubotaru [28b],
A. Clark [57], P.J. Clark [53], N. Clarke Hall [98], C. Clarry [158], J.M. Clavijo Columbie [49],
S.E. Clawson [49], C. Clement [48a,48b], Y. Coadou [104], M. Cobal [70a,70c], A. Coccaro [58b],
R.F. Coelho Barrue [133a], R. Coelho Lopes De Sa [105], S. Coelli [72a], B. Cole [42], J. Collot [61],
P. Conde Muiño [133a,133g], M.P. Connell [34c], S.H. Connell [34c], E.I. Conroy [129], F. Conventi [73a,ae],
H.G. Cooke [21], A.M. Cooper-Sarkar [129], F.A. Corchia [24b,24a], A. Cordeiro Oudot Choi [130],
L.D. Corpe [41], M. Corradi [76a,76b], F. Corriveau [106,w], A. Cortes-Gonzalez [19], M.J. Costa [166],
F. Costanza [4], D. Costanzo [142], B.M. Cote [122], J. Couthures [4], G. Cowan [97], K. Cranmer [173],
D. Cremonini [24b,24a], S. Crépé-Renaudin [61], F. Crescioli [130], M. Cristinziani [144],
M. Cristoforetti [79a,79b], V. Croft [117], J.E. Crosby [124], G. Crosetti [44b,44a], A. Cueto [101], H. Cui [98],
Z. Cui [7], W.R. Cunningham [60], F. Curcio [166], J.R. Curran [53], P. Czodrowski [37],
M.M. Czurylo [37], M.J. Da Cunha Sargedas De Sousa [58b,58a], J.V. Da Fonseca Pinto [84b],
C. Da Via [103], W. Dabrowski [87a], T. Dado [50], S. Dahbi [151], T. Dai [108], D. Dal Santo [20],
C. Dallapiccola [105], M. Dam [43], G. D'amen [30], V. D'Amico [111], J. Damp [102], J.R. Dandoy [35],
D. Dannheim [37], M. Danninger [145], V. Dao [148], G. Darbo [58b], S.J. Das [30,af], F. Dattola [49],
S. D'Auria [72a,72b], A. D'avanzo [73a,73b], C. David [34a], T. Davidek [136], I. Dawson [96],
H.A. Day-hall [135], K. De [8], R. De Asmundis [73a], N. De Biase [49], S. De Castro [24b,24a],
N. De Groot [116], P. de Jong [117], H. De la Torre [118], A. De Maria [114a], A. De Salvo [76a],
U. De Sanctis [77a,77b], F. De Santis [71a,71b], A. De Santo [149], J.B. De Vivie De Regie [61],
D.V. Dedovich [39], J. Degens [94], A.M. Deiana [45], F. Del Corso [24b,24a], J. Del Peso [101],
F. Del Rio [64a], L. Delagrange [130], F. Deliot [138], C.M. Delitzsch [50], M. Della Pietra [73a,73b],
D. Della Volpe [57], A. Dell'Acqua [37], L. Dell'Asta [72a,72b], M. Delmastro [4], P.A. Delsart [61],
S. Demers [175], M. Demichev [39], S.P. Denisov [38], L. D'Eramo [41], D. Derendarz [88], F. Derue [130],
P. Dervan [94], K. Desch [25], C. Deutsch [25], F.A. Di Bello [58b,58a], A. Di Ciaccio [77a,77b],
L. Di Ciaccio [4], A. Di Domenico [76a,76b], C. Di Donato [73a,73b], A. Di Girolamo [37],
G. Di Gregorio [37], A. Di Luca [79a,79b], B. Di Micco [78a,78b], R. Di Nardo [78a,78b], K.F. Di Petrillo [40],
M. Diamantopoulou [35], F.A. Dias [117], T. Dias Do Vale [145], M.A. Diaz [140a,140b],
F.G. Diaz Capriles [25], A.R. Didenko [39], M. Didenko [166], E.B. Diehl [108], S. Díez Cornell [49],
C. Diez Pardos [144], C. Dimitriadi [164], A. Dimitrievska [21], J. Dingfelder [25], T. Dingley [129],
I-M. Dinu [28b], S.J. Dittmeier [64b], F. Dittus [37], M. Divisek [136], F. Djama [104], T. Djobava [152b],
C. Doglioni [103,100], A. Dohnalova [29a], J. Dolejsi [136], Z. Dolezal [136], K. Domijan [87a],
K.M. Dona [40], M. Donadelli [84d], B. Dong [109], J. Donini [41], A. D'Onofrio [73a,73b],
M. D'Onofrio [94], J. Dopke [137], A. Doria [73a], N. Dos Santos Fernandes [133a], P. Dougan [103],
M.T. Dova [92], A.T. Doyle [60], M.A. Draguet [129], E. Dreyer [172], I. Drivas-koulouris [10],
M. Drnevich [120], M. Drozdova [57], D. Du [63a], T.A. du Pree [117], F. Dubinin [38], M. Dubovsky [29a],
E. Duchovni [172], G. Duckeck [111], O.A. Ducu [28b], D. Duda [53], A. Dudarev [37], E.R. Duden [27],
M. D'uffizi [103], L. Duflot [67], M. Dührssen [37], I. Duminica [28g], A.E. Dumitriu [28b],
M. Dunford [64a], S. Dungs [50], K. Dunne [48a,48b], A. Duperrin [104], H. Duran Yildiz [3a],
M. Düren [59], A. Durglishvili [152b], B.L. Dwyer [118], G.I. Dyckes [18a], M. Dyndal [87a],
B.S. Dziedzic [37], Z.O. Earnshaw [149], G.H. Eberwein [129], B. Eckerova [29a], S. Eggebrecht [56],
E. Egidio Purcino De Souza [130], L.F. Ehrke [57], G. Eigen [17], K. Einsweiler [18a], T. Ekelof [164],
P.A. Ekman [100], S. El Farkh [36b], Y. El Ghazali [36b], H. El Jarrari [37], A. El Moussaouy [36a],
V. Ellajosyula [164], M. Ellert [164], F. Ellinghaus [174], N. Ellis [37], J. Elmsheuser [30], M. Elsawy [119a],
M. Elsing [37], D. Emeliyanov [137], Y. Enari [156], I. Ene [18a], S. Epari [13], P.A. Erland [88],
D. Ernani Martins Neto [88], M. Errenst [174], M. Escalier [67], C. Escobar [166], E. Etzion [154],

G. Evans [133a], H. Evans [69], L.S. Evans [97], A. Ezhilov [38], S. Ezzarqtouni [36a], F. Fabbri [24b,24a],
L. Fabbri [24b,24a], G. Facini [98], V. Fadeyev [139], R.M. Fakhrutdinov [38], D. Fakoudis [102],
S. Falciano [76a], L.F. Falda Ulhoa Coelho [37], F. Fallavollita [112], G. Falsetti [44b,44a], J. Faltova [136],
C. Fan [165], Y. Fan [14], Y. Fang [14,114c], M. Fanti [72a,72b], M. Faraj [70a,70b], Z. Farazpay [99],
A. Farbin [8], A. Farilla [78a], T. Farooque [109], S.M. Farrington [53], F. Fassi [36e], D. Fassouliotis [9],
M. Faucci Giannelli [77a,77b], W.J. Fawcett [33], L. Fayard [67], P. Federic [136], P. Federicova [134],
O.L. Fedin [38,a], M. Feickert [173], L. Feligioni [104], D.E. Fellers [126], C. Feng [63b], M. Feng [15],
Z. Feng [117], M.J. Fenton [162], L. Ferencz [49], R.A.M. Ferguson [93], S.I. Fernandez Luengo [140f],
P. Fernandez Martinez [13], M.J.V. Fernoux [104], J. Ferrando [93], A. Ferrari [164], P. Ferrari [117,116],
R. Ferrari [74a], D. Ferrere [57], C. Ferretti [108], D. Fiacco [76a,76b], F. Fiedler [102], P. Fiedler [135],
A. Filipčič [95], E.K. Filmer [1], F. Filthaut [116], M.C.N. Fiolhais [133a,133c,c], L. Fiorini [166],
W.C. Fisher [109], T. Fitschen [103], P.M. Fitzhugh [138], I. Fleck [144], P. Fleischmann [108], T. Flick [174],
M. Flores [34d,aa], L.R. Flores Castillo [65a], L. Flores Sanz De Acedo [37], F.M. Follega [79a,79b],
N. Fomin [33], J.H. Foo [158], A. Formica [138], A.C. Forti [103], E. Fortin [37], A.W. Fortman [18a],
M.G. Foti [18a], L. Fountas [9,j], D. Fournier [67], H. Fox [93], P. Francavilla [75a,75b], S. Francescato [62],
S. Franchellucci [57], M. Franchini [24b,24a], S. Franchino [64a], D. Francis [37], L. Franco [116],
V. Franco Lima [37], L. Franconi [49], M. Franklin [62], G. Frattari [27], Y.Y. Frid [154], J. Friend [60],
N. Fritzsche [51], A. Froch [55], D. Froidevaux [37], J.A. Frost [129], Y. Fu [63a],
S. Fuenzalida Garrido [140f], M. Fujimoto [104], K.Y. Fung [65a], E. Furtado De Simas Filho [84e],
M. Furukawa [156], J. Fuster [166], A. Gaa [56], A. Gabrielli [24b,24a], A. Gabrielli [158], P. Gadow [37],
G. Gagliardi [58b,58a], L.G. Gagnon [18a], S. Gaid [163], S. Galantzan [154], E.J. Gallas [129],
B.J. Gallop [137], K.K. Gan [122], S. Ganguly [156], Y. Gao [53], F.M. Garay Walls [140a,140b], B. Garcia [30],
C. García [166], A. Garcia Alonso [117], A.G. Garcia Caffaro [175], J.E. García Navarro [166],
M. Garcia-Sciveres [18a], G.L. Gardner [131], R.W. Gardner [40], N. Garelli [161], D. Garg [81],
R.B. Garg [146], J.M. Gargan [53], C.A. Garner [158], C.M. Garvey [34a], V.K. Gassmann [161], G. Gaudio [74a],
V. Gautam [13], P. Gauzzi [76a,76b], J. Gavranovic [95], I.L. Gavrilenko [38], A. Gavrilyuk [38], C. Gay [167],
G. Gaycken [126], E.N. Gazis [10], A.A. Geanta [28b], C.M. Gee [139], A. Gekow [122], C. Gemme [58b],
M.H. Genest [61], A.D. Gentry [115], S. George [97], W.F. George [21], T. Geralis [47],
P. Gessinger-Befurt [37], M.E. Geyik [174], M. Ghani [170], K. Ghorbanian [96], A. Ghosal [144],
A. Ghosh [162], A. Ghosh [7], B. Giacobbe [24b], S. Giagu [76a,76b], T. Giani [117], A. Giannini [63a],
S.M. Gibson [97], M. Gignac [139], D.T. Gil [87b], A.K. Gilbert [87a], B.J. Gilbert [42], D. Gillberg [35],
G. Gilles [117], L. Ginabat [130], D.M. Gingrich [2,ad], M.P. Giordani [70a,70c], P.F. Giraud [138],
G. Giugliarelli [70a,70c], D. Giugni [72a], F. Giuli [37], I. Gkialas [9,j], L.K. Gladilin [38], C. Glasman [101],
G.R. Gledhill [126], G. Glemža [49], M. Glisic [126], I. Gnesi [44b,e], Y. Go [30], M. Goblirsch-Kolb [37],
B. Gocke [50], D. Godin [110], B. Gokturk [22a], S. Goldfarb [107], T. Golling [57], M.G.D. Gololo [34g],
D. Golubkov [38], J.P. Gombas [109], A. Gomes [133a,133b], G. Gomes Da Silva [144],
A.J. Gomez Delegido [166], R. Gonçalo [133a], L. Gonella [21], A. Gongadze [152c], F. Gonnella [21],
J.L. Gonski [146], R.Y. González Andana [53], S. González de la Hoz [166], R. Gonzalez Lopez [94],
C. Gonzalez Renteria [18a], M.V. Gonzalez Rodrigues [49], R. Gonzalez Suarez [164],
S. Gonzalez-Sevilla [57], L. Goossens [37], B. Gorini [37], E. Gorini [71a,71b], A. Gorišek [95],
T.C. Gosart [131], A.T. Goshaw [52], M.I. Gostkin [39], S. Goswami [124], C.A. Gottardo [37],
S.A. Gotz [111], M. Gouighri [36b], V. Goumarre [49], A.G. Goussiou [141], N. Govender [34c],
I. Grabowska-Bold [87a], K. Graham [35], E. Gramstad [128], S. Grancagnolo [71a,71b], C.M. Grant [1,138],
P.M. Gravila [28f], F.G. Gravili [71a,71b], H.M. Gray [18a], M. Greco [71a,71b], M.J. Green [1], C. Grefe [25],
A.S. Grefsrud [17], I.M. Gregor [49], K.T. Greif [162], P. Grenier [146], S.G. Grewe [112], A.A. Grillo [139],
K. Grimm [32], S. Grinstein [13,s], J.-F. Grivaz [67], E. Gross [172], J. Grosse-Knetter [56],
J.C. Grundy [129], L. Guan [108], J.G.R. Guerrero Rojas [166], G. Guerrieri [70a,70c], R. Gugel [102],

J.A.M. Guhit [108], A. Guida [19], E. Guilloton [170], S. Guindon [37], F. Guo [14,114c], J. Guo [63c],
L. Guo [49], Y. Guo [108], R. Gupta [132], S. Gurbuz [25], S.S. Gurdasani [55], G. Gustavino [76a,76b],
P. Gutierrez [123], L.F. Gutierrez Zagazeta [131], M. Gutsche [51], C. Gutschow [98], C. Gwenlan [129],
C.B. Gwilliam [94], E.S. Haaland [128], A. Haas [120], M. Habedank [49], C. Haber [18a],
H.K. Hadavand [8], A. Hadef [51], S. Hadzic [112], A.I. Hagan [93], J.J. Hahn [144], E.H. Haines [98],
M. Haleem [169], J. Haley [124], J.J. Hall [142], G.D. Hallewell [104], L. Halser [20], K. Hamano [168],
M. Hamer [25], G.N. Hamity [53], E.J. Hampshire [97], J. Han [63b], K. Han [63a], L. Han [114a],
L. Han [63a], S. Han [18a], Y.F. Han [158], K. Hanagaki [85], M. Hance [139], D.A. Hangal [42],
H. Hanif [145], M.D. Hank [131], J.B. Hansen [43], P.H. Hansen [43], K. Hara [160], D. Harada [57],
T. Harenberg [174], S. Harkusha [38], M.L. Harris [105], Y.T. Harris [129], J. Harrison [13],
N.M. Harrison [122], P.F. Harrison [170], N.M. Hartman [112], N.M. Hartmann [111], R.Z. Hasan [97,137],
Y. Hasegawa [143], S. Hassan [17], R. Hauser [109], C.M. Hawkes [21], R.J. Hawkings [37],
Y. Hayashi [156], S. Hayashida [113], D. Hayden [109], C. Hayes [108], R.L. Hayes [117], C.P. Hays [129],
J.M. Hays [96], H.S. Hayward [94], F. He [63a], M. He [14,114c], Y. He [157], Y. He [49], Y. He [98],
N.B. Heatley [96], V. Hedberg [100], A.L. Heggelund [128], N.D. Hehir [96,*], C. Heidegger [55],
K.K. Heidegger [55], J. Heilman [35], S. Heim [49], T. Heim [18a], J.G. Heinlein [131], J.J. Heinrich [126],
L. Heinrich [112,ab], J. Hejbal [134], A. Held [173], S. Hellesund [17], C.M. Helling [167],
S. Hellman [48a,48b], R.C.W. Henderson [93], L. Henkelmann [33], A.M. Henriques Correia [37], H. Herde [100],
Y. Hernández Jiménez [148], L.M. Herrmann [25], T. Herrmann [51], G. Herten [55], R. Hertenberger [111],
L. Hervas [37], M.E. Hesping [102], N.P. Hessey [159a], M. Hidaoui [36b], N. Hidic [136], E. Hill [158],
S.J. Hillier [21], J.R. Hinds [109], F. Hinterkeuser [25], M. Hirose [127], S. Hirose [160],
D. Hirschbuehl [174], T.G. Hitchings [103], B. Hiti [95], J. Hobbs [148], R. Hobincu [28e], N. Hod [172],
M.C. Hodgkinson [142], B.H. Hodkinson [129], A. Hoecker [37], D.D. Hofer [108], J. Hofer [49],
T. Holm [25], M. Holzbock [112], L.B.A.H. Hommels [33], B.P. Honan [103], J.J. Hong [69], J. Hong [63c],
T.M. Hong [132], B.H. Hooberman [165], W.H. Hopkins [6], M.C. Hoppesch [165], Y. Horii [113],
S. Hou [151], A.S. Howard [95], J. Howarth [60], J. Hoya [6], M. Hrabovsky [125], A. Hrynevich [49],
T. Hryn'ova [4], P.J. Hsu [66], S.-C. Hsu [141], T. Hsu [67], M. Hu [18a], Q. Hu [63a], S. Huang [65b],
X. Huang [14,114c], Y. Huang [142], Y. Huang [102], Y. Huang [14], Z. Huang [103], Z. Hubacek [135],
M. Huebner [25], F. Huegging [25], T.B. Huffman [129], C.A. Hugli [49], M. Huhtinen [37],
S.K. Huiberts [17], R. Hulsken [106], N. Huseynov [12,g], J. Huston [109], J. Huth [62], R. Hyneman [146],
G. Iacobucci [57], G. Iakovidis [30], L. Iconomidou-Fayard [67], J.P. Iddon [37], P. Iengo [73a,73b],
R. Iguchi [156], Y. Iiyama [156], T. Iizawa [129], Y. Ikegami [85], N. Ilic [158], H. Imam [36a],
M. Ince Lezki [57], T. Ingebretsen Carlson [48a,48b], J.M. Inglis [96], G. Introzzi [74a,74b], M. Iodice [78a],
V. Ippolito [76a,76b], R.K. Irwin [94], M. Ishino [156], W. Islam [173], C. Issever [19,49], S. Istin [22a,ah],
H. Ito [171], R. Iuppa [79a,79b], A. Ivina [172], J.M. Izen [46], V. Izzo [73a], P. Jacka [134], P. Jackson [1],
C.S. Jagfeld [111], G. Jain [159a], P. Jain [49], K. Jakobs [55], T. Jakoubek [172], J. Jamieson [60],
W. Jang [156], M. Javurkova [105], P. Jawahar [103], L. Jeanty [126], J. Jejelava [152a,z], P. Jenni [55,f],
C.E. Jessiman [35], C. Jia [63b], J. Jia [148], X. Jia [62], X. Jia [14,114c], Z. Jia [114a], C. Jiang [53],
S. Jiggins [49], J. Jimenez Pena [13], S. Jin [114a], A. Jinaru [28b], O. Jinnouchi [157], P. Johansson [142],
K.A. Johns [7], J.W. Johnson [139], D.M. Jones [149], E. Jones [49], P. Jones [33], R.W.L. Jones [93],
T.J. Jones [94], H.L. Joos [56,37], R. Joshi [122], J. Jovicevic [16], X. Ju [18a], J.J. Junggeburth [105],
T. Junkermann [64a], A. Juste Rozas [13,s], M.K. Juzek [88], S. Kabana [140e], A. Kaczmarska [88],
M. Kado [112], H. Kagan [122], M. Kagan [146], A. Kahn [131], C. Kahra [102], T. Kaji [156],
E. Kajomovitz [153], N. Kakati [172], I. Kalaitzidou [55], C.W. Kalderon [30], N.J. Kang [139],
D. Kar [34g], K. Karava [129], M.J. Kareem [159b], E. Karentzos [55], O. Karkout [117], S.N. Karpov [39],
Z.M. Karpova [39], V. Kartvelishvili [93], A.N. Karyukhin [38], E. Kasimi [155], J. Katzy [49], S. Kaur [35],
K. Kawade [143], M.P. Kawale [123], C. Kawamoto [89], T. Kawamoto [63a], E.F. Kay [37], F.I. Kaya [161],

S. Kazakos [109], V.F. Kazanin [38], Y. Ke [148], J.M. Keaveney [34a], R. Keeler [168], G.V. Kehris [62],
J.S. Keller [35], A.S. Kelly [98], J.J. Kempster [149], P.D. Kennedy [102], O. Kepka [134], B.P. Kerridge [137],
S. Kersten [174], B.P. Kerševan [95], L. Keszeghova [29a], S. Ketabchi Haghighat [158], R.A. Khan [132],
A. Khanov [124], A.G. Kharlamov [38], T. Kharlamova [38], E.E. Khoda [141], M. Kholodenko [38],
T.J. Khoo [19], G. Khoriauli [169], J. Khubua [152b], Y.A.R. Khwaira [130], B. Kibirige [34g], D. Kim [6],
D.W. Kim [48a,48b], Y.K. Kim [40], N. Kimura [98], M.K. Kingston [56], A. Kirchhoff [56], C. Kirfel [25],
F. Kirfel [25], J. Kirk [137], A.E. Kiryunin [112], C. Kitsaki [10], O. Kivernyk [25], M. Klassen [161],
C. Klein [35], L. Klein [169], M.H. Klein [45], S.B. Klein [57], U. Klein [94], P. Klimek [37],
A. Klimentov [30], T. Klioutchnikova [37], P. Kluit [117], S. Kluth [112], E. Kneringer [80],
T.M. Knight [158], A. Knue [50], R. Kobayashi [89], D. Kobylianskii [172], S.F. Koch [129],
M. Kocian [146], P. Kodyš [136], D.M. Koeck [126], P.T. Koenig [25], T. Koffas [35], O. Kolay [51],
I. Koletsou [4], T. Komarek [88], K. Köneke [55], A.X.Y. Kong [1], T. Kono [121], N. Konstantinidis [98],
P. Kontaxakis [57], B. Konya [100], R. Kopeliansky [42], S. Koperny [87a], K. Korcyl [88],
K. Kordas [155,d], A. Korn [98], S. Korn [56], I. Korolkov [13], N. Korotkova [38], B. Kortman [117],
O. Kortner [112], S. Kortner [112], W.H. Kostecka [118], V.V. Kostyukhin [144], A. Kotsokechagia [138],
A. Kotwal [52], A. Koulouris [37], A. Kourkoumeli-Charalampidi [74a,74b], C. Kourkoumelis [9],
E. Kourlitis [112,ab], O. Kovanda [126], R. Kowalewski [168], W. Kozanecki [138], A.S. Kozhin [38],
V.A. Kramarenko [38], G. Kramberger [95], P. Kramer [102], M.W. Krasny [130], A. Krasznahorkay [37],
A.C. Kraus [118], J.W. Kraus [174], J.A. Kremer [49], T. Kresse [51], L. Kretschmann [174],
J. Kretzschmar [94], K. Kreul [19], P. Krieger [158], S. Krishnamurthy [105], M. Krivos [136],
K. Krizka [21], K. Kroeninger [50], H. Kroha [112], J. Kroll [134], J. Kroll [131], K.S. Krowpman [109],
U. Kruchonak [39], H. Krüger [25], N. Krumnack [82], M.C. Kruse [52], O. Kuchinskaia [38], S. Kuday [3a],
S. Kuehn [37], R. Kuesters [55], T. Kuhl [49], V. Kukhtin [39], Y. Kulchitsky [38,a], S. Kuleshov [140d,140b],
M. Kumar [34g], N. Kumari [49], P. Kumari [159b], A. Kupco [134], T. Kupfer [50], A. Kupich [38],
O. Kuprash [55], H. Kurashige [86], L.L. Kurchaninov [159a], O. Kurdysh [67], Y.A. Kurochkin [38],
A. Kurova [38], M. Kuze [157], A.K. Kvam [105], J. Kvita [125], T. Kwan [106], N.G. Kyriacou [108],
L.A.O. Laatu [104], C. Lacasta [166], F. Lacava [76a,76b], H. Lacker [19], D. Lacour [130], N.N. Lad [98],
E. Ladygin [39], A. Lafarge [41], B. Laforge [130], T. Lagouri [175], F.Z. Lahbabi [36a], S. Lai [56],
J.E. Lambert [168], S. Lammers [69], W. Lampl [7], C. Lampoudis [155,d], G. Lamprinoudis [102],
A.N. Lancaster [118], E. Lançon [30], U. Landgraf [55], M.P.J. Landon [96], V.S. Lang [55],
O.K.B. Langrekken [128], A.J. Lankford [162], F. Lanni [37], K. Lantzsch [25], A. Lanza [74a],
J.F. Laporte [138], T. Lari [72a], F. Lasagni Manghi [24b], M. Lassnig [37], V. Latonova [134],
A. Laurier [153], S.D. Lawlor [142], Z. Lawrence [103], R. Lazaridou [170], M. Lazzaroni [72a,72b], B. Le [103],
E.M. Le Boulicaut [52], L.T. Le Pottier [18a], B. Leban [24b,24a], A. Lebedev [82], M. LeBlanc [103],
F. Ledroit-Guillon [61], S.C. Lee [151], S. Lee [48a,48b], T.F. Lee [94], L.L. Leeuw [34c], H.P. Lefebvre [97],
M. Lefebvre [168], C. Leggett [18a], G. Lehmann Miotto [37], M. Leigh [57], W.A. Leight [105],
W. Leinonen [116], A. Leisos [155,r], M.A.L. Leite [84c], C.E. Leitgeb [19], R. Leitner [136],
K.J.C. Leney [45], T. Lenz [25], S. Leone [75a], C. Leonidopoulos [53], A. Leopold [147], R. Les [109],
C.G. Lester [33], M. Levchenko [38], J. Levêque [4], L.J. Levinson [172], G. Levrini [24b,24a],
M.P. Lewicki [88], C. Lewis [141], D.J. Lewis [4], A. Li [5], B. Li [63b], C. Li [63a], C-Q. Li [112], H. Li [63a],
H. Li [63b], H. Li [114a], H. Li [15], H. Li [63b], J. Li [63c], K. Li [141], L. Li [63c], M. Li [14,114c],
S. Li [14,114c], S. Li [63d,63c], T. Li [5], X. Li [106], Z. Li [129], Z. Li [156], Z. Li [14,114c], S. Liang [14,114c],
Z. Liang [14], M. Liberatore [138], B. Liberti [77a], K. Lie [65c], J. Lieber Marin [84e], H. Lien [69],
H. Lin [108], K. Lin [109], R.E. Lindley [7], J.H. Lindon [2], J. Ling [62], E. Lipeles [131],
A. Lipniacka [17], A. Lister [167], J.D. Little [69], B. Liu [14], B.X. Liu [114b], D. Liu [63d,63c],
E.H.L. Liu [21], J.B. Liu [63a], J.K.K. Liu [33], K. Liu [63d], K. Liu [63d,63c], M. Liu [63a], M.Y. Liu [63a],
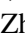P. Liu [14], Q. Liu [63d,141,63c], X. Liu [63a], X. Liu [63b], Y. Liu [114b,114c], Y.L. Liu [63b], Y.W. Liu [63a],
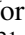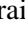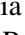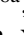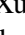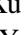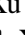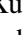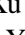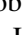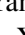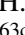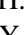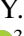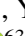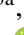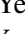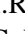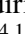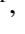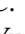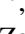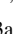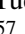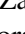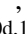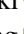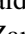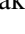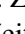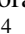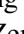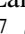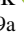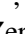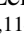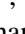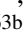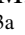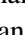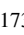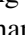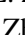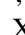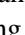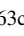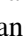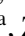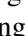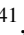
J. Llorente Merino [145], S.L. Lloyd [96], E.M. Lobodzinska [49], P. Loch [7], T. Lohse [19],
K. Lohwasser [142], E. Loiacono [49], M. Lokajicek [134,*], J.D. Lomas [21], J.D. Long [165],
I. Longarini [162], R. Longo [165], I. Lopez Paz [68], A. Lopez Solis [49], N. Lorenzo Martinez [4],
A.M. Lory [111], M. Losada [119a], G. Löschcke Centeno [149], O. Loseva [38], X. Lou [48a,48b],
X. Lou [14,114c], A. Lounis [67], P.A. Love [93], G. Lu [14,114c], M. Lu [67], S. Lu [131], Y.J. Lu [66],
H.J. Lubatti [141], C. Luci [76a,76b], F.L. Lucio Alves [114a], F. Luehring [69], I. Luise [148],
O. Lukianchuk [67], O. Lundberg [147], B. Lund-Jensen [147], N.A. Luongo [6], M.S. Lutz [37],
A.B. Lux [26], D. Lynn [30], R. Lysak [134], E. Lytken [100], V. Lyubushkin [39], T. Lyubushkina [39],
M.M. Lyukova [148], M.Firdaus M. Soberi [53], H. Ma [30], K. Ma [63a], L.L. Ma [63b], W. Ma [63a],
Y. Ma [124], J.C. MacDonald [102], P.C. Machado De Abreu Farias [84e], R. Madar [41], T. Madula [98],
J. Maeda [86], T. Maeno [30], H. Maguire [142], V. Maiboroda [138], A. Maio [133a,133b,133d], K. Maj [87a],
O. Majersky [49], S. Majewski [126], N. Makovec [67], V. Maksimovic [16], B. Malaescu [130],
Pa. Malecki [88], V.P. Maleev [38], F. Malek [61,n], M. Mali [95], D. Malito [97], U. Mallik [81],
S. Maltezos [10], S. Malyukov [39], J. Mamuzic [13], G. Mancini [54], M.N. Mancini [27], G. Manco [74a,74b],
J.P. Mandalia [96], S.S. Mandarry [149], I. Mandić [95], L. Manhaes de Andrade Filho [84a],
I.M. Maniatis [172], J. Manjarres Ramos [91], D.C. Mankad [172], A. Mann [111], A. Manousos [80],
S. Manzoni [37], L. Mao [63c], X. Mapekula [34c], A. Marantis [155,r], G. Marchiori [5],
M. Marcisovsky [134], C. Marcon [72a], M. Marinescu [21], S. Marium [49], M. Marjanovic [123],
A. Markhoos [55], M. Markovitch [67], E.J. Marshall [93], Z. Marshall [18a], S. Marti-Garcia [166],
J. Martin [98], T.A. Martin [137], V.J. Martin [53], B. Martin dit Latour [17], L. Martinelli [76a,76b],
M. Martinez [13,s], P. Martinez Agullo [166], V.I. Martinez Outschoorn [105], P. Martinez Suarez [13],
S. Martin-Haugh [137], G. Martinovicova [136], V.S. Martoiu [28b], A.C. Martyniuk [98], A. Marzin [37],
D. Mascione [79a,79b], L. Masetti [102], T. Mashimo [156], J. Masik [103], A.L. Maslennikov [38],
P. Massarotti [73a,73b], P. Mastrandrea [75a,75b], A. Mastroberardino [44b,44a], T. Masubuchi [156],
T. Mathisen [164], J. Matousek [136], N. Matsuzawa [156], J. Maurer [28b], A.J. Maury [67], B. Maček [95],
D.A. Maximov [38], A.E. May [103], R. Mazini [151], I. Maznas [118], M. Mazza [109], S.M. Mazza [139],
E. Mazzeo [72a,72b], C. Mc Ginn [30], J.P. Mc Gowan [168], S.P. Mc Kee [108], C.C. McCracken [167],
E.F. McDonald [107], A.E. McDougall [117], J.A. Mcfayden [149], R.P. McGovern [131],
R.P. Mckenzie [34g], T.C. Mclachlan [49], D.J. Mclaughlin [98], S.J. McMahon [137],
C.M. Mcpartland [94], R.A. McPherson [168,w], S. Mehlhase [111], A. Mehta [94], D. Melini [166],
B.R. Mellado Garcia [34g], A.H. Melo [56], F. Meloni [49], A.M. Mendes Jacques Da Costa [103],
H.Y. Meng [158], L. Meng [93], S. Menke [112], M. Mentink [37], E. Meoni [44b,44a], G. Mercado [118],
S. Merianos [155], C. Merlassino [70a,70c], L. Merola [73a,73b], C. Meroni [72a,72b], J. Metcalfe [6],
A.S. Mete [6], E. Meuser [102], C. Meyer [69], J-P. Meyer [138], R.P. Middleton [137], L. Mijović [53],
G. Mikenberg [172], M. Mikestikova [134], M. Mikuž [95], H. Mildner [102], A. Milic [37],
D.W. Miller [40], E.H. Miller [146], L.S. Miller [35], A. Milov [172], D.A. Milstead [48a,48b], T. Min [114a],
A.A. Minaenko [38], I.A. Minashvili [152b], L. Mince [60], A.I. Mincer [120], B. Mindur [87a],
M. Mineev [39], Y. Mino [89], L.M. Mir [13], M. Miralles Lopez [60], M. Mironova [18a], A. Mishima [156],
M.C. Missio [116], A. Mitra [170], V.A. Mitsou [166], Y. Mitsumori [113], O. Miu [158],
P.S. Miyagawa [96], T. Mkrtchyan [64a], M. Mlinarevic [98], T. Mlinarevic [98], M. Mlynarikova [37],
S. Mobius [20], P. Mogg [111], M.H. Mohamed Farook [115], A.F. Mohammed [14,114c], S. Mohapatra [42],
G. Mokgatitswane [34g], L. Moleri [172], B. Mondal [144], S. Mondal [135], K. Mönig [49],
E. Monnier [104], L. Monsonis Romero [166], J. Montejo Berlingen [13], M. Montella [122],
F. Montereali [78a,78b], F. Monticelli [92], S. Monzani [70a,70c], N. Morange [67],
A.L. Moreira De Carvalho [49], M. Moreno Llácer [166], C. Moreno Martinez [57], P. Morettini [58b],
S. Morgenstern [37], M. Morii [62], M. Morinaga [156], F. Morodei [76a,76b], L. Morvaj [37],
P. Moschovakos [37], B. Moser [37], M. Mosidze [152b], T. Moskalets [45], P. Moskvitina [116],

J. Moss [32,k], P. Moszkowicz [87a], A. Moussa [36d], E.J.W. Moyse [105], O. Mtintsilana [34g],
S. Muanza [104], J. Mueller [132], D. Muenstermann [93], R. Müller [37], G.A. Mullier [164],
A.J. Mullin [33], J.J. Mullin [131], D.P. Mungo [158], D. Munoz Perez [166], F.J. Munoz Sanchez [103],
M. Murin [103], W.J. Murray [170,137], M. Muškinja [95], C. Mwewa [30], A.G. Myagkov [38,a],
A.J. Myers [8], G. Myers [108], M. Myska [135], B.P. Nachman [18a], O. Nackenhorst [50], K. Nagai [129],
K. Nagano [85], J.L. Nagle [30,af], E. Nagy [104], A.M. Nairz [37], Y. Nakahama [85], K. Nakamura [85],
K. Nakkalil [5], H. Nanjo [127], E.A. Narayanan [115], I. Naryshkin [38], L. Nasella [72a,72b],
M. Naseri [35], S. Nasri [119b], C. Nass [25], G. Navarro [23a], J. Navarro-Gonzalez [166], R. Nayak [154],
A. Nayaz [19], P.Y. Nechaeva [38], S. Nechaeva [24b,24a], F. Nechansky [49], L. Nedic [129], T.J. Neep [21],
A. Negri [74a,74b], M. Negrini [24b], C. Nellist [117], C. Nelson [106], K. Nelson [108], S. Nemecek [134],
M. Nessi [37,h], M.S. Neubauer [165], F. Neuhaus [102], J. Neundorf [49], P.R. Newman [21],
C.W. Ng [132], Y.W.Y. Ng [49], B. Ngair [119a], H.D.N. Nguyen [110], R.B. Nickerson [129],
R. Nicolaidou [138], J. Nielsen [139], M. Niemeyer [56], J. Niermann [56], N. Nikiforou [37],
V. Nikolaenko [38,a], I. Nikolic-Audit [130], K. Nikolopoulos [21], P. Nilsson [30], I. Ninca [49],
G. Ninio [154], A. Nisati [76a], N. Nishu [2], R. Nisius [112], J-E. Nitschke [51], E.K. Nkadimeng [34g],
T. Nobe [156], T. Nommensen [150], M.B. Norfolk [142], B.J. Norman [35], M. Noury [36a], J. Novak [95],
T. Novak [95], L. Novotny [135], R. Novotny [115], L. Nozka [125], K. Ntekas [162],
N.M.J. Nunes De Moura Junior [84b], J. Ocariz [130], A. Ochi [86], I. Ochoa [133a], S. Oerdek [49,t],
J.T. Offermann [40], A. Ogrodnik [136], A. Oh [103], C.C. Ohm [147], H. Oide [85], R. Oishi [156],
M.L. Ojeda [49], Y. Okumura [156], L.F. Oleiro Seabra [133a], I. Oleksiyuk [57], S.A. Olivares Pino [140d],
G. Oliveira Correa [13], D. Oliveira Damazio [30], D. Oliveira Goncalves [84a], J.L. Oliver [162],
Ö.O. Öncel [55], A.P. O'Neill [20], A. Onofre [133a,133e], P.U.E. Onyisi [11], M.J. Oreglia [40],
G.E. Orellana [92], D. Orestano [78a,78b], N. Orlando [13], R.S. Orr [158], L.M. Osojnak [131],
R. Ospanov [63a], G. Otero y Garzon [31], H. Otono [90], P.S. Ott [64a], G.J. Ottino [18a], M. Ouchrif [36d],
F. Ould-Saada [128], T. Ovsiannikova [141], M. Owen [60], R.E. Owen [137], V.E. Ozcan [22a],
F. Ozturk [88], N. Ozturk [8], S. Ozturk [83], H.A. Pacey [129], A. Pacheco Pages [13],
C. Padilla Aranda [13], G. Padovano [76a,76b], S. Pagan Griso [18a], G. Palacino [69], A. Palazzo [71a,71b],
J. Pampel [25], J. Pan [175], T. Pan [65a], D.K. Panchal [11], C.E. Pandini [117],
J.G. Panduro Vazquez [137], H.D. Pandya [1], H. Pang [15], P. Pani [49], G. Panizzo [70a,70c],
L. Panwar [130], L. Paolozzi [57], S. Parajuli [165], A. Paramonov [6], C. Paraskevopoulos [54],
D. Paredes Hernandez [65b], A. Pareti [74a,74b], K.R. Park [42], T.H. Park [158], M.A. Parker [33],
F. Parodi [58b,58a], E.W. Parrish [118], V.A. Parrish [53], J.A. Parsons [42], U. Parzefall [55],
B. Pascual Dias [110], L. Pascual Dominguez [101], E. Pasqualucci [76a], S. Passaggio [58b], F. Pastore [97],
P. Patel [88], U.M. Patel [52], J.R. Pater [103], T. Pauly [37], C.I. Pazos [161], J. Pearkes [146],
M. Pedersen [128], R. Pedro [133a], S.V. Peleganchuk [38], O. Penc [37], E.A. Pender [53], G.D. Penn [175],
K.E. Penski [111], M. Penzin [38], B.S. Peralva [84d], A.P. Pereira Peixoto [141], L. Pereira Sanchez [146],
D.V. Perepelitsa [30,af], G. Perera [105], E. Perez Codina [159a], M. Perganti [10], H. Pernegger [37],
S. Perrella [76a,76b], O. Perrin [41], K. Peters [49], R.F.Y. Peters [103], B.A. Petersen [37],
T.C. Petersen [43], E. Petit [104], V. Petousis [135], C. Petridou [155,d], T. Petru [136], A. Petrukhin [144],
M. Pettee [18a], A. Petukhov [38], K. Petukhova [37], R. Pezoa [140f], L. Pezzotti [37], G. Pezzullo [175],
T.M. Pham [173], T. Pham [107], P.W. Phillips [137], G. Piacquadio [148], E. Pianori [18a], F. Piazza [126],
R. Piegaia [31], D. Pietreanu [28b], A.D. Pilkington [103], M. Pinamonti [70a,70c], J.L. Pinfold [2],
B.C. Pinheiro Pereira [133a], A.E. Pinto Pinoargote [138,138], L. Pintucci [70a,70c], K.M. Piper [149],
A. Pirttikoski [57], D.A. Pizzi [35], L. Pizzimento [65b], A. Pizzini [117], M.-A. Pleier [30], V. Pleskot [136],
E. Plotnikova [39], G. Poddar [96], R. Poettgen [100], L. Poggioli [130], I. Pokharel [56], S. Polacek [136],
G. Polesello [74a], A. Poley [145,159a], A. Polini [24b], C.S. Pollard [170], Z.B. Pollock [122],
E. Pompa Pacchi [76a,76b], N.I. Pond [98], D. Ponomarenko [116], L. Pontecorvo [37], S. Popa [28a],

G.A. Popeneciu [28d], A. Poreba [37], D.M. Portillo Quintero [159a], S. Pospisil [135], M.A. Postill [142],
P. Postolache [28c], K. Potamianos [170], P.A. Potepa [87a], I.N. Potrap [39], C.J. Potter [33], H. Potti [150],
J. Poveda [166], M.E. Pozo Astigarraga [37], A. Prades Ibanez [166], J. Pretel [55], D. Price [103],
M. Primavera [71a], M.A. Principe Martin [101], R. Privara [125], T. Procter [60], M.L. Proffitt [141],
N. Proklova [131], K. Prokofiev [65c], G. Proto [112], J. Proudfoot [6], M. Przybycien [87a],
W.W. Przygoda [87b], A. Psallidas [47], J.E. Puddefoot [142], D. Pudzha [55], D. Pyatiizbyantseva [38],
J. Qian [108], D. Qichen [103], Y. Qin [13], T. Qiu [53], A. Quadt [56], M. Queitsch-Maitland [103],
G. Quetant [57], R.P. Quinn [167], G. Rabanal Bolanos [62], D. Rafanoharana [55], F. Raffaeli [77a,77b],
F. Ragusa [72a,72b], J.L. Rainbolt [40], J.A. Raine [57], S. Rajagopalan [30], E. Ramakoti [38],
I.A. Ramirez-Berend [35], K. Ran [49,114c], D.S. Rankin [131], N.P. Rapheeha [34g], H. Rasheed [28b],
V. Raskina [130], D.F. Rassloff [64a], A. Rastogi [18a], S. Rave [102], S. Ravera [58b,58a], B. Ravina [56],
I. Ravinovich [172], M. Raymond [37], A.L. Read [128], N.P. Readioff [142], D.M. Rebuzzi [74a,74b],
G. Redlinger [30], A.S. Reed [112], K. Reeves [27], J.A. Reidelsturz [174], D. Reikher [154], A. Rej [50],
C. Rembser [37], M. Renda [28b], F. Renner [49], A.G. Rennie [162], A.L. Rescia [49], S. Resconi [72a],
M. Ressegotti [58b,58a], S. Rettie [37], J.G. Reyes Rivera [109], E. Reynolds [18a], O.L. Rezanova [38],
P. Reznicek [136], H. Riani [36d], N. Ribaric [93], E. Ricci [79a,79b], R. Richter [112], S. Richter [48a,48b],
E. Richter-Was [87b], M. Ridel [130], S. Ridouani [36d], P. Rieck [120], P. Riedler [37], E.M. Riefel [48a,48b],
J.O. Rieger [117], M. Rijssenbeek [148], M. Rimoldi [37], L. Rinaldi [24b,24a], P. Rincke [56,164],
T.T. Rinn [30], M.P. Rinnagel [111], G. Ripellino [164], I. Riu [13], J.C. Rivera Vergara [168],
F. Rizatdinova [124], E. Rizvi [96], B.R. Roberts [18a], S.H. Robertson [106,w], D. Robinson [33],
C.M. Robles Gajardo [140f], M. Robles Manzano [102], A. Robson [60], A. Rocchi [77a,77b], C. Roda [75a,75b],
S. Rodriguez Bosca [37], Y. Rodriguez Garcia [23a], A. Rodriguez Rodriguez [55],
A.M. Rodríguez Vera [118], S. Roe [37], J.T. Roemer [37], A.R. Roepe-Gier [139], O. Røhne [128],
R.A. Rojas [105], C.P.A. Roland [130], J. Roloff [30], A. Romaniouk [38], E. Romano [74a,74b],
M. Romano [24b], A.C. Romero Hernandez [165], N. Rompotis [94], L. Roos [130], S. Rosati [76a],
B.J. Rosser [40], E. Rossi [129], E. Rossi [73a,73b], L.P. Rossi [62], L. Rossini [55], R. Rosten [122],
M. Rotaru [28b], B. Rottler [55], C. Rougier [91], D. Rousseau [67], D. Rousso [49], A. Roy [165],
S. Roy-Garand [158], A. Rozanov [104], Z.M.A. Rozario [60], Y. Rozen [153], A. Rubio Jimenez [166],
A.J. Ruby [94], V.H. Ruelas Rivera [19], T.A. Ruggeri [1], A. Ruggiero [129], A. Ruiz-Martinez [166],
A. Rummler [37], Z. Rurikova [55], N.A. Rusakovich [39], H.L. Russell [168], G. Russo [76a,76b],
J.P. Rutherfoord [7], S. Rutherford Colmenares [33], M. Rybar [136], E.B. Rye [128], A. Ryzhov [45],
J.A. Sabater Iglesias [57], P. Sabatini [166], H.F-W. Sadrozinski [139], F. Safai Tehrani [76a],
B. Safarzadeh Samani [137], S. Saha [1], M. Sahinsoy [112], A. Saibel [166], M. Saimpert [138],
M. Saito [156], T. Saito [156], A. Sala [72a,72b], D. Salamani [37], A. Salnikov [146], J. Salt [166],
A. Salvador Salas [154], D. Salvatore [44b,44a], F. Salvatore [149], A. Salzburger [37], D. Sammel [55],
E. Sampson [93], D. Sampsonidis [155,d], D. Sampsonidou [126], J. Sánchez [166],
V. Sanchez Sebastian [166], H. Sandaker [128], C.O. Sander [49], J.A. Sandesara [105], M. Sandhoff [174],
C. Sandoval [23b], L. Sanfilippo [64a], D.P.C. Sankey [137], T. Sano [89], A. Sansoni [54], L. Santi [37,76b],
C. Santoni [41], H. Santos [133a,133b], A. Santra [172], E. Sanzani [24b,24a], K.A. Saoucha [163],
J.G. Saraiva [133a,133d], J. Sardain [7], O. Sasaki [85], K. Sato [160], C. Sauer [64b], E. Sauvan [4],
P. Savard [158,ad], R. Sawada [156], C. Sawyer [137], L. Sawyer [99], C. Sbarra [24b], A. Sbrizzi [24b,24a],
T. Scanlon [98], J. Schaarschmidt [141], U. Schäfer [102], A.C. Schaffer [67,45], D. Schaile [111],
R.D. Schamberger [148], C. Scharf [19], M.M. Schefer [20], V.A. Schegelsky [38], D. Scheirich [136],
M. Schernau [162], C. Scheulen [56], C. Schiavi [58b,58a], M. Schioppa [44b,44a], B. Schlag [146,m],
K.E. Schleicher [55], S. Schlenker [37], J. Schmeing [174], M.A. Schmidt [174], K. Schmieden [102],
C. Schmitt [102], N. Schmitt [102], S. Schmitt [49], L. Schoeffel [138], A. Schoening [64b],
P.G. Scholer [35], E. Schopf [129], M. Schott [25], J. Schovancova [37], S. Schramm [57], T. Schroer [57],

H-C. Schultz-Coulon [64a], M. Schumacher [55], B.A. Schumm [139], Ph. Schune [138], A.J. Schuy [141],
H.R. Schwartz [139], A. Schwartzman [146], T.A. Schwarz [108], Ph. Schwemling [138],
R. Schwienhorst [109], F.G. Sciacca [20], A. Sciandra [30], G. Sciolla [27], F. Scuri [75a],
C.D. Sebastiani [94], K. Sedlaczek [118], S.C. Seidel [115], A. Seiden [139], B.D. Seidlitz [42], C. Seitz [49],
J.M. Seixas [84b], G. Sekhniaidze [73a], L. Selem [61], N. Semprini-Cesari [24b,24a], D. Sengupta [57],
V. Senthilkumar [166], L. Serin [67], M. Sessa [77a,77b], H. Severini [123], F. Sforza [58b,58a], A. Sfyrla [57],
Q. Sha [14], E. Shabalina [56], A.H. Shah [33], R. Shaheen [147], J.D. Shahinian [131],
D. Shaked Renous [172], L.Y. Shan [14], M. Shapiro [18a], A. Sharma [37], A.S. Sharma [167],
P. Sharma [81], P.B. Shatalov [38], K. Shaw [149], S.M. Shaw [103], Q. Shen [63c], D.J. Sheppard [145],
P. Sherwood [98], L. Shi [98], X. Shi [14], C.O. Shimmin [175], J.D. Shinner [97], I.P.J. Shipsey [129],
S. Shirabe [90], M. Shiyakova [39,u], M.J. Shochet [40], D.R. Shope [128], B. Shrestha [123],
S. Shrestha [122,ag], M.J. Shroff [168], P. Sicho [134], A.M. Sickles [165], E. Sideras Haddad [34g],
A.C. Sidley [117], A. Sidoti [24b], F. Siegert [51], Dj. Sijacki [16], F. Sili [92], J.M. Silva [53],
I. Silva Ferreira [84b], M.V. Silva Oliveira [30], S.B. Silverstein [48a], S. Simion [67], R. Simoniello [37],
E.L. Simpson [103], H. Simpson [149], L.R. Simpson [108], N.D. Simpson [100], S. Simsek [83],
S. Sindhu [56], P. Sinervo [158], S. Singh [158], S. Sinha [49], S. Sinha [103], M. Sioli [24b,24a], I. Siral [37],
E. Sitnikova [49], J. Sjölin [48a,48b], A. Skaf [56], E. Skorda [21], P. Skubic [123], M. Slawinska [88],
V. Smakhtin [172], B.H. Smart [137], S.Yu. Smirnov [38], Y. Smirnov [38], L.N. Smirnova [38,a],
O. Smirnova [100], A.C. Smith [42], D.R. Smith [162], E.A. Smith [40], H.A. Smith [129], J.L. Smith [103],
R. Smith [146], M. Smizanska [93], K. Smolek [135], A.A. Snesarev [38], S.R. Snider [158], H.L. Snoek [117],
S. Snyder [30], R. Sobie [168,w], A. Soffer [154], C.A. Solans Sanchez [37], E.Yu. Soldatov [38],
U. Soldevila [166], A.A. Solodkov [38], S. Solomon [27], A. Soloshenko [39], K. Solovieva [55],
O.V. Solovyanov [41], P. Sommer [37], A. Sonay [13], W.Y. Song [159b], A. Sopczak [135], A.L. Sopio [98],
F. Sopkova [29b], J.D. Sorenson [115], I.R. Sotarriva Alvarez [157], V. Sothilingam [64a],
O.J. Soto Sandoval [140c,140b], S. Sottocornola [69], R. Soualah [163], Z. Soumaimi [36e], D. South [49],
N. Soybelman [172], S. Spagnolo [71a,71b], M. Spalla [112], D. Sperlich [55], G. Spigo [37], S. Spinali [93],
B. Spisso [73a,73b], D.P. Spiteri [60], M. Spousta [136], E.J. Staats [35], R. Stamen [64a], A. Stampekis [21],
M. Standke [25], E. Stanecka [88], W. Stanek-Maslouska [49], M.V. Stange [51], B. Stanislaus [18a],
M.M. Stanitzki [49], B. Stapf [49], E.A. Starchenko [38], G.H. Stark [139], J. Stark [91], P. Staroba [134],
P. Starovoitov [64a], S. Stärz [106], R. Staszewski [88], G. Stavropoulos [47], P. Steinberg [30],
B. Stelzer [145,159a], H.J. Stelzer [132], O. Stelzer-Chilton [159a], H. Stenzel [59], T.J. Stevenson [149],
G.A. Stewart [37], J.R. Stewart [124], M.C. Stockton [37], G. Stoicea [28b], M. Stolarski [133a],
S. Stonjek [112], A. Straessner [51], J. Strandberg [147], S. Strandberg [48a,48b], M. Stratmann [174],
M. Strauss [123], T. Strebler [104], P. Strizenec [29b], R. Ströhmer [169], D.M. Strom [126],
R. Stroynowski [45], A. Strubig [48a,48b], S.A. Stucci [30], B. Stugu [17], J. Stupak [123], N.A. Styles [49],
D. Su [146], S. Su [63a], W. Su [63d], X. Su [63a], D. Suchy [29a], K. Sugizaki [156], V.V. Sulin [38],
M.J. Sullivan [94], D.M.S. Sultan [129], L. Sultanaliyeva [38], S. Sultansoy [3b], T. Sumida [89],
S. Sun [173], O. Sunneborn Gudnadottir [164], N. Sur [104], M.R. Sutton [149], H. Suzuki [160],
M. Svatos [134], M. Swiatlowski [159a], T. Swirski [169], I. Sykora [29a], M. Sykora [136], T. Sykora [136],
D. Ta [102], K. Tackmann [49,t], A. Taffard [162], R. Tafirout [159a], J.S. Tafoya Vargas [67], Y. Takubo [85],
M. Talby [104], A.A. Talyshev [38], K.C. Tam [65b], N.M. Tamir [154], A. Tanaka [156], J. Tanaka [156],
R. Tanaka [67], M. Tanasini [148], Z. Tao [167], S. Tapia Araya [140f], S. Tapprogge [102],
A. Tarek Abouelfadl Mohamed [109], S. Tarem [153], K. Tariq [14], G. Tarna [28b], G.F. Tartarelli [72a],
M.J. Tartarin [91], P. Tas [136], M. Tasevsky [134], E. Tassi [44b,44a], A.C. Tate [165], G. Tateno [156],
Y. Tayalati [36e,v], G.N. Taylor [107], W. Taylor [159b], R. Teixeira De Lima [146], P. Teixeira-Dias [97],
J.J. Teoh [158], K. Terashi [156], J. Terron [101], S. Terzo [13], M. Testa [54], R.J. Teuscher [158,w],
A. Thaler [80], O. Theiner [57], N. Themistokleous [53], T. Theveneaux-Pelzer [104], O. Thielmann [174],

53

D.W. Thomas[97], J.P. Thomas [21], E.A. Thompson [18a], P.D. Thompson [21], E. Thomson [131],
R.E. Thornberry [45], C. Tian [63a], Y. Tian [56], V. Tikhomirov [38,a], Yu.A. Tikhonov [38],
S. Timoshenko[38], D. Timoshyn [136], E.X.L. Ting [1], P. Tipton [175], A. Tishelman-Charny [30],
S.H. Tlou [34g], K. Todome [157], S. Todorova-Nova [136], S. Todt[51], L. Toffolin [70a,70c], M. Togawa [85],
J. Tojo [90], S. Tokár [29a], K. Tokushuku [85], O. Toldaiev [69], R. Tombs [33], M. Tomoto [85,113],
L. Tompkins [146,m], K.W. Topolnicki [87b], E. Torrence [126], H. Torres [91], E. Torró Pastor [166],
M. Toscani [31], C. Tosciri [40], M. Tost [11], D.R. Tovey [142], I.S. Trandafir [28b], T. Trefzger [169],
A. Tricoli [30], I.M. Trigger [159a], S. Trincaz-Duvoid [130], D.A. Trischuk [27], B. Trocmé [61],
A. Tropina[39], L. Truong [34c], M. Trzebinski [88], A. Trzupek [88], F. Tsai [148], M. Tsai [108],
A. Tsiamis [155,d], P.V. Tsiareshka[38], S. Tsigaridas [159a], A. Tsirigotis [155,r], V. Tsiskaridze [158],
E.G. Tskhadadze [152a], M. Tsopoulou [155], Y. Tsujikawa [89], I.I. Tsukerman [38], V. Tsulaia [18a],
S. Tsuno [85], K. Tsuri [121], D. Tsybychev [148], Y. Tu [65b], A. Tudorache [28b], V. Tudorache [28b],
A.N. Tuna [62], S. Turchikhin [58b,58a], I. Turk Cakir [3a], R. Turra [72a], T. Turtuvshin [39,x],
P.M. Tuts [42], S. Tzamarias [155,d], E. Tzovara [102], F. Ukegawa [160], P.A. Ulloa Poblete [140c,140b],
E.N. Umaka [30], G. Unal [37], A. Undrus [30], G. Unel [162], J. Urban [29b], P. Urrejola [140a], G. Usai [8],
R. Ushioda [157], M. Usman [110], Z. Uysal [83], V. Vacek [135], B. Vachon [106], T. Vafeiadis [37],
A. Vaitkus [98], C. Valderanis [111], E. Valdes Santurio [48a,48b], M. Valente [159a], S. Valentinetti [24b,24a],
A. Valero [166], E. Valiente Moreno [166], C.Y. Vallgren [37], A. Vallier [91], J.A. Valls Ferrer [166],
D.R. Van Arneman [117], T.R. Van Daalen [141], A. Van Der Graaf [50], P. Van Gemmeren [6],
M. Van Rijnbach [37], S. Van Stroud [98], I. Van Vulpen [117], P. Vana [136], M. Vanadia [77a,77b],
W. Vandelli [37], E.R. Vandewall [124], D. Vannicola [154], L. Vannoli [54], R. Vari [76a], E.W. Varnes [7],
C. Varni [18b], T. Varol [151], D. Varouchas [67], L. Varriale [166], K.E. Varvell [150], M.E. Vasile [28b],
L. Vaslin[85], G.A. Vasquez [168], A. Vasyukov [39], L.M. Vaughan [124], R. Vavricka[102],
T. Vazquez Schroeder [37], J. Veatch [32], V. Vecchio [103], M.J. Veen [105], I. Veliscek [30],
L.M. Veloce [158], F. Veloso [133a,133c], S. Veneziano [76a], A. Ventura [71a,71b], S. Ventura Gonzalez [138],
A. Verbytskyi [112], M. Verducci [75a,75b], C. Vergis [96], M. Verissimo De Araujo [84b],
W. Verkerke [117], J.C. Vermeulen [117], C. Vernieri [146], M. Vessella [105], M.C. Vetterli [145,ad],
A. Vgenopoulos [102], N. Viaux Maira [140f], T. Vickey [142], O.E. Vickey Boeriu [142],
G.H.A. Viehhauser [129], L. Vigani [64b], M. Villa [24b,24a], M. Villaplana Perez [166], E.M. Villhauer[53],
E. Vilucchi [54], M.G. Vincter [35], A. Visibile[117], C. Vittori [37], I. Vivarelli [24b,24a], E. Voevodina [112],
F. Vogel [111], J.C. Voigt [51], P. Vokac [135], Yu. Volkotrub [87b], J. Von Ahnen [49], E. Von Toerne [25],
B. Vormwald [37], V. Vorobel [136], K. Vorobev [38], M. Vos [166], K. Voss [144], M. Vozak [117],
L. Vozdecky [123], N. Vranjes [16], M. Vranjes Milosavljevic [16], M. Vreeswijk [117], N.K. Vu [63d,63c],
R. Vuillermet [37], O. Vujinovic [102], I. Vukotic [40], S. Wada [160], C. Wagner[105], J.M. Wagner [18a],
W. Wagner [174], S. Wahdan [174], H. Wahlberg [92], M. Wakida [113], J. Walder [137], R. Walker [111],
W. Walkowiak [144], A. Wall [131], E.J. Wallin [100], T. Wamorkar [6], A.Z. Wang [139], C. Wang [102],
C. Wang [11], H. Wang [18a], J. Wang [65c], P. Wang [98], R. Wang [62], R. Wang [6], S.M. Wang [151],
S. Wang [63b], S. Wang [14], T. Wang [63a], W.T. Wang [81], W. Wang [14], X. Wang [114a], X. Wang [165],
X. Wang [63c], Y. Wang [63d], Y. Wang [114a], Y. Wang[63a], Z. Wang [108], Z. Wang [63d,52,63c],
Z. Wang [108], A. Warburton [106], R.J. Ward [21], N. Warrack [60], S. Waterhouse [97], A.T. Watson [21],
H. Watson [60], M.F. Watson [21], E. Watton [60,137], G. Watts [141], B.M. Waugh [98], J.M. Webb [55],
C. Weber [30], H.A. Weber [19], M.S. Weber [20], S.M. Weber [64a], C. Wei [63a], Y. Wei [55],
A.R. Weidberg [129], E.J. Weik [120], J. Weingarten [50], C. Weiser [55], C.J. Wells [49], T. Wenaus [30],
B. Wendland [50], T. Wengler [37], N.S. Wenke[112], N. Wermes [25], M. Wessels [64a], A.M. Wharton [93],
A.S. White [62], A. White [8], M.J. White [1], D. Whiteson [162], L. Wickremasinghe [127],
W. Wiedenmann [173], M. Wielers [137], C. Wiglesworth [43], D.J. Wilbern[123], H.G. Wilkens [37],
J.J.H. Wilkinson [33], D.M. Williams [42], H.H. Williams[131], S. Williams [33], S. Willocq [105],

B.J. Wilson [103], P.J. Windischhofer [40], F.I. Winkel [31], F. Winklmeier [126], B.T. Winter [55], J.K. Winter [103], M. Wittgen [146], M. Wobisch [99], T. Wojtkowski [61], Z. Wolffs [117], J. Wollrath [162], M.W. Wolter [88], H. Wolters [133a,133c], M.C. Wong [139], E.L. Woodward [42], S.D. Worm [49], B.K. Wosiek [88], K.W. Woźniak [88], S. Wozniewski [56], K. Wraight [60], C. Wu [21], M. Wu [114b], M. Wu [116], S.L. Wu [173], X. Wu [57], Y. Wu [63a], Z. Wu [4], J. Wuerzinger [112,ab], T.R. Wyatt [103], B.M. Wynne [53], S. Xella [43], L. Xia [114a], M. Xia [15], M. Xie [63a], S. Xin [14,114c], A. Xiong [126], J. Xiong [18a], D. Xu [14], H. Xu [63a], L. Xu [63a], R. Xu [131], T. Xu [108], Y. Xu [15], Z. Xu [53], Z. Xu [114a], B. Yabsley [150], S. Yacoob [34a], Y. Yamaguchi [157], E. Yamashita [156], H. Yamauchi [160], T. Yamazaki [18a], Y. Yamazaki [86], J. Yan [63c], S. Yan [60], Z. Yan [105], H.J. Yang [63c,63d], H.T. Yang [63a], S. Yang [63a], T. Yang [65c], X. Yang [37], X. Yang [14], Y. Yang [45], Y. Yang [63a], Z. Yang [63a], W-M. Yao [18a], H. Ye [114a], H. Ye [56], J. Ye [14], S. Ye [30], X. Ye [63a], Y. Yeh [98], I. Yeletskikh [39], B.K. Yeo [18b], M.R. Yexley [98], T.P. Yildirim [129], P. Yin [42], K. Yorita [171], S. Younas [28b], C.J.S. Young [37], C. Young [146], C. Yu [14,114c], Y. Yu [63a], J. Yuan [14,114c], M. Yuan [108], R. Yuan [63d,63c], L. Yue [98], M. Zaazoua [63a], B. Zabinski [88], E. Zaid [53], Z.K. Zak [88], T. Zakareishvili [166], S. Zambito [57], J.A. Zamora Saa [140d,140b], J. Zang [156], D. Zanzi [55], O. Zaplatilek [135], C. Zeitnitz [174], H. Zeng [14], J.C. Zeng [165], D.T. Zenger Jr [27], O. Zenin [38], T. Ženiš [29a], S. Zenz [96], S. Zerradi [36a], D. Zerwas [67], M. Zhai [14,114c], D.F. Zhang [142], J. Zhang [63b], J. Zhang [6], K. Zhang [14,114c], L. Zhang [63a], L. Zhang [114a], P. Zhang [14,114c], R. Zhang [173], S. Zhang [108], S. Zhang [91], T. Zhang [156], X. Zhang [63c], X. Zhang [63b], Y. Zhang [63c], Y. Zhang [98], Y. Zhang [114a], Z. Zhang [18a], Z. Zhang [63b], Z. Zhang [67], H. Zhao [141], T. Zhao [63b], Y. Zhao [139], Z. Zhao [63a], Z. Zhao [63a], A. Zhemchugov [39], J. Zheng [114a], K. Zheng [165], X. Zheng [63a], Z. Zheng [146], D. Zhong [165], B. Zhou [108], H. Zhou [7], N. Zhou [63c], Y. Zhou [15], Y. Zhou [114a], Y. Zhou [7], C.G. Zhu [63b], J. Zhu [108], X. Zhu [63d], Y. Zhu [63c], Y. Zhu [63a], X. Zhuang [14], K. Zhukov [38], N.I. Zimine [39], J. Zinsser [64b], M. Ziolkowski [144], L. Živković [16], A. Zoccoli [24b,24a], K. Zoch [62], T.G. Zorbas [142], O. Zormpa [47], W. Zou [42], L. Zwalinski [37].

[1] Department of Physics, University of Adelaide, Adelaide; Australia.

[2] Department of Physics, University of Alberta, Edmonton AB; Canada.

[3] (a) Department of Physics, Ankara University, Ankara; (b) Division of Physics, TOBB University of Economics and Technology, Ankara; Türkiye.

[4] LAPP, Université Savoie Mont Blanc, CNRS/IN2P3, Annecy; France.

[5] APC, Université Paris Cité, CNRS/IN2P3, Paris; France.

[6] High Energy Physics Division, Argonne National Laboratory, Argonne IL; United States of America.

[7] Department of Physics, University of Arizona, Tucson AZ; United States of America.

[8] Department of Physics, University of Texas at Arlington, Arlington TX; United States of America.

[9] Physics Department, National and Kapodistrian University of Athens, Athens; Greece.

[10] Physics Department, National Technical University of Athens, Zografou; Greece.

[11] Department of Physics, University of Texas at Austin, Austin TX; United States of America.

[12] Institute of Physics, Azerbaijan Academy of Sciences, Baku; Azerbaijan.

[13] Institut de Física d'Altes Energies (IFAE), Barcelona Institute of Science and Technology, Barcelona; Spain.

[14] Institute of High Energy Physics, Chinese Academy of Sciences, Beijing; China.

[15] Physics Department, Tsinghua University, Beijing; China.

[16] Institute of Physics, University of Belgrade, Belgrade; Serbia.

[17] Department for Physics and Technology, University of Bergen, Bergen; Norway.

[18] (a) Physics Division, Lawrence Berkeley National Laboratory, Berkeley CA; (b) University of California,

Berkeley CA; United States of America.

[19]Institut für Physik, Humboldt Universität zu Berlin, Berlin; Germany.

[20]Albert Einstein Center for Fundamental Physics and Laboratory for High Energy Physics, University of Bern, Bern; Switzerland.

[21]School of Physics and Astronomy, University of Birmingham, Birmingham; United Kingdom.

[22][a]Department of Physics, Bogazici University, Istanbul;[b]Department of Physics Engineering, Gaziantep University, Gaziantep;[c]Department of Physics, Istanbul University, Istanbul; Türkiye.

[23][a]Facultad de Ciencias y Centro de Investigaciónes, Universidad Antonio Nariño, Bogotá;[b]Departamento de Física, Universidad Nacional de Colombia, Bogotá; Colombia.

[24][a]Dipartimento di Fisica e Astronomia A. Righi, Università di Bologna, Bologna;[b]INFN Sezione di Bologna; Italy.

[25]Physikalisches Institut, Universität Bonn, Bonn; Germany.

[26]Department of Physics, Boston University, Boston MA; United States of America.

[27]Department of Physics, Brandeis University, Waltham MA; United States of America.

[28][a]Transilvania University of Brasov, Brasov;[b]Horia Hulubei National Institute of Physics and Nuclear Engineering, Bucharest;[c]Department of Physics, Alexandru Ioan Cuza University of Iasi, Iasi;[d]National Institute for Research and Development of Isotopic and Molecular Technologies, Physics Department, Cluj-Napoca;[e]National University of Science and Technology Politechnica, Bucharest;[f]West University in Timisoara, Timisoara;[g]Faculty of Physics, University of Bucharest, Bucharest; Romania.

[29][a]Faculty of Mathematics, Physics and Informatics, Comenius University, Bratislava;[b]Department of Subnuclear Physics, Institute of Experimental Physics of the Slovak Academy of Sciences, Kosice; Slovak Republic.

[30]Physics Department, Brookhaven National Laboratory, Upton NY; United States of America.

[31]Universidad de Buenos Aires, Facultad de Ciencias Exactas y Naturales, Departamento de Física, y CONICET, Instituto de Física de Buenos Aires (IFIBA), Buenos Aires; Argentina.

[32]California State University, CA; United States of America.

[33]Cavendish Laboratory, University of Cambridge, Cambridge; United Kingdom.

[34][a]Department of Physics, University of Cape Town, Cape Town;[b]iThemba Labs, Western Cape;[c]Department of Mechanical Engineering Science, University of Johannesburg, Johannesburg;[d]National Institute of Physics, University of the Philippines Diliman (Philippines);[e]University of South Africa, Department of Physics, Pretoria;[f]University of Zululand, KwaDlangezwa;[g]School of Physics, University of the Witwatersrand, Johannesburg; South Africa.

[35]Department of Physics, Carleton University, Ottawa ON; Canada.

[36][a]Faculté des Sciences Ain Chock, Réseau Universitaire de Physique des Hautes Energies - Université Hassan II, Casablanca;[b]Faculté des Sciences, Université Ibn-Tofail, Kénitra;[c]Faculté des Sciences Semlalia, Université Cadi Ayyad, LPHEA-Marrakech;[d]LPMR, Faculté des Sciences, Université Mohamed Premier, Oujda;[e]Faculté des sciences, Université Mohammed V, Rabat;[f]Institute of Applied Physics, Mohammed VI Polytechnic University, Ben Guerir; Morocco.

[37]CERN, Geneva; Switzerland.

[38]Affiliated with an institute covered by a cooperation agreement with CERN.

[39]Affiliated with an international laboratory covered by a cooperation agreement with CERN.

[40]Enrico Fermi Institute, University of Chicago, Chicago IL; United States of America.

[41]LPC, Université Clermont Auvergne, CNRS/IN2P3, Clermont-Ferrand; France.

[42]Nevis Laboratory, Columbia University, Irvington NY; United States of America.

[43]Niels Bohr Institute, University of Copenhagen, Copenhagen; Denmark.

[44][a]Dipartimento di Fisica, Università della Calabria, Rende;[b]INFN Gruppo Collegato di Cosenza, Laboratori Nazionali di Frascati; Italy.

[45]Physics Department, Southern Methodist University, Dallas TX; United States of America.

[46]Physics Department, University of Texas at Dallas, Richardson TX; United States of America.

[47]National Centre for Scientific Research "Demokritos", Agia Paraskevi; Greece.

[48][a]Department of Physics, Stockholm University;[b]Oskar Klein Centre, Stockholm; Sweden.

[49]Deutsches Elektronen-Synchrotron DESY, Hamburg and Zeuthen; Germany.

[50]Fakultät Physik , Technische Universität Dortmund, Dortmund; Germany.

[51]Institut für Kern- und Teilchenphysik, Technische Universität Dresden, Dresden; Germany.

[52]Department of Physics, Duke University, Durham NC; United States of America.

[53]SUPA - School of Physics and Astronomy, University of Edinburgh, Edinburgh; United Kingdom.

[54]INFN e Laboratori Nazionali di Frascati, Frascati; Italy.

[55]Physikalisches Institut, Albert-Ludwigs-Universität Freiburg, Freiburg; Germany.

[56]II. Physikalisches Institut, Georg-August-Universität Göttingen, Göttingen; Germany.

[57]Département de Physique Nucléaire et Corpusculaire, Université de Genève, Genève; Switzerland.

[58][a]Dipartimento di Fisica, Università di Genova, Genova;[b]INFN Sezione di Genova; Italy.

[59]II. Physikalisches Institut, Justus-Liebig-Universität Giessen, Giessen; Germany.

[60]SUPA - School of Physics and Astronomy, University of Glasgow, Glasgow; United Kingdom.

[61]LPSC, Université Grenoble Alpes, CNRS/IN2P3, Grenoble INP, Grenoble; France.

[62]Laboratory for Particle Physics and Cosmology, Harvard University, Cambridge MA; United States of America.

[63][a]Department of Modern Physics and State Key Laboratory of Particle Detection and Electronics, University of Science and Technology of China, Hefei;[b]Institute of Frontier and Interdisciplinary Science and Key Laboratory of Particle Physics and Particle Irradiation (MOE), Shandong University, Qingdao;[c]School of Physics and Astronomy, Shanghai Jiao Tong University, Key Laboratory for Particle Astrophysics and Cosmology (MOE), SKLPPC, Shanghai;[d]Tsung-Dao Lee Institute, Shanghai;[e]School of Physics and Microelectronics, Zhengzhou University; China.

[64][a]Kirchhoff-Institut für Physik, Ruprecht-Karls-Universität Heidelberg, Heidelberg;[b]Physikalisches Institut, Ruprecht-Karls-Universität Heidelberg, Heidelberg; Germany.

[65][a]Department of Physics, Chinese University of Hong Kong, Shatin, N.T., Hong Kong;[b]Department of Physics, University of Hong Kong, Hong Kong;[c]Department of Physics and Institute for Advanced Study, Hong Kong University of Science and Technology, Clear Water Bay, Kowloon, Hong Kong; China.

[66]Department of Physics, National Tsing Hua University, Hsinchu; Taiwan.

[67]IJCLab, Université Paris-Saclay, CNRS/IN2P3, 91405, Orsay; France.

[68]Centro Nacional de Microelectrónica (IMB-CNM-CSIC), Barcelona; Spain.

[69]Department of Physics, Indiana University, Bloomington IN; United States of America.

[70][a]INFN Gruppo Collegato di Udine, Sezione di Trieste, Udine;[b]ICTP, Trieste;[c]Dipartimento Politecnico di Ingegneria e Architettura, Università di Udine, Udine; Italy.

[71][a]INFN Sezione di Lecce;[b]Dipartimento di Matematica e Fisica, Università del Salento, Lecce; Italy.

[72][a]INFN Sezione di Milano;[b]Dipartimento di Fisica, Università di Milano, Milano; Italy.

[73][a]INFN Sezione di Napoli;[b]Dipartimento di Fisica, Università di Napoli, Napoli; Italy.

[74][a]INFN Sezione di Pavia;[b]Dipartimento di Fisica, Università di Pavia, Pavia; Italy.

[75][a]INFN Sezione di Pisa;[b]Dipartimento di Fisica E. Fermi, Università di Pisa, Pisa; Italy.

[76][a]INFN Sezione di Roma;[b]Dipartimento di Fisica, Sapienza Università di Roma, Roma; Italy.

[77][a]INFN Sezione di Roma Tor Vergata;[b]Dipartimento di Fisica, Università di Roma Tor Vergata, Roma; Italy.

[78][a]INFN Sezione di Roma Tre;[b]Dipartimento di Matematica e Fisica, Università Roma Tre, Roma; Italy.

[79][a]INFN-TIFPA;[b]Università degli Studi di Trento, Trento; Italy.

[80]Universität Innsbruck, Department of Astro and Particle Physics, Innsbruck; Austria.

[81]University of Iowa, Iowa City IA; United States of America.

[82]Department of Physics and Astronomy, Iowa State University, Ames IA; United States of America.

[83]Istinye University, Sariyer, Istanbul; Türkiye.

[84][a]Departamento de Engenharia Elétrica, Universidade Federal de Juiz de Fora (UFJF), Juiz de Fora;[b]Universidade Federal do Rio De Janeiro COPPE/EE/IF, Rio de Janeiro;[c]Instituto de Física, Universidade de São Paulo, São Paulo;[d]Rio de Janeiro State University, Rio de Janeiro;[e]Federal University of Bahia, Bahia; Brazil.

[85]KEK, High Energy Accelerator Research Organization, Tsukuba; Japan.

[86]Graduate School of Science, Kobe University, Kobe; Japan.

[87][a]AGH University of Krakow, Faculty of Physics and Applied Computer Science, Krakow;[b]Marian Smoluchowski Institute of Physics, Jagiellonian University, Krakow; Poland.

[88]Institute of Nuclear Physics Polish Academy of Sciences, Krakow; Poland.

[89]Faculty of Science, Kyoto University, Kyoto; Japan.

[90]Research Center for Advanced Particle Physics and Department of Physics, Kyushu University, Fukuoka ; Japan.

[91]L2IT, Université de Toulouse, CNRS/IN2P3, UPS, Toulouse; France.

[92]Instituto de Física La Plata, Universidad Nacional de La Plata and CONICET, La Plata; Argentina.

[93]Physics Department, Lancaster University, Lancaster; United Kingdom.

[94]Oliver Lodge Laboratory, University of Liverpool, Liverpool; United Kingdom.

[95]Department of Experimental Particle Physics, Jožef Stefan Institute and Department of Physics, University of Ljubljana, Ljubljana; Slovenia.

[96]School of Physics and Astronomy, Queen Mary University of London, London; United Kingdom.

[97]Department of Physics, Royal Holloway University of London, Egham; United Kingdom.

[98]Department of Physics and Astronomy, University College London, London; United Kingdom.

[99]Louisiana Tech University, Ruston LA; United States of America.

[100]Fysiska institutionen, Lunds universitet, Lund; Sweden.

[101]Departamento de Física Teorica C-15 and CIAFF, Universidad Autónoma de Madrid, Madrid; Spain.

[102]Institut für Physik, Universität Mainz, Mainz; Germany.

[103]School of Physics and Astronomy, University of Manchester, Manchester; United Kingdom.

[104]CPPM, Aix-Marseille Université, CNRS/IN2P3, Marseille; France.

[105]Department of Physics, University of Massachusetts, Amherst MA; United States of America.

[106]Department of Physics, McGill University, Montreal QC; Canada.

[107]School of Physics, University of Melbourne, Victoria; Australia.

[108]Department of Physics, University of Michigan, Ann Arbor MI; United States of America.

[109]Department of Physics and Astronomy, Michigan State University, East Lansing MI; United States of America.

[110]Group of Particle Physics, University of Montreal, Montreal QC; Canada.

[111]Fakultät für Physik, Ludwig-Maximilians-Universität München, München; Germany.

[112]Max-Planck-Institut für Physik (Werner-Heisenberg-Institut), München; Germany.

[113]Graduate School of Science and Kobayashi-Maskawa Institute, Nagoya University, Nagoya; Japan.

[114][a]Department of Physics, Nanjing University, Nanjing;[b]School of Science, Shenzhen Campus of Sun Yat-sen University;[c]University of Chinese Academy of Science (UCAS), Beijing; China.

[115]Department of Physics and Astronomy, University of New Mexico, Albuquerque NM; United States of America.

[116]Institute for Mathematics, Astrophysics and Particle Physics, Radboud University/Nikhef, Nijmegen; Netherlands.

[117]Nikhef National Institute for Subatomic Physics and University of Amsterdam, Amsterdam; Netherlands.

[118]Department of Physics, Northern Illinois University, DeKalb IL; United States of America.

[119][a]New York University Abu Dhabi, Abu Dhabi;[b]United Arab Emirates University, Al Ain; United Arab Emirates.

[120]Department of Physics, New York University, New York NY; United States of America.

[121]Ochanomizu University, Otsuka, Bunkyo-ku, Tokyo; Japan.

[122]Ohio State University, Columbus OH; United States of America.

[123]Homer L. Dodge Department of Physics and Astronomy, University of Oklahoma, Norman OK; United States of America.

[124]Department of Physics, Oklahoma State University, Stillwater OK; United States of America.

[125]Palacký University, Joint Laboratory of Optics, Olomouc; Czech Republic.

[126]Institute for Fundamental Science, University of Oregon, Eugene, OR; United States of America.

[127]Graduate School of Science, Osaka University, Osaka; Japan.

[128]Department of Physics, University of Oslo, Oslo; Norway.

[129]Department of Physics, Oxford University, Oxford; United Kingdom.

[130]LPNHE, Sorbonne Université, Université Paris Cité, CNRS/IN2P3, Paris; France.

[131]Department of Physics, University of Pennsylvania, Philadelphia PA; United States of America.

[132]Department of Physics and Astronomy, University of Pittsburgh, Pittsburgh PA; United States of America.

[133][a]Laboratório de Instrumentação e Física Experimental de Partículas - LIP, Lisboa;[b]Departamento de Física, Faculdade de Ciências, Universidade de Lisboa, Lisboa;[c]Departamento de Física, Universidade de Coimbra, Coimbra;[d]Centro de Física Nuclear da Universidade de Lisboa, Lisboa;[e]Departamento de Física, Universidade do Minho, Braga;[f]Departamento de Física Teórica y del Cosmos, Universidad de Granada, Granada (Spain);[g]Departamento de Física, Instituto Superior Técnico, Universidade de Lisboa, Lisboa; Portugal.

[134]Institute of Physics of the Czech Academy of Sciences, Prague; Czech Republic.

[135]Czech Technical University in Prague, Prague; Czech Republic.

[136]Charles University, Faculty of Mathematics and Physics, Prague; Czech Republic.

[137]Particle Physics Department, Rutherford Appleton Laboratory, Didcot; United Kingdom.

[138]IRFU, CEA, Université Paris-Saclay, Gif-sur-Yvette; France.

[139]Santa Cruz Institute for Particle Physics, University of California Santa Cruz, Santa Cruz CA; United States of America.

[140][a]Departamento de Física, Pontificia Universidad Católica de Chile, Santiago;[b]Millennium Institute for Subatomic physics at high energy frontier (SAPHIR), Santiago;[c]Instituto de Investigación Multidisciplinario en Ciencia y Tecnología, y Departamento de Física, Universidad de La Serena;[d]Universidad Andres Bello, Department of Physics, Santiago;[e]Instituto de Alta Investigación, Universidad de Tarapacá, Arica;[f]Departamento de Física, Universidad Técnica Federico Santa María, Valparaíso; Chile.

[141]Department of Physics, University of Washington, Seattle WA; United States of America.

[142]Department of Physics and Astronomy, University of Sheffield, Sheffield; United Kingdom.

[143]Department of Physics, Shinshu University, Nagano; Japan.

[144]Department Physik, Universität Siegen, Siegen; Germany.

[145]Department of Physics, Simon Fraser University, Burnaby BC; Canada.

[146]SLAC National Accelerator Laboratory, Stanford CA; United States of America.

[147]Department of Physics, Royal Institute of Technology, Stockholm; Sweden.

[148]Departments of Physics and Astronomy, Stony Brook University, Stony Brook NY; United States of

America.

[149]Department of Physics and Astronomy, University of Sussex, Brighton; United Kingdom.

[150]School of Physics, University of Sydney, Sydney; Australia.

[151]Institute of Physics, Academia Sinica, Taipei; Taiwan.

[152](a)E. Andronikashvili Institute of Physics, Iv. Javakhishvili Tbilisi State University, Tbilisi;(b)High Energy Physics Institute, Tbilisi State University, Tbilisi;(c)University of Georgia, Tbilisi; Georgia.

[153]Department of Physics, Technion, Israel Institute of Technology, Haifa; Israel.

[154]Raymond and Beverly Sackler School of Physics and Astronomy, Tel Aviv University, Tel Aviv; Israel.

[155]Department of Physics, Aristotle University of Thessaloniki, Thessaloniki; Greece.

[156]International Center for Elementary Particle Physics and Department of Physics, University of Tokyo, Tokyo; Japan.

[157]Department of Physics, Tokyo Institute of Technology, Tokyo; Japan.

[158]Department of Physics, University of Toronto, Toronto ON; Canada.

[159](a)TRIUMF, Vancouver BC;(b)Department of Physics and Astronomy, York University, Toronto ON; Canada.

[160]Division of Physics and Tomonaga Center for the History of the Universe, Faculty of Pure and Applied Sciences, University of Tsukuba, Tsukuba; Japan.

[161]Department of Physics and Astronomy, Tufts University, Medford MA; United States of America.

[162]Department of Physics and Astronomy, University of California Irvine, Irvine CA; United States of America.

[163]University of Sharjah, Sharjah; United Arab Emirates.

[164]Department of Physics and Astronomy, University of Uppsala, Uppsala; Sweden.

[165]Department of Physics, University of Illinois, Urbana IL; United States of America.

[166]Instituto de Física Corpuscular (IFIC), Centro Mixto Universidad de Valencia - CSIC, Valencia; Spain.

[167]Department of Physics, University of British Columbia, Vancouver BC; Canada.

[168]Department of Physics and Astronomy, University of Victoria, Victoria BC; Canada.

[169]Fakultät für Physik und Astronomie, Julius-Maximilians-Universität Würzburg, Würzburg; Germany.

[170]Department of Physics, University of Warwick, Coventry; United Kingdom.

[171]Waseda University, Tokyo; Japan.

[172]Department of Particle Physics and Astrophysics, Weizmann Institute of Science, Rehovot; Israel.

[173]Department of Physics, University of Wisconsin, Madison WI; United States of America.

[174]Fakultät für Mathematik und Naturwissenschaften, Fachgruppe Physik, Bergische Universität Wuppertal, Wuppertal; Germany.

[175]Department of Physics, Yale University, New Haven CT; United States of America.

[a] Also Affiliated with an institute covered by a cooperation agreement with CERN.

[b] Also at An-Najah National University, Nablus; Palestine.

[c] Also at Borough of Manhattan Community College, City University of New York, New York NY; United States of America.

[d] Also at Center for Interdisciplinary Research and Innovation (CIRI-AUTH), Thessaloniki; Greece.

[e] Also at Centro Studi e Ricerche Enrico Fermi; Italy.

[f] Also at CERN, Geneva; Switzerland.

[g] Also at CMD-AC UNEC Research Center, Azerbaijan State University of Economics (UNEC); Azerbaijan.

[h] Also at Département de Physique Nucléaire et Corpusculaire, Université de Genève, Genève; Switzerland.

[i] Also at Departament de Fisica de la Universitat Autonoma de Barcelona, Barcelona; Spain.

[j] Also at Department of Financial and Management Engineering, University of the Aegean, Chios; Greece.

[k] Also at Department of Physics, California State University, Sacramento; United States of America.

[l] Also at Department of Physics, King's College London, London; United Kingdom.

[m] Also at Department of Physics, Stanford University, Stanford CA; United States of America.

[n] Also at Department of Physics, Stellenbosch University; South Africa.

[o] Also at Department of Physics, University of Fribourg, Fribourg; Switzerland.

[p] Also at Department of Physics, University of Thessaly; Greece.

[q] Also at Department of Physics, Westmont College, Santa Barbara; United States of America.

[r] Also at Hellenic Open University, Patras; Greece.

[s] Also at Institucio Catalana de Recerca i Estudis Avancats, ICREA, Barcelona; Spain.

[t] Also at Institut für Experimentalphysik, Universität Hamburg, Hamburg; Germany.

[u] Also at Institute for Nuclear Research and Nuclear Energy (INRNE) of the Bulgarian Academy of Sciences, Sofia; Bulgaria.

[v] Also at Institute of Applied Physics, Mohammed VI Polytechnic University, Ben Guerir; Morocco.

[w] Also at Institute of Particle Physics (IPP); Canada.

[x] Also at Institute of Physics and Technology, Mongolian Academy of Sciences, Ulaanbaatar; Mongolia.

[y] Also at Institute of Physics, Azerbaijan Academy of Sciences, Baku; Azerbaijan.

[z] Also at Institute of Theoretical Physics, Ilia State University, Tbilisi; Georgia.

[aa] Also at National Institute of Physics, University of the Philippines Diliman (Philippines); Philippines.

[ab] Also at Technical University of Munich, Munich; Germany.

[ac] Also at The Collaborative Innovation Center of Quantum Matter (CICQM), Beijing; China.

[ad] Also at TRIUMF, Vancouver BC; Canada.

[ae] Also at Università di Napoli Parthenope, Napoli; Italy.

[af] Also at University of Colorado Boulder, Department of Physics, Colorado; United States of America.

[ag] Also at Washington College, Chestertown, MD; United States of America.

[ah] Also at Yeditepe University, Physics Department, Istanbul; Türkiye.

[*] Deceased